Mechanical Design and Analysis of a Magnetic Gearbox

by

Charles Johannes Agenbach

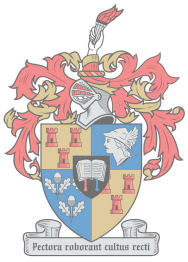

Thesis presented in partial fulfilment of the requirements for the degree of Master of Engineering (Mechanical) in the Faculty of Engineering at Stellenbosch University

Supervisor: Dr D.N.J. Els
Co-supervisor: Prof R-J. Wang

March 2018

Declaration

By submitting this thesis electronically, I declare that the entirety of the work contained therein is my own, original work, that I am the sole author thereof (save to the extent explicitly otherwise stated), that reproduction and publication thereof by Stellenbosch University will not infringe any third party rights and that I have not previously in its entirety or in part submitted it for obtaining any qualification.

Date: March 2018

UNIVERSITEIT·STELLENBOSCH·UNIVERSITY
jou kennisvennoot • your knowledge partner

Plagiaatverklaring / Plagiarism *Declaration*

1 Plagiaat is die oorneem en gebruik van die idees, materiaal en ander intellektuele eiendom van ander persone asof dit jou eie werk is.
Plagiarism is the use of ideas, material and other intellectual property of another's work and to present is as my own.

2 Ek erken dat die pleeg van plagiaat 'n strafbare oortreding is aangesien dit 'n vorm van diefstal is.
I agree that plagiarism is a punishable offence because it constitutes theft.

3 Ek verstaan ook dat direkte vertalings plagiaat is.
I also understand that direct translations are plagiarism.

4 Dienooreenkomstig is alle aanhalings en bydraes vanuit enige bron (ingesluit die internet) volledig verwys (erken). Ek erken dat die woordelikse aanhaal van teks sonder aanhalingstekens (selfs al word die bron volledig erken) plagiaat is.
Accordingly all quotations and contributions from any source whatsoever (including the internet) have been cited fully. I understand that the reproduction of text without quotation marks (even when the source is cited) is plagiarism.

5 Ek verklaar dat die werk in hierdie skryfstuk vervat, behalwe waar anders aangedui, my eie oorspronklike werk is en dat ek dit nie vantevore in die geheel of gedeeltelik ingehandig het vir bepunting in hierdie module/werkstuk of 'n ander module/werkstuk nie.
I declare that the work contained in this assignment, except where otherwise stated, is my original work and that I have not previously (in its entirety or in part) submitted it for grading in this module/assignment or another module/assignment.

Studentenommer / *Student number*	**Handtekening / *Signature***
Voorletters en van / *Initials and surname*	**Datum / *Date***

Abstract

Mechanical Design and Analysis of a Magnetic Gearbox

C.J. Agenbach

Department of Mechanical and Mechatronic Engineering,
University of Stellenbosch,
Private Bag X1, Matieland 7602, South Africa.

Thesis: MEng (Mech)

March 2018

Unbalanced magnetic forces (UMFs) in magnetic gears (MG) were investigated and a criterion for identifying gear ratios with a minimum UMF was derived. The proposed criterion was assessed by developing a prototype MG in conjunction with the criterion. More specifically, a vibrational analysis was done on the MG and showed a significant decrease in UMFs and vibrations. An evaluation of the final MG showed a no-load loss of 180 W relative to 2.8 kW rated power. Furthermore, the no-load losses for the MG were reduced by 36.8 %, compared to a previous MG prototype. An efficiency of 95 % was achieved and a large spectrum of high efficiency operating conditions was obtained. The measured vs. simulated torque ripple had a difference of 9.5 % and a percentage torque ripple of 14.4 % was measured, thus indicating an MG with stable power transmission and low UMF was achieved in the presented research.

Uittreksel

Meganiese Ontwerp en Analise van 'n Magnetiese Ratkas

("Mechanical Design and Analysis of a Magnetic Gearbox")

C.J. Agenbach

Departement van Meganiese en Megatroniese Ingenieurswese,
Universiteit van Stellenbosch,
Privaatsak X1, Matieland 7602, Suid Afrika.

Tesis: MIng (Meg)

Maart 2018

Ongebalanseerde magnetiese kragte (OMKs) in magnetiese ratte (MR) is ondersoek en ratverhoudings met beperkte OMK is afgelei met behulp van 'n kriterium. Die voorgestelde kriterium was beoordeel deur 'n prototipe MR te ontwikkel in samewerking met die kriterium. 'n Vibrasie-analiese is op die MR gedoen en dit het 'n beduidende afname in OMKs en vibrasies aangedui. 'n Evaluering van die finale MR het las-vrye verliese van 180 W gehad teenoor die 2.8 kW dryfkrag. Die las-vrye verliese van die MR het met 36.8 % verminder vanaf 'n vorige MR prototipe. 'n Effektiwiteit van 95 % is bereik en die doeltreffendheid spektrum het aansienlik toegeneem. Die gemete teenoor gesimuleerde wringkrag rimpeling het 'n verskil van 9.5 % aangedui en 'n persentasie wringkrag rimpeling van 14.4 % was gemeet, dus dui dit aan dat 'n MR met 'n stabiele kragoordrag en met beperkte OMK bereik is in die voorgestelde navorsing.

Acknowledgements

For helping me complete this thesis, I would like to express my sincere gratitude to:

- My Creator, Jesus Christ, for unconditional love, wisdom, and opportunities.
- My supervisor, Dr Danie Els, for his expertise, wise counsel, guidance, and all the fruitful discussions during our weekly meetings. Also, thank you for the financial support.
- My co-supervisor, Prof R.J. Wang, for all of his expertise, wise counsel, guidance, and encouragement to always strive towards the best possible solution. Also, thank you for introducing me to the magical world of magnets.
- The Mechanical en Mechatronic Engineering workshop for the use of their hardware and facilities. I specifically want to thank Mr Anton van den Berg for all his advice and extreme machining abilities.
- The Electrical and Electronic Engineering workshop for the use of their hardware and facilities. I specifically want to thank Mr André Swart for all his advice and guidance during the assembly of the magnets.
- Dr Stiaan Gerber for his expertise in SEMFEM and for always being willing to help.
- Alex Matthee for all his help and advice during the electrical design.
- Mrs Susan van der Spuy for all the order placements and for always being kind and helpful.
- My family and friends for all the support and unforgettable memories.

"En ons weet dat vir hulle wat God liefhet, alles ten goede meewerk, vir hulle wat na sy voorneme geroep is." Romeine 8:28

"And we know that all things work together for good to them that love God, to them who are the called according to his purpose." Romans 8:28

Dedications

This dissertation is dedicated to my parents, sister, and brother.
(Hierdie verhandeling word opgedra aan my ouers, suster en broer.)

Contents

List of Figures

List of Tables

Nomenclature

Abbreviations

2D	Two-Dimensional
3D	Three-Dimensional
ACC	Air Cooled Condenser
BSF	Ball Spin Frequency
CAD	Computer Aided Design
CCW	Counter Clockwise
CW	Clockwise
DFMA	Design for Manufacture and Assembly
DFT	Discrete Fourier Transform
E & E	Electrical and Electronic
FEA	Finite Element Analysis
FEM	Finite Element Method
FFT	Fundamental Train Frequency
FTF	Finite Element Analysis
FMMG	Flux Modulated Magnetic Gear
GMF	Gear-Mesh Frequency
HS	High-Speed
ICP	Integrating Circuit Piezoelectric
IRF	Inner Race Frequency
LCM	Least Common Multiple
LS	Low-Speed
MG	Magnetic Gear
M & M	Mechanical and Mechatronic
MMFD	Modified Method of Feasible Direction
NdFeB	Neodymium Iron Boron
OAT	One-at-a-Time

ORF	Outer Race Frequency
PEEK	Poly-Ether-Ether-Ketone
PSD	Power-Spectral-Density
PSO	Particle Swarm Optimisation
RNA	Reluctance network analysis
SEMFEM	Stellenbosch Electrical Machines Finite Element Method
UMF	Unbalanced Magnetic Force
VPF	Vane Passing Frequency
VSD	Variable Speed Drive

Constants

$g_0 = 9.81\,\mathrm{m/s^2}$

Roman Symbols

B	Magnetic flux density
B_r	Flux density distribution in the radial component
B_t	Flux density distribution circumferential component
Bd	Bearing ball diameter
b_{ri}	Radial Fourier coefficients of the flux density distribution
$b_{\theta i}$	Circumferential Fourier coefficients of the flux density distribution
F_e	Magnetic energy functional
$\mathcal{F}$	Magnetomotive force
f_c	Cogging factor
G_{r1}	Magnetic gear ratio for fixed low speed rotor
G_{r2}	Magnetic gear ratio for fixed modulator
H	Magnetic flux intensity
L	Stack length of the magnetic gear
M	Magnetomotive force magnitude
n_b	Number of balls
Pd	Pitch diameter
P_{in}	Power in
P_{out}	Power out
$\mathcal{P}$	Permeance
p	General number of magnetic pole pairs
p_{hs}	Number of magnetic pole pairs on the high-speed rotor
p_{ls}	Number of magnetic pole pairs on the low-speed rotor
q_m	Number of ferromagnetic pole pieces

r	Arc radius
r_g	Average air-gap radius
rps	Revolutions per second
S_{ez}	Endurance limit
S_{ut}	Ultimate tensile stress
t	Time
V	Volume
W	Stored magnetic energy

Greek Symbols

η	Magnetic gear efficiency
θ	Angular position of the componentrad
θ_0	Initial angular position of the componentrad
λ_{rj}	Radial Fourier coefficients of the modulating functions
$\lambda_{\theta j}$	Circumferential Fourier coefficients of the modulating functions
μ	Magnetic permeability
μ_0	Permeability in air-gap
ϕ	Magnetic flux
ϕ_c	Contact angle
σ'_{az}	Amplitude stress
σ'_{mz}	Median stress
τ	Torque
τ	2D
τ_{avg}	Average torque
τ_{max}	Maximum torque
τ_{min}	Minimum torque
τ_{rated}	Rated torque
τ_{ripple}	Ripple torque
$\tau_{ripple,\%}$	Ripple torque percentage
Ω_{hs}	Rotational speed of the high-speed rotor
Ω_{ls}	Rotational speed of the low-speed rotor
Ω_m	Rotational speed of the modulator
Ω_r	Rotational speed of whichever rotor is analysed

Vectors and Tensors

$\vec{\boldsymbol{A}}$	Magnetic potential vector
$\vec{\boldsymbol{B}}$	Magnetic flux density vector

$\vec{\boldsymbol{F}}$	Total magnetic force vector
$\vec{\boldsymbol{f}}$	Force density
$\vec{\boldsymbol{H}}$	Magnetic flux intensity vector
$\vec{\boldsymbol{J}}$	Magnetic current densit vector
$\mathbb{T}$	Maxwell stress tensor

Chapter 1

Introduction

Efficient and clean power generation has been one of the main challenges of the modern power industry. For most power plants cooling the working fluid is a crucial factor in the process. Two common cooling systems are: wet-cooled systems and dry-cooled systems.

In wet-cooled systems, the working fluid is water and one major disadvantage of the system is its high water consumption, which has a negative impact on the environment (Kröger, 2004).

In dry-cooled systems the working fluid is air and the cooling is done by forced convection. An example of a dry-cooled system is a force draught air-cooled condenser (ACC) (see Figure 1.1a). Dry cooling systems such as the ACC, are used in areas where water is limited, as discussed by Zhao *et al.* (2011) and Shi *et al.* (2009). In South Africa, dry cooling systems are often used due to water shortages and legislation. Examples of ACC systems in South Africa are the Medupi and Matimba power plants (see Figure 1.1b).

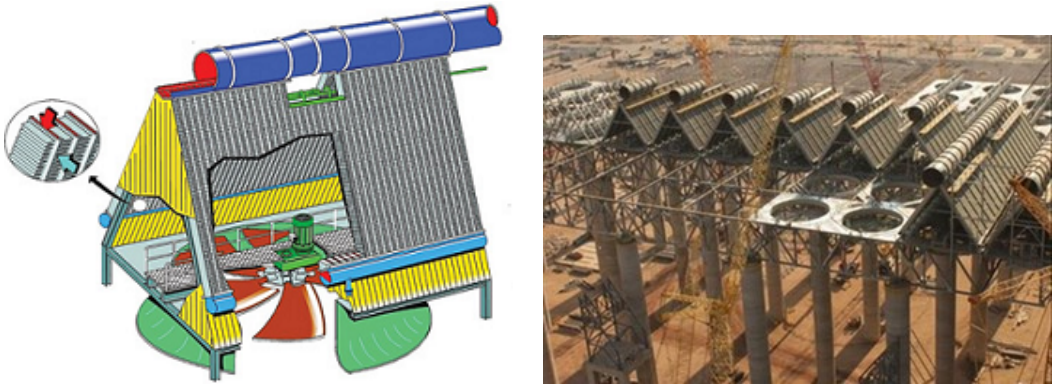

(a) (b)

Figure 1.1: Two views of ACC systems: (a) A-frame ACC system (Wurtz, 2008). (b) Air cooled condenser site at Medupi (ANA, 2016).

1.1 Problem Statement and Motivation

The standard fan drive configuration for these ACC units consists of an induction motor connected to a mechanical gearbox. These ACC units are driven by line-fed induction motors and, as a result, the entire system experiences large start-up torques (Shaltout, 1994).

According to Liu *et al.* (2009*a*) wind speed, direction and air temperature are the main factors which affect the operation of an ACC. Also, studies by Li *et al.* (2011) reveal that the mechanical fan drive system experiences high fatigue over time due to fan vibration and cross air flow conditions. Furthermore, these units operate for a long period before maintenance is done on them and due to load spikes, the lifespan of the gears are drastically reduced (Zhao and Liu, 2009).

A case study at Matimba power station has shown that the number of gearbox failures per year is over 30 out of 288 units (Goldschagg, 2013), and the number of failures per year is illustrated in Figure 1.2.

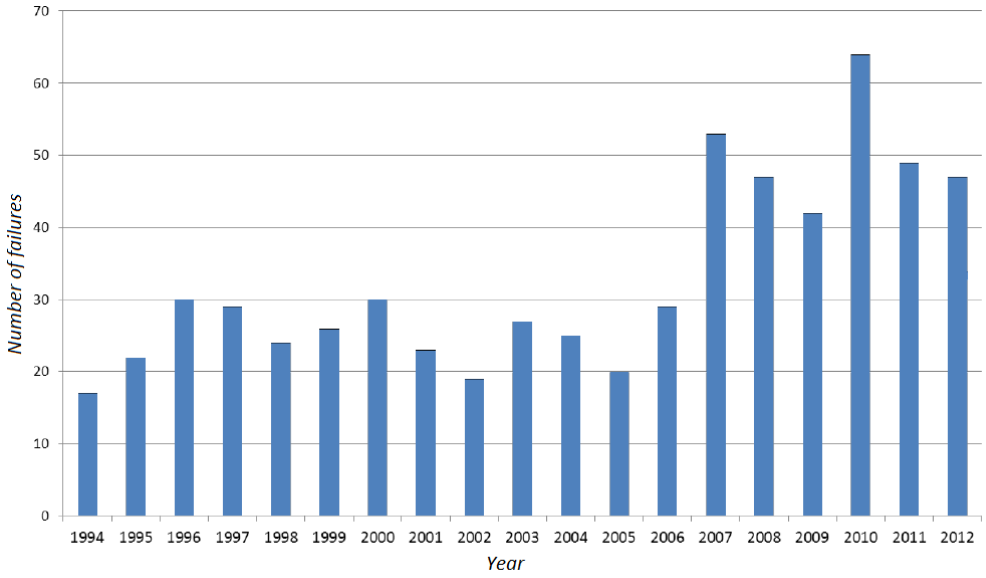

Figure 1.2: Annual number of gear failures out of 288 gearboxes (Goldschagg, 2013).

Recently, a new gear technology has come to the attention of engineers, namely the magnetic gear (MG). The reason for this sudden increase in interest can be attributed to the increased availability of high energy permanent magnetic material, and more importantly the novel magnetic gear topologies (Gerber and Wang, 2013).

One advantage MGs have is the ability to operate with little or no lubrication, thus an MG does not require regular oil replacement like mechanical gears do. Another advantage is their built-in overload protection which allows the

components of the gear to merely slip when overloaded. Also, since the power transfer is contactless, frictional loss due to meshing teeth can be neglected.

Gouda *et al.* (2011) and Desvaux *et al.* (2017) have compared mechanical gears with magnetic gears and found that magnetic gears can be used as an alternative gear. As a result, the MG will be investigated as an alternative gear possibility for ACC units.

1.2 Research Objectives

As a part of Stellenbosch University's axial fan system project funded by the European Union's Horizon 2020 research and innovation programme, a multidisciplinary team from both the Mechanical & Mechatronic (M & M) Engineering and the Electrical & Electronics (E & E) Engineering Departments was formed focusing on developing a sustainable MG for cooling fan applications.

A Master's student from the E & E Department designed and evaluated a first prototype MG (Matthee, 2016), with the assistance of a Master's student from the M & M Department, the author. This prototype will be used as a reference for the research presented in this thesis and, as a result, the first prototype MG will be further investigated.

The main objective of this research project is to develop a second prototype MG, with an improved mechanical design, and test its performance. More specifically, to perform a case study on the first prototype, investigate the magnetic force distribution of an MG, perform a vibrational analysis, and investigate the manufacturing and maintenance processes of MGs as they are currently and improve on them. Thus, determining whether this technology will be acceptable for cooling fan applications.

The research objectives are summarised as follows:

- Perform a case study on the first prototype.
- Investigate unbalanced magnetic forces.
- Perform a vibrational analysis.
- Develop manufacturing and maintenance techniques.
- Design and develop a second improved prototype.
- Evaluate the prototype.

1.3 Project Scope

A well-rounded MG design requires both the electromagnetic and the mechanical design to be sound. This project is limited to the mechanical design and analysis of an MG, as a result, the electromagnetic design and analysis of the gear will be done with the aid of the (E & E) Engineering Department.

1.4 Research Approach

In order to accomplish all the research objectives, the following research approach is followed. Firstly, a literature review is done in the MG research field to provide background on how its research has evolved and to identify an appropriate MG topology. Furthermore, the literature review provides insight into the operating principles of the MG. The literature review also provides the required knowledge for the vibration analysis presented in this thesis. Secondly, previous studies are used as a reference for the electromagnetic design aspects, and an electromagnetic analysis is performed with the guidance of the (E & E) Engineering Department. Possible mechanical improvements are investigated by performing a case study on the first prototype. In addition, design specifications are defined for the second prototype. Thirdly, the magnetic forces and how they affect the MG design are investigated. The electromagnetic design of the second prototype is done by applying torque density and torque ripple optimisations. The second prototype is then designed with mechanical improvements, which include lower unbalanced forces, motor-interface, and a prototype which is easily manufactured, assembled, and maintained. Lastly, an evaluation of the second prototype will be done by performing no load tests and fan load tests. Furthermore, a vibration analysis will be done to identify the excited force frequencies of the MG. The measured and simulated torque ripple will also be compared.

1.5 Thesis Layout

The structure layout of this thesis is as follows:

Chapter 2 (Literature Review):
In the literature review, the background and research for MGs are given. The mechanical research for this thesis is also presented here.

Chapter 3 (Design Considerations):
In the design considerations, both the electromagnetic and mechanical design aspects are investigated. For the mechanical design, a case study on the first prototype MG is given.

Chapter 4 (Force Analysis):
In the force analysis, the relationship between the magnetic forces and the components of an MG is analysed.

Chapter 5 (Prototype Design):
In the prototype design, a second prototype with improvements is designed.

Chapter 6 (Prototype Evaluation):
In the prototype evaluation, various tests are done on the second prototype and compared to simulation results.

Chapter 7 (Conclusion and Recommendations):
In the conclusion and recommendations, all findings are discussed and recommendations for future work are made.

Chapter 2

Literature Review

This chapter is a literature review on MGs. Background is given and how the research evolved is described. Figure 2.1 is a graphic representation of the research that will be covered in this chapter. This project map is composed of four boundary layers that correlate with the section layout of the chapter. The first layer gives some background on transmission systems in general (section 2.1). The second layer covers some of the existing MG topologies (section 2.2). The third layer refers to the specific research done on the flux modulated magnetic gear (FMMG) (section 2.3). The fourth boundary layer represents the mechanical literature read as research for this thesis (section 2.4).

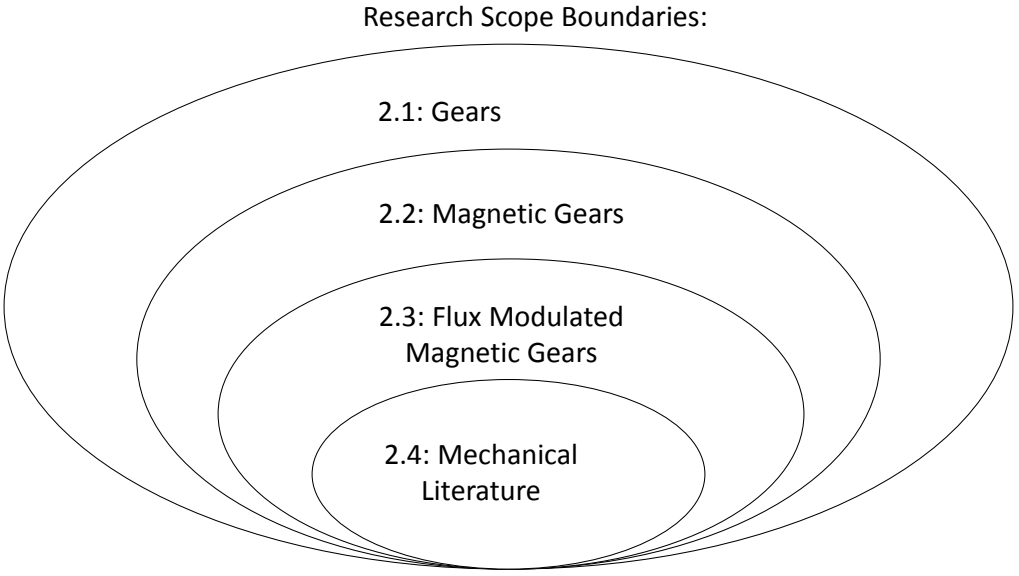

Figure 2.1: Map representing the field of research for this project (not to scale).

2.1 General Transmission Background

One of the first documented transmission mechanisms was invented by Da Vinci, (Figure 2.2). In earlier years systems like these were often used for hoisting heavy loads, i.e. building materials, ship anchors, etc. However, as the gear technology improved, they have become popular in various applications, especially for rotating machinery.

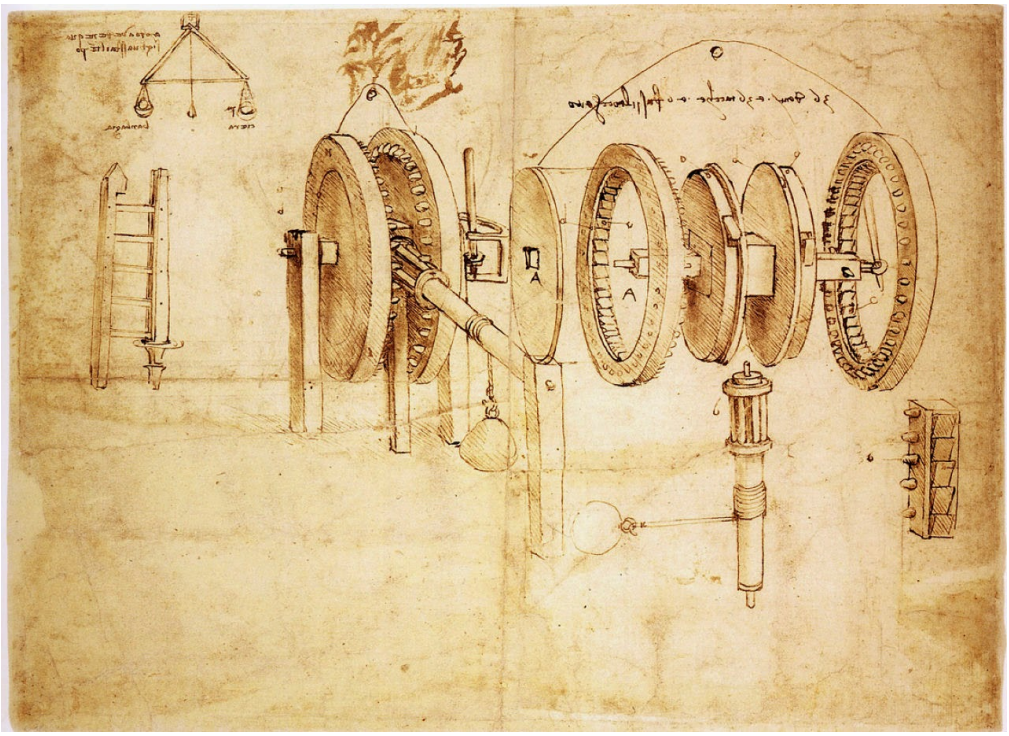

Figure 2.2: Da Vinci's gear invention (Scott, 2014).

2.2 Magnetic Gears

Magnetic gear research began as early as the 19th century when Charles G. Armstrong proposed a patent for a power-transmitting device by means of employing magnetic attractive and repulsive forces (Armstrong, 1901). Figure 2.3 is a visual representation of this patent.

In recent years research regarding magnetic gears has gained great popularity in both research institutions and industry. Figure 2.4 is a histogram of all the publications, journals, conferences, and patents for MG research (Tlali *et al.*, 2014). From this figure, an increase in research activity can be seen from the start of the 20th century. One of the reasons for this may be the increasing availability of high energy density magnetic materials, such as Neodymium Iron Boron (NdFeB). Another reason for the sudden increase is the novel topologies developed in recent years.

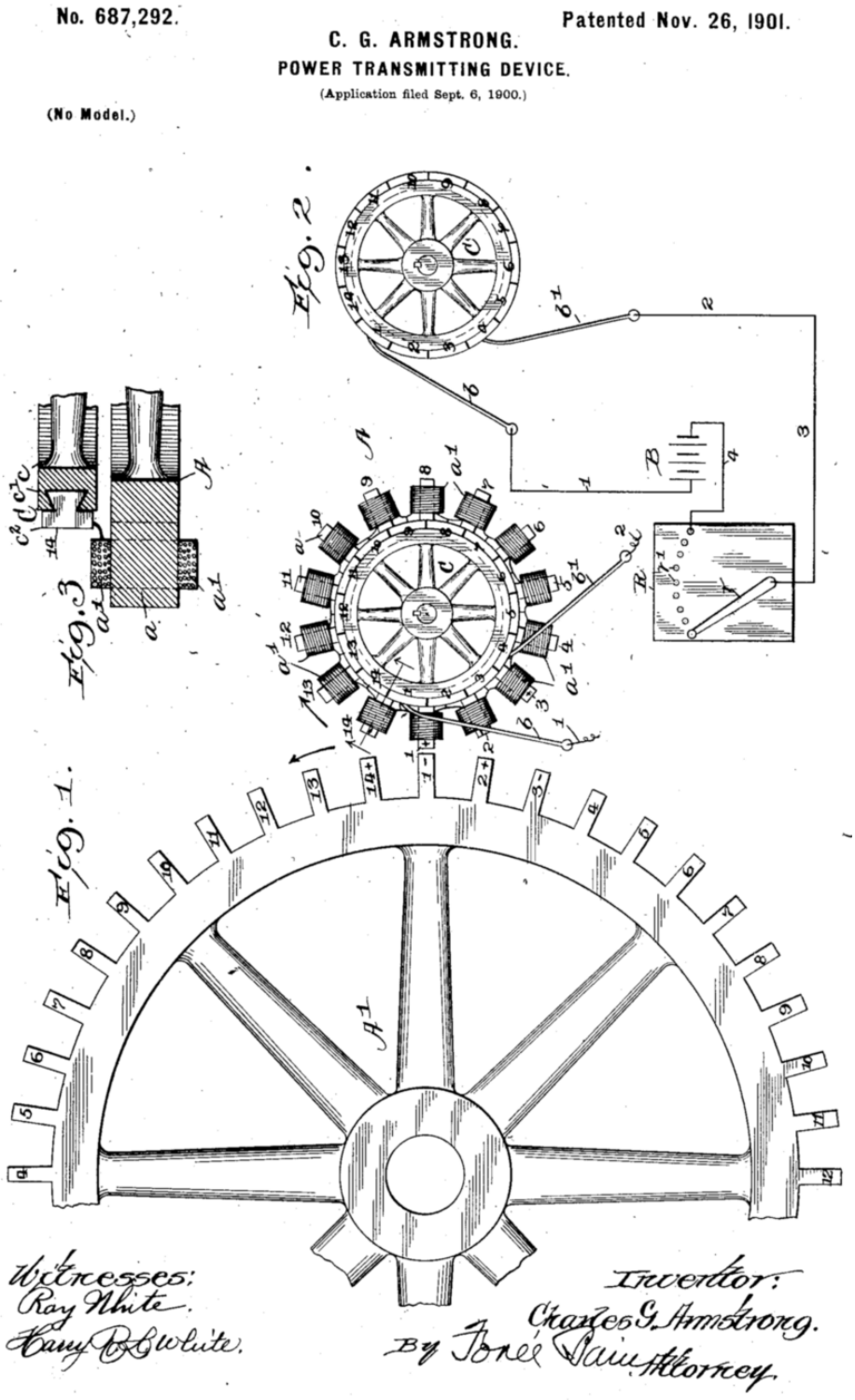

Figure 2.3: Power transmitting device created by Armstrong (1901).

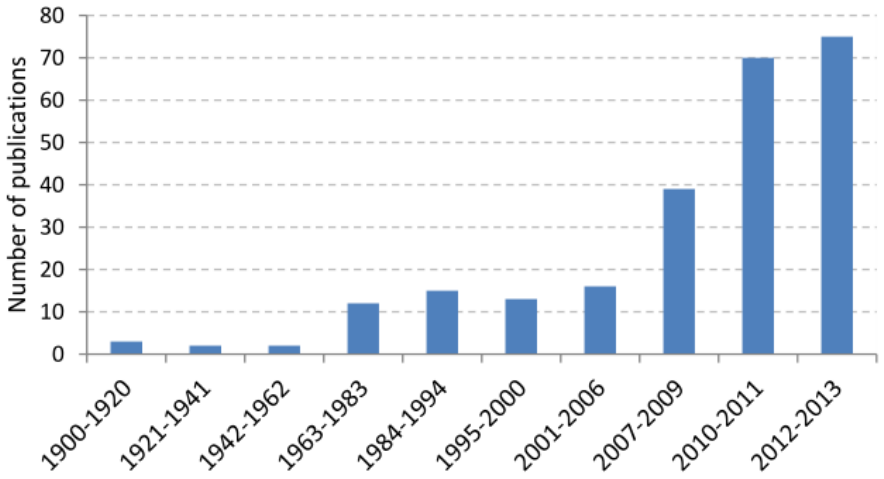

Figure 2.4: Published work on magnetic gears (1900-2013) (Tlali *et al.*, 2014).

Various magnetic gear topologies have been developed for their mechanical counterparts, as seen in Figure 2.5. The first magnetic gears focused more on traditional gear types, i.e. spur gears, (Armstrong, 1901) and worm gears (Baermann, 1974). However, only a small portion of the permanent magnets contribute to the torque being transmitted. Hence, they have a lower torque density and efficiency than their mechanical counterparts, as mentioned in Atallah *et al.* (2004).

The high torque capability of magnetic gears was discovered by Atallah and Howe (2001). After their research, the amount of research on magnetic gears started to escalate and three topologies that stand out due to their high torque density capabilities are given in Figure 2.6, namely: flux modulated magnetic gear (FMMG) (Atallah and Howe, 2001), harmonic magnetic gears (Rens *et al.*, 2010), and planetary magnetic gears (Huang *et al.*, 2008). The high torque density in these topologies can be attributed to the increased energy utilisation of the magnetic fields, and hence the torque transfer at any given time is continuous (Tlali *et al.*, 2014).

In recent years, the FMMG has been studied in detail and appears to be one of the most promising magnetic gear topologies due to its reliable performance and layout advantages. Some of these studies include those by Atallah and Howe (2001), Rasmussen *et al.* (2005), and Gerber and Wang (2013). Thus, it was decided that the FMMG topology would be the most suitable for this research and its application.

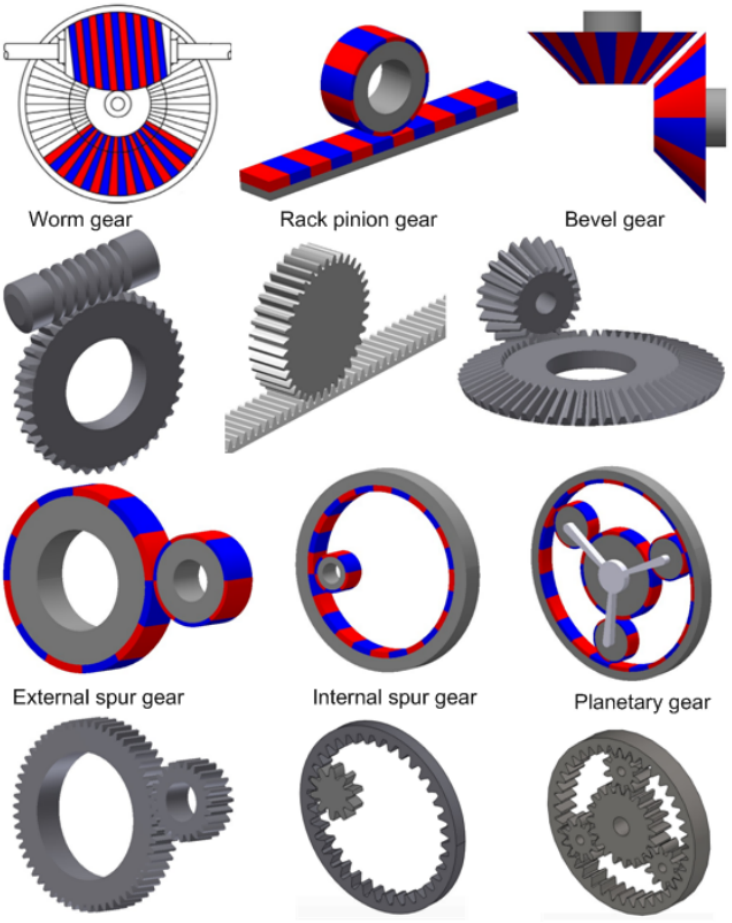

Figure 2.5: Mechanical and magnetic gear topologies (Tlali *et al.*, 2014).

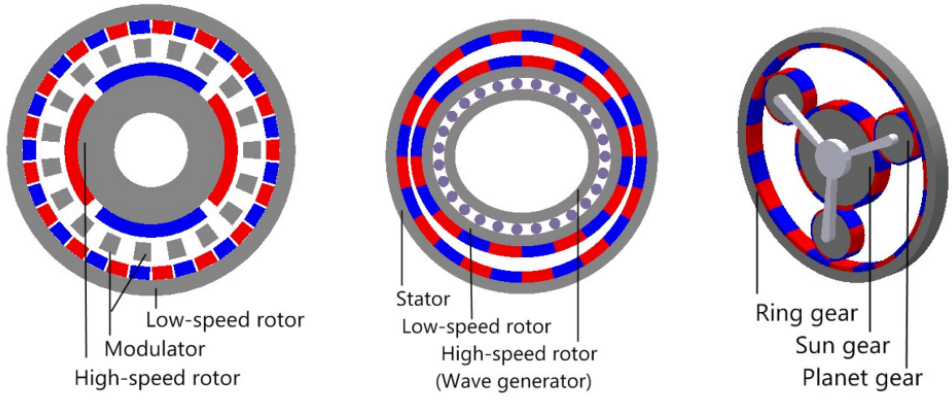

Figure 2.6: Left: flux modulated magnetic gear, middle: harmonic magnetic gear, right: planetary magnetic gear, (Tlali *et al.*, 2014).

2.3 Flux Modulated Magnetic Gears

In this section the FMMG topology is described, starting with the layout of the FMMG, followed by a review of its operating principles, and torque characteristics.

2.3.1 FMMG Layout

The general layout of the FMMG can be seen in Figure 2.7. The gear consists of the following major components:

- High-speed rotor.
- Ferromagnetic pole pieces.
- Low-speed rotor.
- Permanent magnets.
- Inner and outer yokes.

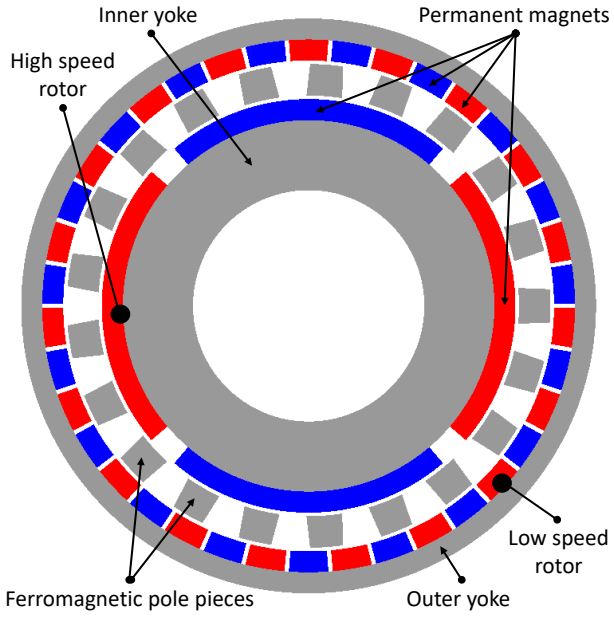

Figure 2.7: FMMG schematic layout.

The high-speed (HS) rotor, as its name implies, rotates at a higher speed compared to the modulator or the low-speed rotor. The high-speed rotor consists of permanent magnet pole pairs and an inner yoke. The inner yoke is made from a magnetically conductive material, i.e. steel. Some authors refer to the high-speed rotor as the inner rotor.

The ferromagnetic pole pieces are also made of a magnetically conductive material. These pole pieces are referred to as the modulator since the flux paths from the inner and outer permanent magnets are 'modulated' through them.

The low-speed (LS) rotor also consists of permanent magnet pole pairs and an outer yoke. The outer and inner yokes consist of the same material. Some authors refer to the low-speed rotor as the outer rotor.

The number of magnetic pole pairs in the low-speed rotor is usually higher than in the high-speed rotor and this determines the gear ratio (Atallah *et al.*, 2004). The number of ferromagnetic pole pieces is given to be a fixed relationship, given by equation 2.11. These relationships will be discussed in more detail in Sections 2.3.2 and 2.3.3.

Two movement arrangements are possible for the FMMG and will be referred to as case 1 and case 2. They are illustrated in Figure 2.8.

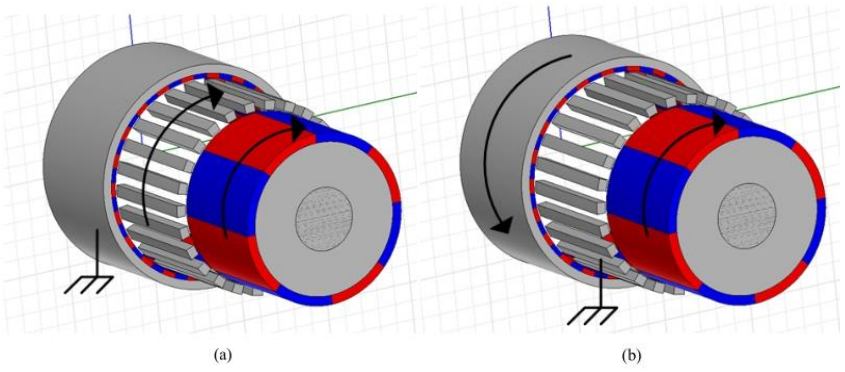

Figure 2.8: Operation options: (a) Low-speed rotor fixed. (b) Modulator fixed (Frank and Toliyat, 2009*a*).

For case 1, the low-speed rotor is fixed, i.e. $\Omega_{ls} = 0$, while the modulator and high-speed rotor are allowed to rotate freely, as seen in Figure 2.8 (a). The gear ratio for this case is given as

$$G_{r1} = -\frac{q_m}{p_{hs}} = -\frac{\Omega_m}{\Omega_{hs}} \tag{2.1}$$

where p_{hs} is the number of magnetic pole pairs on the high-speed rotor, q_m is the number of ferromagnetic pole pieces, Ω_{hs} is the rotational speed of the high-speed rotor, and Ω_m is the rotational speed of the modulator.

For case 2, the modulator is fixed, i.e. $\Omega_m = 0$, while the high-speed and low-speed rotors are allowed to rotate freely, as seen in Figure 2.8 (b). The gear ratio for this case is given as

$$G_{r2} = \frac{p_{ls}}{p_{hs}} = \frac{\Omega_{ls}}{\Omega_{hs}} \tag{2.2}$$

where p_{ls} is the number of magnetic pole pairs on the low-speed rotor, and Ω_{ls} is the rotational speed of the low-speed rotor.

From equations 2.1 and 2.2, for a given gear ratio, a higher torque can be transmitted for the arrangement in case 1. The negative sign for case 1 implies that the modulator and the high-speed rotor will rotate in the same direction, and will be discussed further in sections 2.3.2 and 2.3.3.

2.3.2 Principles of Operation

The relationship between the three major components and how they operate will be explained in this section. The key operating principle of the FMMG is the flux wave patterns and space-harmonics produced by the inner magnets and outer magnets, as illustrated in Figure 2.9a and 2.9b respectively. The magnetic fields of the same space-harmonic order interact and produce a stable torque in the FMMG. Thus, as the name implies, the FMMG works by modulating the flux of the inner and outer magnets. Figures 2.10a and 2.10b illustrate the flux paths of the magnetic field relative to the inner magnets and outer magnets, respectively.

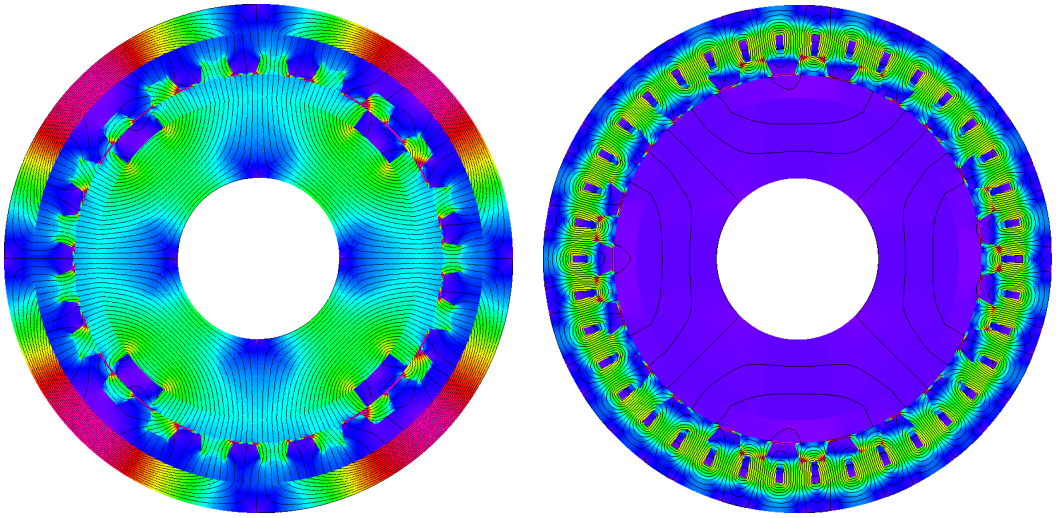

(a) (b)

Figure 2.9: Flux density distribution in an FMMG: (a) Field generated by inner magnets. (b) Field generated by outer magnets (Gerber, 2015).

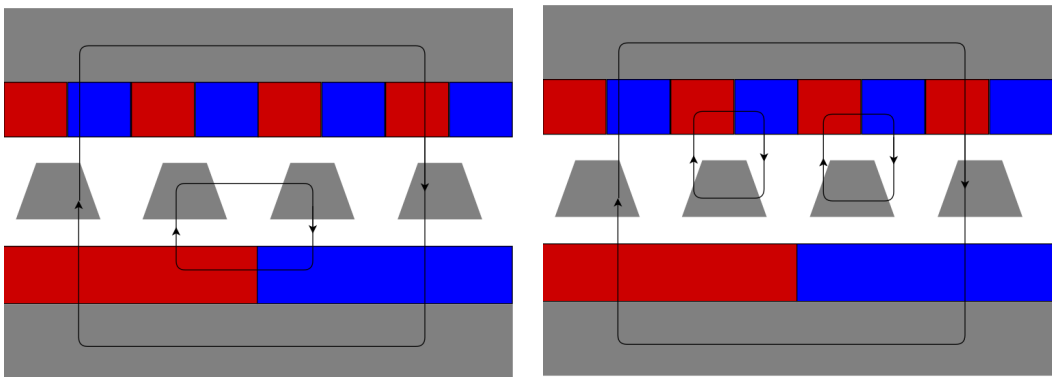

(a) (b)

Figure 2.10: FMMG Linear examples : (a) Flux path of the inner magnets. (b) Flux path of the outer magnets.

The magnetic flux density waveforms for the inner and outer air-gaps and their respective space harmonic content can be seen in Figure 2.11, where the gear under investigation has a p_{hs} value of 2, and p_{ls} value of 21, hence a gear ratio of 10.5:1 with the modulator fixed. The resulting FFT of the inner air-gap's waveform shows a prominent 2nd harmonic (see Figure 2.11b). Likewise, the FFT of the outer air-gap's waveform shows a prominent 21st harmonic, (Figure 2.11d).

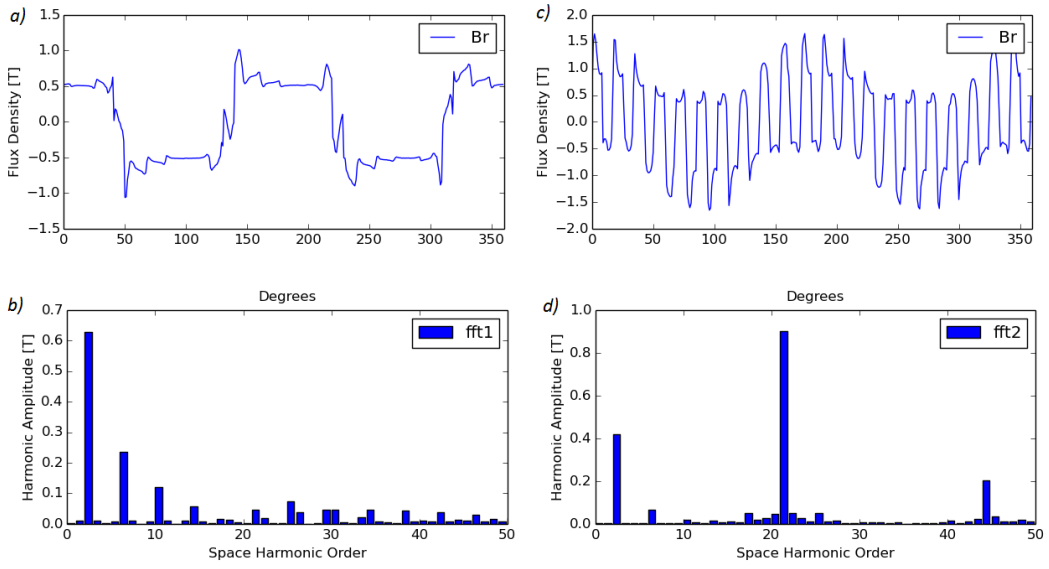

Figure 2.11: Magnetic flux distribution waveform: (a) Inner air-gap. (b) FFT of the inner waveform. (c) Outer air-gap. (d) FFT of the outer waveform (Matthee, 2016).

Figure 2.12 shows a schematic of an MG with and without inner bridges. Gerber and Wang (2013) and Frank and Toliyat (2011) have shown that adding a bridge to the inner modulator smoothes out the waveform, as seen in Figure 2.13a. Furthermore, as can be seen in Figure 2.13b the bridges can suppress undesired higher order harmonics (e.g. 21st and 25th harmonics) in the HS air-gap, which helps to minimise unwanted losses in the HS magnets and solid yoke (Gerber and Wang, 2013).

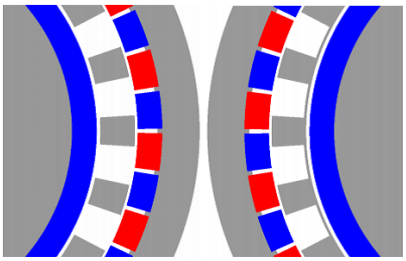

Figure 2.12: Bridge schematics (Gerber and Wang, 2013).

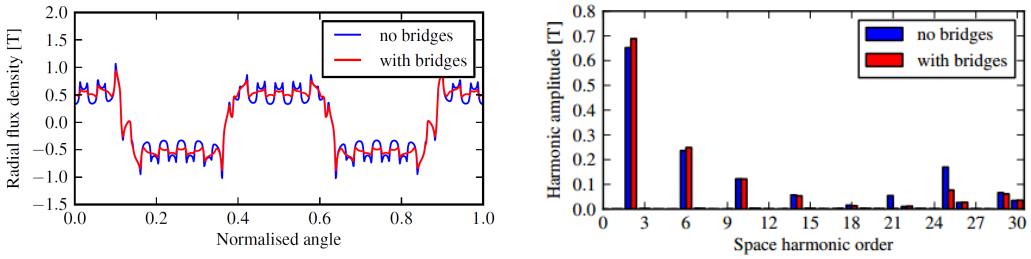

(a) (b)

Figure 2.13: Bridges vs. no bridges: (a) Radial flux density waveform in the HS air-gap due to HS magnets. (b) Space harmonics present in the HS air-gap (Gerber and Wang, 2013).

The flux density distribution produced by either of these two rotors at an arc radius r is given by Atallah *et al.* (2004) as

$$B_r(r,\theta) = \sum_{i=1,3,5,\ldots} b_{ri}(r)\cos(ip(\theta - \Omega_r t) + ip\theta_0) \tag{2.3}$$

for the radial component, and

$$B_\theta(r,\theta) = \sum_{i=1,3,5,\ldots} b_{\theta i}(r)\sin(ip(\theta - \Omega_r t) + ip\theta_0) \tag{2.4}$$

for the circumferential component, where $i = 1, 3, 5, ..., \infty$, p is defined as the number of permanent magnet pole-pairs, Ω_r is the rotational velocity of whichever rotor is analysed, b_{ri} and $b_{\theta i}$ are Fourier coefficients for the radial

and circumferential components of the flux density distribution, respectively. Furthermore, θ and θ_0 are the angular position and initial angular position, respectively, of the component under inspection, i.e. either HS or LS.

The ferromagnetic pole-pieces are introduced as a median for the flux to be controlled or modulated. Thus another term is introduced into equations 2.3 and 2.4 and the equations become

$$B_r(r,\theta) = \overbrace{\left(\sum_{i=1,3,5,\ldots} b_{ri}(r)\cos(ip(\theta-\Omega_r t)+ip\theta_0)\right)}^{\text{flux density distribution without ferromagnetic pole-pieces}} \times \overbrace{\left(\lambda_{r0}(r)+\sum_{j=1,3,5,\ldots}\lambda_{rj}(r)\cos(jq_m(\theta-\Omega_m t))\right)}^{\text{modulating function}} \tag{2.5}$$

for the radial component, and

$$B_\theta(r,\theta) = \overbrace{\left(\sum_{i=1,3,5,\ldots} b_{\theta i}(r)\sin(ip(\theta-\Omega_r t)+ip\theta_0)\right)}^{\text{flux density distribution without ferromagnetic pole-pieces}} \times \overbrace{\left(\lambda_{\theta 0}(r)+\sum_{j=1,3,5,\ldots}\lambda_{\theta j}(r)\cos(jq_m(\theta-\Omega_m t))\right)}^{\text{modulating function}} \tag{2.6}$$

for the circumferential component, where $j = 1, 3, 5, ..., \infty$, Ω_m is the rotational velocity of the ferromagnetic pole-pieces, q_m is the number of ferromagnetic pole-pieces, λ_{rj} and $\lambda_{\theta j}$ are Fourier coefficients for the modulating functions connected with the radial and circumferential components of the flux density distribution as a result of the ferromagnetic pole-pieces introduced. Equations 2.5 and 2.6 can be rewritten as

$$\begin{aligned} B_r(r,\theta) = {} & \lambda_{r0}\sum_{i=1,3,5,\ldots} b_{ri}(r)\cos(ip(\theta-\Omega_r t)+ip\theta_0) \\ & + \frac{1}{2}\sum_{i=1,3,5,\ldots}\sum_{j=1,3,5,\ldots}\lambda_{rj}(r)b_{ri}(r)\cos \\ & \left((ip+jq_m)\left(\theta-\frac{(ip\Omega_r+jq_m\Omega_m)}{(ip+jq_m)}t\right)+ip\theta_0\right) \\ & + \frac{1}{2}\sum_{i=1,3,5,\ldots}\sum_{j=1,3,5,\ldots}\lambda_{rj}(r)b_{ri}(r)\cos \\ & \left((ip-jq_m)\left(\theta-\frac{(ip\Omega_r-jq_m\Omega_m)}{(ip-jq_m)}t\right)+ip\theta_0\right) \end{aligned} \tag{2.7}$$

and

$$\begin{aligned} B_\theta(r,\theta) = \lambda_{\theta 0} \sum_{i=1,3,5,\ldots} b_{\theta i}(r)\sin(ip(\theta-\Omega_r t)+ip\theta_0) \\ + \frac{1}{2}\sum_{i=1,3,5,\ldots}\sum_{j=1,3,5,\ldots}\lambda_{\theta j}(r)b_{\theta i}(r)\sin \\ \left((ip+jq_m)\left(\theta-\frac{(ip\Omega_r+jq_m\Omega_m)}{(ip+jq_m)}t\right)+ip\theta_0\right) \\ + \frac{1}{2}\sum_{i=1,3,5,\ldots}\sum_{j=1,3,5,\ldots}\lambda_{\theta j}(r)b_{\theta i}(r)\sin \\ \left((ip-jq_m)\left(\theta-\frac{(ip\Omega_r-jq_m\Omega_m)}{(ip-jq_m)}t\right)+ip\theta_0\right) \end{aligned} \tag{2.8}$$

for the radial and circumferential components, respectively. Hence, the number of pole-pairs in the space harmonic flux density distribution generated by either rotor is given by

$$p_{i,k} = |ip + kq_m| \tag{2.9}$$

and the rotational velocity of the flux density space harmonics is thus

$$\Omega_{i,k} = \frac{ip}{ip+kq_m}\Omega_r + \frac{kq_m}{ip+kq_m}\Omega_m \tag{2.10}$$

where

$$i = 1, 3, 5, ..., \infty$$
$$k = 0, \pm1, \pm2, \pm3, ..., \pm\infty.$$

As described by Atallah *et al.* (2004), the velocity of the space harmonics is not the same as the velocity of any of the two rotors. Therefore, in order to transfer torque at a different rotational speed, the number of pole-pairs of any permanent magnet rotor must equal the number of pole-pairs of a space harmonic, where $k \neq 0$. Thus, for the highest asynchronous space harmonic to occur the following must be met $i = 1$, $k = -1$. As a result, equation 2.11 must be satisfied, which in effect gives the relationship between the number of ferromagnetic pole-pieces and the number of magnetic pole pairs on each rotor.

$$p_{ls} = q_m - p_{hs} \tag{2.11}$$

2.3.3 Torque characteristics

The underlying theory for the torque transfer in a magnetic gear can be found in Niguchi *et al.* (2010) and Gerber (2015). The Law of Conservation of Energy states:

"Energy cannot be created or destroyed, it can only be changed from one form to another."

In other words, energy is always converted from one form to another, and in this case, energy is converted from kinetic energy to magnetic energy and then converted back from magnetic to kinetic energy. From the law governing the transformation of magnetic energy to kinetic energy, the torque on a component within the magnetic gear can be expressed as

$$\tau(\theta) = -\frac{\partial W(\theta)}{\partial \theta} \tag{2.12}$$

where $W(\theta)$ is the magnetic energy and θ is the angular position of the component. Assuming that the system acts as an isolated system, in which the magnetic energy is stored only in the air gap, $W(\theta)$ can be calculated as follows

$$W(\theta) = \frac{1}{2\mu_0} \int_V B^2 dV \tag{2.13}$$

where μ_0 is the permeability in a vacuum, V is the volume of the air gap, and B is the magnetic flux density in the air gap. Thus, assuming the magnets have a permeability approximately equal to a vacuum, the flux density B can be shown to be

$$B(r, \theta) = \frac{\mathcal{FP}}{2\pi r_g L} = \frac{\phi(\theta)}{2\pi r_g L} \tag{2.14}$$

where L is the axial length of the air gap, or the stack length of the gear and r_g is the average air-gap radius. By substituting equation 2.14 into 2.13 the following equation can be obtained

$$W(\theta) = \frac{1}{2\mu_0} \int_\theta \int_r \int_z \frac{\phi^2}{(2\pi r L)^2} d\theta dr dz \tag{2.15}$$

After solving this integral the torque on the outer rotor with respect to its movement is calculated as the change in energy in both air-gaps and is given as

$$\tau_{ls} = \frac{\partial W_{inner}}{\partial \theta_r} + \frac{\partial W_{outer}}{\partial \theta_r} \tag{2.16}$$

which can further be expanded and shown to be

$$\tau_{ls} = -X p_{ls} \left(ln \frac{r_{m,inner}}{r_{ls,m,inner}} + ln \frac{r_{ls,m,outer}}{r_{m,outer}} \right) \sin(p_{hs}\theta_{hs} + p_{ls}\theta_{ls} - q_m \theta_m) \tag{2.17}$$

where X is made up of the following variables

$$X = \frac{L M_{hs} M_{ls} \mathcal{P}_{avg} \mathcal{P}_m}{8\mu_0 \pi^2}. \tag{2.18}$$

The torque on the inner rotor and the modulator can be derived in a similar manner and are given by equations 2.19 and 2.20, respectively.

$$\tau_{hs} = -Xp_{hs}\left(ln\frac{r_{m,inner}}{r_{ls,m,inner}} + ln\frac{r_{ls,m,outer}}{r_{m,outer}}\right)\sin(p_{hs}\theta_{hs} + p_{ls}\theta_{ls} - q_m\theta_m) \quad (2.19)$$

$$\tau_m = Xq_m\left(ln\frac{r_{m,inner}}{r_{ls,m,inner}} + ln\frac{r_{ls,m,outer}}{r_{m,outer}}\right)\sin(p_{hs}\theta_{hs} + p_{ls}\theta_{ls} - q_m\theta_m) \quad (2.20)$$

Thus from these equations the torque relationship in equations 2.1 and 2.2 are confirmed.

$$\tau_m = -\frac{q_m}{p_{hs}} = -G_{r1}\tau_{hs} \quad (2.21)$$

$$\tau_{ls} = \frac{p_{ls}}{p_{hs}} = G_{r2}\tau_{hs} \quad (2.22)$$

2.4 Mechanical Literature Review

The fourth and final boundary layer is the mechanical literature read during research for this thesis. This section provides background on the analysis and measurement of mechanical vibrations and consists of the following subsections: vibration background, measuring equipment, and common vibration analysis methods.

2.4.1 Vibration Background

The vibrational response of any mechanical system is dependent on the frequency, or rotational speed of the driven input. Vibration measurements are generally done to analyse two situations. The first is a surveillance mode for analysing the health of machinery on a routine basis and is commonly known as condition monitoring. The second situation is an analysis process where the main objective is to identify and fix a problem, this is generally done by analysing the forced excitation of machinery.

Natural Frequency: The natural frequency of an object is defined in Wowk (1991) as the frequency at which a system will oscillate if excited with an impulse. When the input driving force of a structural part operates close to its natural frequency the part will vibrate vigorously, this effect is known as resonance. For shafts or rotors, these operating speeds are typically called the critical speeds of the rotor. Harmonic frequencies are vibration frequencies which are integer multiples of the fundamental frequency. Figure 2.14 shows an overhung shaft and its first and second natural frequencies.

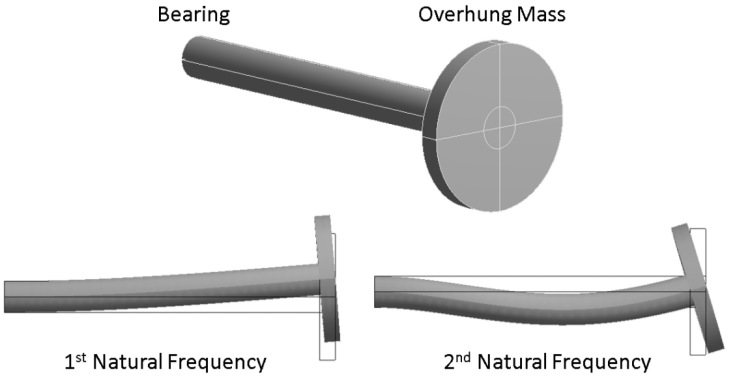

Figure 2.14: The first and second natural frequency of a shaft, or the two-shaft modes (Stamper, 2017).

Bearings frequencies: Roller bearings give off specific vibration frequencies. All ball bearings give off four distinct tones, namely:

1. Fundamental train frequency (FTF)
2. Ball spin frequency (BSF)
3. Outer race frequency (ORF)
4. Inner race frequency (IRF)

In condition monitoring, the amplitude of these tones is often used as an indication of the bearings condition. The formulas for calculating these frequencies are given in Wowk (1991) as

$$FTF = \frac{rps}{2}\left[1 - \frac{Bd}{Pd}\cos\phi_c\right] \tag{2.23}$$

$$BSF = \frac{Pd}{2Bd}(rps)\left[1 - \frac{Bd^2}{Pd}\cos^2\phi_c\right] \tag{2.24}$$

$$ORF = n_b(FTF) \tag{2.25}$$

$$IRF = n_b(rps - FTF) \tag{2.26}$$

where rps is the revolutions per second of the inner race, Bd is the ball diameter, Pd is the pitch diameter, n_b is the number of balls in the bearing, and ϕ_c is the contact angle of the ball bearings. For bearings with no thrust load, the contact angle can be assumed to be zero, which simplifies equations 2.23 and 2.24 to

$$FTF = \frac{rps}{2}\left[1 - \frac{Bd}{Pd}\right] \tag{2.27}$$

$$BS = \frac{Pd}{2Bd}(rps)\left[1 - \frac{Bd^2}{Pd}\right]. \tag{2.28}$$

It should be noted that these formulas are theoretical, and the calculated and measured bearing frequencies can differ as much as several hertz (Wowk, 1991). The frequencies for the bearings used in this thesis were acquired from SKF (2017).

Gear frequencies: The spectral gear patterns or gear signatures are often used as a reference to determine the condition of bearings and gears. Furthermore, significant forces are present at the surfaces of the meshing gear teeth and are caused by the teeth deflecting under load, and then relaxing when unloaded. Determining the gear-mesh frequency (GMF) of a gear is a common way of identifying the transmitting forces, as shown in Wowk (1991). The GMF is calculated as

$$GMF = \omega \times N_{teeth} \tag{2.29}$$

where ω is the running speed of the gear in Hz, and N_{teeth} is the number of teeth of the corresponding gear. It should be noted that there is only one GMF for two mating gears, and to clarify an example is give as

$$\begin{gathered} N_1 = 40 \\ N_2 = 10 \\ \text{gear ratio} = \frac{N_1}{N_2} \\ \omega_1 = 100\ Hz \\ \omega_2 = 100\ Hz \times GR = 400\ Hz \\ GMF = 100\ Hz \times 40 = 4000\ Hz \\ GMF = 400\ Hz \times 10 = 4000\ Hz. \end{gathered} \tag{2.30}$$

Fan frequencies: A phenomenon similar to the GMF occurs in fans and other fluid-handling machines. These frequencies occur due to pressure fluctuation as a vane passes a discontinuity within its chamber, and is known as the vane passing frequency (VPF). The VPF of a fan is calculated as

$$\text{VPF} = \omega \times N_{blades} \tag{2.31}$$

where ω is the running speed of the fan in Hz, and N_{blades} is the number of blades of the corresponding fan. The existence of VPF are expected and occur in the operation of all pumps and fans. They are usually not a problem unless they excite a resonance in the structure supporting the fan or cause an acoustic problem.

Magnetic gear frequencies: In MGs vibrations are generated by the electromagnetic force acting on a corresponding rotating component (Lee and Chang, 2017). These vibrations are also present in the external rotor of a permanent magnet synchronous motor which has a similar structure as an FMMG. Thus, for a rotating modulator the major force excitation frequency is given by Zuo *et al.* (2015) as

$$f_{excited,m} = \mu q_m f_{r,m} (\mu = 1, 2, 3, ...) \tag{2.32}$$

where q_m is the number of modulating pieces, and f_{r_m} is the rotational frequency of the modulator. Similarly, the main force excitation frequency for the high-speed rotor will be

$$f_{excited,high} = \mu p_{hs} f_{r,high} (\mu = 1, 2, 3, ...) \tag{2.33}$$

where p_{hs} is the number of pole pairs of the permanent magnets of the high-speed rotor and f_{r_high} is the rotational frequency of the high-speed rotor.

Motor frequencies: Electricity is distributed in South Africa at a frequency of 50 Hz, and the mechanical vibrations emanating from motors and transformers are at 100 Hz (Wowk, 1991). Furthermore, electric motors produce torsional vibrations, and it is likely to get linear vibrations at 50 Hz or multiples thereof.

2.4.2 Measuring Equipment

Piezoelectric accelerometers are commonly used to measure vibrations. This is because of its useful frequency measuring range (1 Hz to 2×10^4 Hz) (Wowk, 1991). The accelerometer is made from quartz crystal layers (barium titanate, a manmade quartz), with a mass bolted on top of the quartz and a spring compressing the mass and quartz. Figure 2.15 illustrates the internal components of a piezoelectric accelerometer. The quartz generates a charge output going positive and negative as the crystals are alternately compressed and relaxed about the load. This charge output is a faithful reproduction of the motion in the direction of the accelerometer's axis.

Accelerometers are practically unaffected by external electrical or magnetic fields (Wowk, 1991), and as a result are ideal for measuring the vibrations of an MG. The primary consideration for selecting an accelerometer is its sensitivity and corresponding frequency response. 100 $\mathrm{mV/g_0}$ sensitivity accelerometers

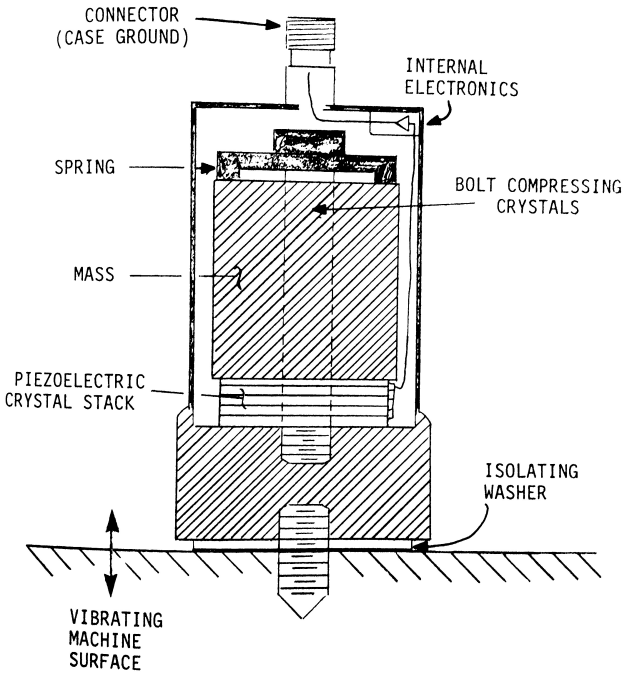

Figure 2.15: The internal construction of a piezoelectric accelerometer (Wowk, 1991).

provide the right balance of sensitivity and frequency response for most machinery monitoring.

Figure 2.16 illustrates the two general types of accelerometers, namely: the charge mode accelerometer and voltage mode accelerometer. The charge mode accelerometer requires a charge amplifier nearby, which provides the proper impedance matching. Furthermore, the accelerometer, cable and charge amplifier must be calibrated as a unit to ensure impedance matching (Wowk, 1991).

The voltage mode accelerometer has built-in impedance matching the internal electronics. Thus it only requires a power supply (typically batteries) to power the internal electronics. The voltage-mode accelerometers are labelled ICP (integrating circuit piezoelectric) by some manufacturers. However, elevated temperatures will damage the internal electronics and a charge-mode system should rather be used where the temperature could be an issue (Wowk, 1991).

2.4.3 Time and Frequency Domains

As mentioned, accelerometers generate vibration measurement in the time domain, namely a time signal. However, many other useful operators exist for analysing vibrations and the ones considered for this thesis are: fast-Fourier-transform (FFT), power-spectral-density (PSD), and a Spectrogram. These methods are all in the frequency domain which is one of the most powerful

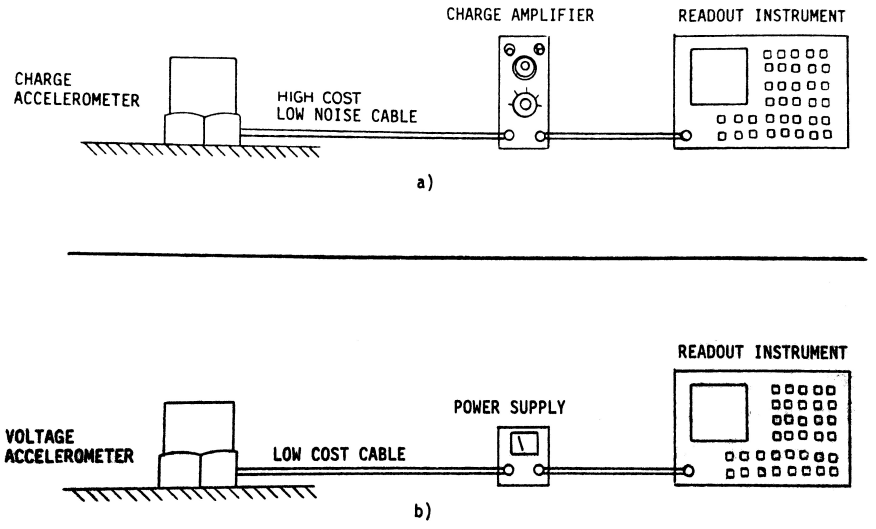

Figure 2.16: The two general types of piezoelectric accelerometer systems: (a) Charge mode accelerometer. (b) Voltage mode accelerometer (Wowk, 1991).

windows in machine monitoring and nearly all diagnostic and predictive maintenance instruments display vibrations in the frequency domain.

FFT: A fast Fourier transform is an efficient algorithm used to compute a discrete Fourier transform (DFT) (Hanly, 2016). As mentioned, FFT outputs vibration amplitude as a function of frequency. The frequency resolution is directly proportional to the signal length and sample rate.

PSD: A power spectral density is computed by multiplying each frequency bin in an FFT by its complex conjugate, thus resulting in only the real spectrum amplitude, in g_0^2. The key aspect of a PSD, which makes it more useful than an FFT for random vibration analysis, is that the amplitude value is normalised to the frequency bin width and the units become g_0^2/Hz. By normalising the result, the dependency on bin width is removed, allowing for comparison between vibration signals of different lengths (Hanly, 2016).

Spectogram: A spectrogram takes a series of FFTs and overlaps them to illustrate how the spectrum (frequency domain) changes over time (Hanly, 2016). If vibration analysis is being done in a changing environment, a spectrogram can be a powerful tool used to illustrate exactly how that spectrum of the vibration changes.

Chapter 3

Design Considerations

In this chapter both the electromagnetic and mechanical design aspects are investigated and discussed. First, the electromagnetic analysis of MG are discussed and the system losses in an MG are described. Then, a case study of the first prototype is presented, and finally, the design specifications for the second prototype are given.

3.1 Electromagnetic Analysis

For the design analysis of magnetic gears, several methods can be used (Tlali *et al.*, 2014), and three common methods are:

- Field solution-based analytical models: given by Jian *et al.* (2011), and Lubin *et al.* (2010).
- Reluctance network based analysis: given by Fukuoka *et al.* (2011), and Nakamura and Ichinokura (2008).
- Finite element analysis: given by Ge *et al.* (2012), and Gerber and Wang (2013)

The analytical methods have the advantage of being time efficient while providing insight into the electromagnetic solutions. However, they also have disadvantages such as not being able to account for saturation and intricate geometries. Thus, for the design and optimisation of magnetic gears, they are less suitable as mentioned in Tlali *et al.* (2014).

Reluctance network analysis (RNA) is a practical analysis method which uses an analytical model to solve magnetic circuits (Fukuoka *et al.*, 2011). Depending on the detail of the RNA model, reasonably high calculation accuracy can be achieved. The RNA method is not the most common method used for simulating a magnetic gear, however, it has been shown to have the ability to model the end effects of magnetic gears with good accuracy (Nakamura and Ichinokura, 2008).

Finite element method (FEM) is probably the most commonly used method for the electromagnetic design and analysis of a magnetic gear. This is because of the two distinct advantages of the FEM, namely the ability to account for the non-linearity in the ferromagnetic materials and the high accuracy in the performance calculations. One disadvantage of FEM-based dynamic analysis is the relatively high computational costs (Fukuoka *et al.*, 2011). However, since the results are accurate and software packages are readily available, this method will be used for the design and analysis of this research.

3.1.1 SEMFEM

Although various commercial FEM software packages are available for electromagnetic simulations, an in-house FEM package called SEMFEM was utilised for this project (Gerber, 2011). Figure 3.1 gives the flow diagram of SEMFEM. A FEM model of an MG is developed and executed in Python™ script, and output results are obtained. More information can be found on the webpage (Gerber, 2016). An important feature of SEMFEM is the ease of simulating the movement of the various components in the magnetic gear, as described by Gerber (2015).

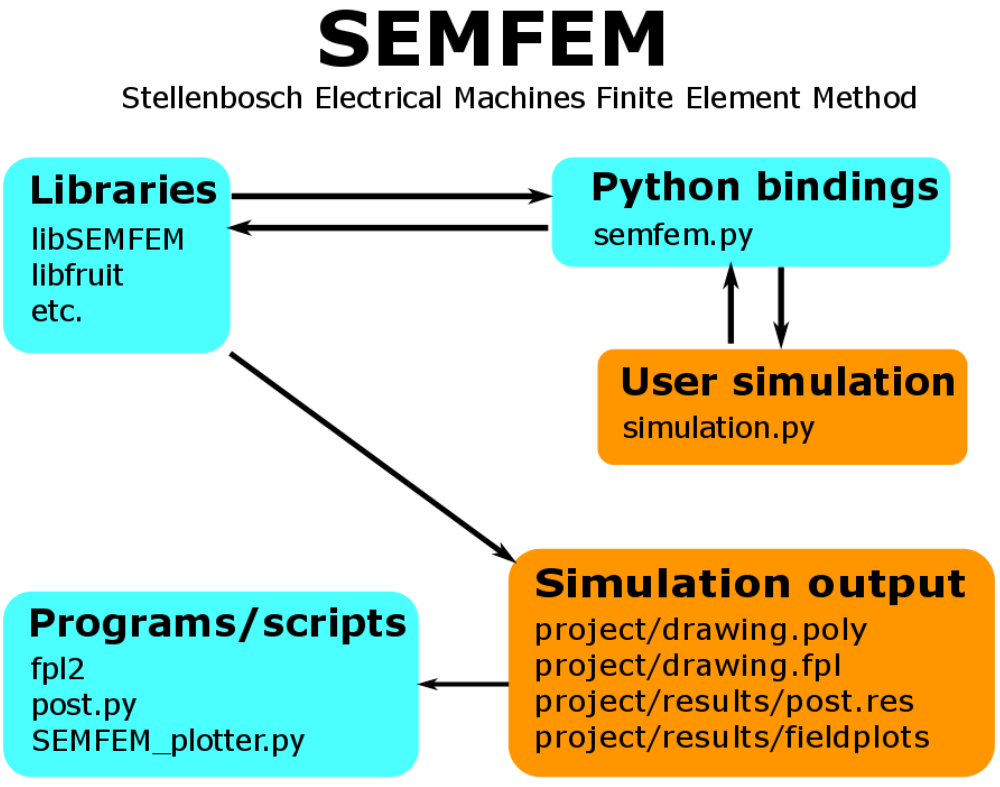

Figure 3.1: Flow diagram of SEMFEM (Gerber, 2016).

3.1.2 2D & 3D Effects of FEM

It is standard practice in the FE analysis of electrical machines to apply a 2D model rather than a 3D model and to make use of geometric symmetry to reduce the computational cost and complexity of the simulation model. However, a magnetic gear often does not exhibit periodic symmetry and therefore requires a full simulation model. As a result, the 2D simulation becomes computationally expensive and even more so a 3D simulation. Furthermore, if optimisation is applied to the design the computational expense of 3D FEA becomes prohibitively high. As a result, 2D FEA simulations will be done for the optimisation part of this project.

One common drawback of 2D FE analysis is that it overestimates the performance capability of the magnetic gear by a substantial amount, while 3D FE analysis has proven to give accurate performance predictions, as can be seen in Niguchi *et al.* (2010). This error is evident in literature where the authors, Ge *et al.* (2012), Rasmussen *et al.* (2005), Bronn *et al.* (2010), Liu *et al.* (2009*b*), and Gerber and Wang (2013), have all reported an error ranging between 20 % and 40 %. The source of this error is due to end-effects, which, as the name implies, occur at the end region of the gear. Further analysis of the end-effects in magnetic gears was done by Gerber and Wang (2014) and it was found that the end-effects are related to the aspect ratio (stack length to diameter ratio).

Figure 3.2 demonstrates the relationship between the aspect ratio, maximum torque capacity and torque density of a magnetic gear. The aspect ratio is defined as L/D, where L is the stack length of the gear and D is the outer rotor diameter. From Figure 3.2 it can be seen that the maximum torque for both a 2D and 3D model have a linear relationship with respect to the aspect ratio of the gear. As a result, an approximation of the difference in the 2D and 3D maximum torque can be made. Therefore, for the design of the prototype gear equation 3.1 will be applied to make up for this discrepancy rather than computing a 3D model.

$$\tau_{2D} = \frac{\tau_{rated}}{80} = \tau_{rated} \times 1.25 \tag{3.1}$$

Torque density (torque per volume) optimisation is often applied to magnetic gears to reduce the size of a gear. The torque density of an MG increases exponentially as L/D increases, as seen in Figure 3.2. This implies that there is little gain for an aspect ratio larger than 0.3. Therefore, increasing the stack length only has a significant advantage up to $L/D > 0.3$, with respect to the torque density. Furthermore, a long stack length is subjected to component deflection, due to strong oscillating magnetic forces, as seen in Fernando and Saha (2017).

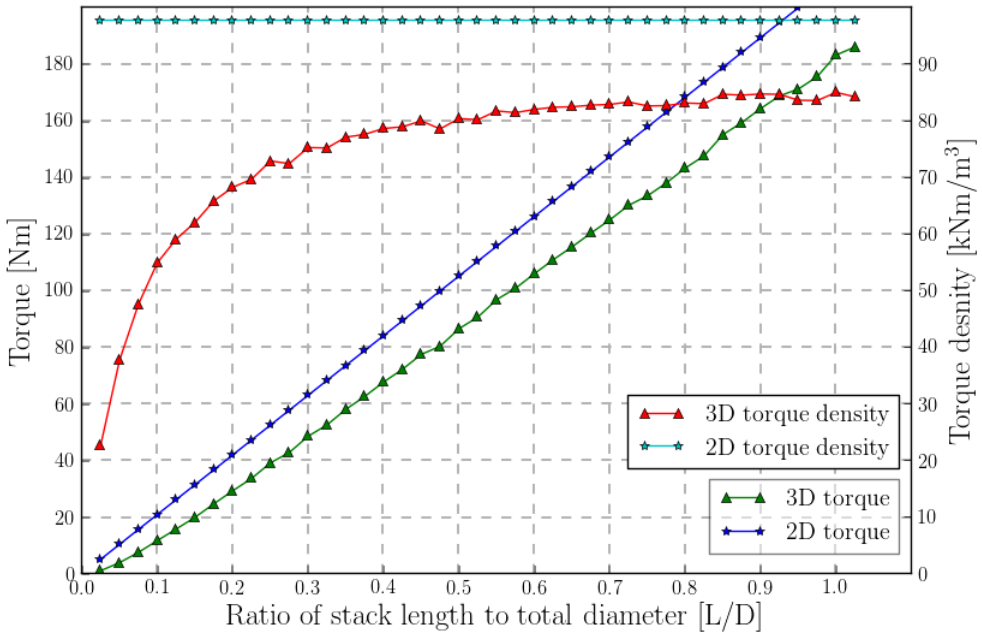

Figure 3.2: The end effect vs aspect ratio (Tlali, 2015).

Various studies have shown that the optimum point for 2D and 3D tend to be similar with respect to the maximum torque of the MG (Gerber and Wang, 2014). Figure 3.3 demonstrates the optimum point for the modulator thickness and maximum torque. This was done for various parameters of the magnetic gear and it was found that 2D FE analysis can be used to find optimum points for the stall torque.

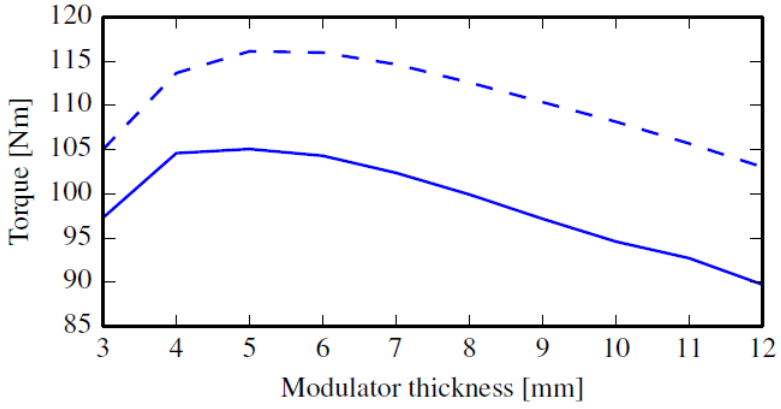

Figure 3.3: Torque vs modulator thickness of a magnetic gear (2D FEA: dashed, 3D FEA: solid) (Gerber and Wang, 2014).

3.1.3 Torque Ripple Analysis

Torque ripple refers to the periodic increase and decrease in the output torque as the output shaft rotates. Torque ripple is a common effect in many electric motor designs and magnetic gears. It is generally measured as the difference in the maximum and minimum torque over one complete period, as given by equation 3.2, and is generally expressed as a percentage (Emetor, 2017)

$$\tau_{ripple,\%} = \frac{\tau_{max} - \tau_{min}}{\tau_{avg}} \cdot 100\,\% \tag{3.2}$$

where τ_{max} is the maximum torque, τ_{min} is the minimum torque, and τ_{avg} is the average torque.

The torque ripple in magnetic gears may be caused by factors such as the airgap flux harmonics and mechanical imbalances, i.e. eccentricity of the rotor. As a design guidance, equation 3.3 is often used to determine the cogging factor of each rotor

$$f_c = \frac{2pq}{LCM(p,q)} \tag{3.3}$$

where, p is the number of pole-pairs of the rotor, q is the number of pole-pieces and LCM is the least common multiple between p and q. Due to the vast number of possible combinations of pole-pairs on the inner and outer rotor magnets, there are a wide variety of gear ratio possibilities. Various studies have been done with respect to the gear ratio and it has been found that fractional gear ratios produce a lower torque ripple effect, see Bronn *et al.* (2010), Frank and Toliyat (2009*b*), Frank and Toliyat (2009*a*), Wang *et al.* (2013).

As a result, fractional gear ratios have always been the prefered norm when selecting a gear ratio for an MG. However as seen in Chapter 4, there is another design factor to consider, namely, unbalanced magnetic forces (UMF). Thus, for this study selecting a gear ratio based on the UMF was more important and other methods for reducing the torque ripple were considered.

As can be expected, torque ripple in magnetic gears is undesirable, since the lifetime of the gear will be reduced due to the unwanted vibrations and noise generated. As a result, excessive torque ripple may require certain mitigation techniques such as skewing or changing the machine geometry that might reduce the general performance of the machine (Emetor, 2017). The skewing angle is related to the number of magnetic poles on the low-speed rotor and can be verified with simulations. Figures 3.4b and 3.4e show a normal high-speed rotor, while Figures 3.4a and 3.4d illustrate an ideally skewed high-speed rotor of which the tapered curve is continuous. However, due to the complex machining requirements skewing for MGs is often done in steps, as demonstrated in Figures 3.4c and 3.4f (Niguchi *et al.*, 2010).

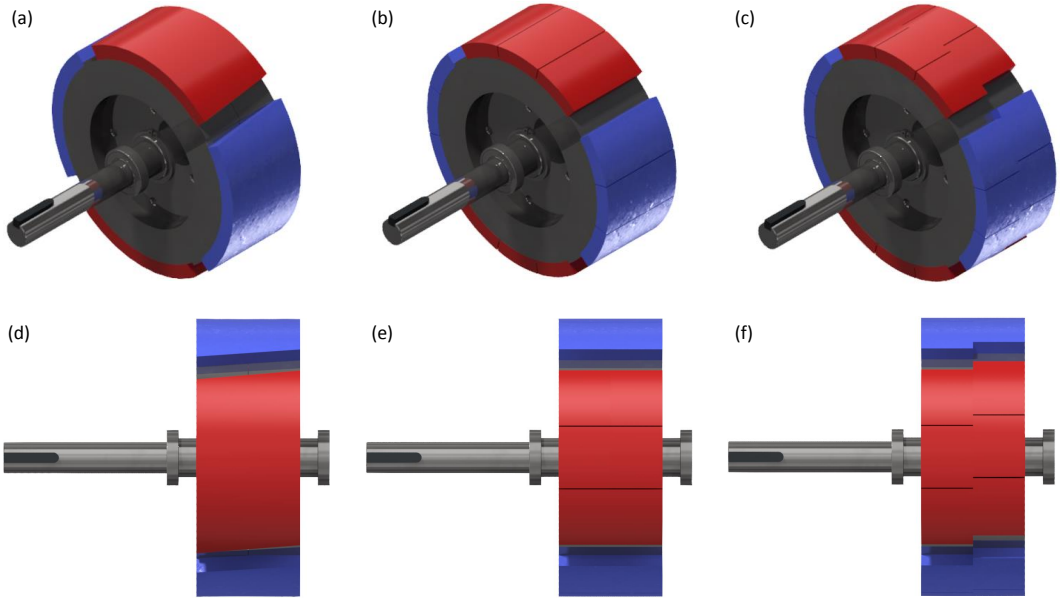

Figure 3.4: Example of skewing: (a) Ideal side view. (b) Normal side view. (c) Step skewed side view. (d) Ideal iso view. (b) Normal iso view. (c) Step skewed iso view.

3.2 System Loss Analysis

The losses present in a magnetic gear are similar to the losses present in other electrical machines and can be categorised into electromagnetic losses and mechanical losses, as illustrated in Figure 3.5.

3.2.1 Electromagnetic Losses

The electromagnetic losses can be further subdivided into hysteresis losses, eddy current losses, and excess losses. Though losses cannot be eliminated completely, the aim is to reduce the electromagnetic loss as far as possible. Although an in-depth electromagnetic analysis is not in the scope of this study, it is important to apply sound electromagnetic design principles.

Eddy Current Losses: Eddy currents can be defined as a circulating current induced in a conductive material by a changing electromagnetic field. As a result, eddy current losses occur when a time-varying magnetic field is applied to a material with high electric conductivity. Eddy current losses are proportional to the square of the frequency of the field variations, as given in Nair *et al.* (2016). As a result, components rotating at a high frequency are usually responsible for the most eddy current losses. Therefore, the electrical frequency of a magnetic gear should be kept low to prevent excessive losses, as suggested by Bronn *et al.* (2010).

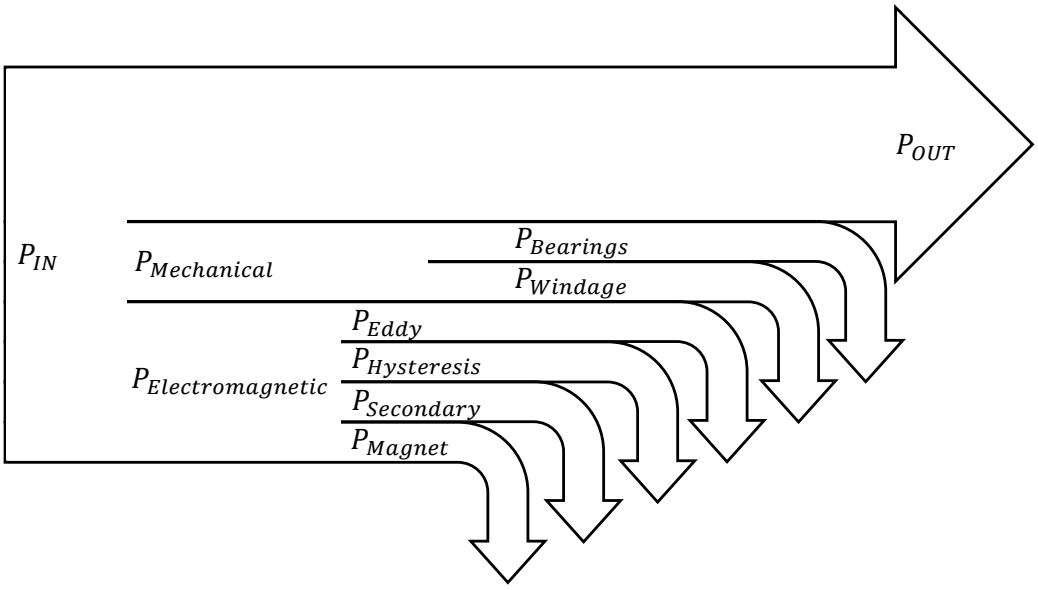

Figure 3.5: Losses present in magnetic gears.

One method for reducing eddy current losses in the active conductor is by laminating the conductor into thin layers. This restricts the eddy currents flowing in unwanted directions, as illustrated in Figure 3.6.

Another way to reduce eddy currents is by avoiding electrically conductive materials in areas where high-frequency magnetic flux passes through. For example, non-ferrous materials such as aluminium, copper etc., still generate eddy currents due to its high electric conductivity. Stainless steel is a non-ferrous material with low electric conductivity and low magnetic conductor, while materials such as plastic or ceramics are considered ideal.

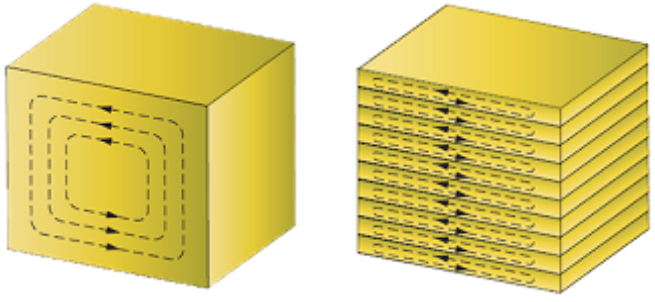

(a) (b)

Figure 3.6: Eddy current flow patterns: (a) Solid piece of metal. b) Laminated metal sheets (Gillet and Friedrich, 2015).

Hysteresis Losses: When a magnetic field is applied to a ferromagnetic material in one direction and then removed, it will not return to zero magnetisation along the same path. For it to return to zero, it must be driven in the opposite direction by a field. This effect is known as hysteresis and it is due to the existence of magnetic domains in the material. Once the magnetic domains are changed, it requires energy to turn them back again, as described by Nave (2016). The continuous movement of particles as they attempt to align with the varying field vector produce molecular friction, which can lead to heat loss (Integrated Publishing, 2017).

Secondary Losses: Magnetic gears can suffer large losses due to flux leakage from the magnets to any magnetic materials close to the passing flux fields. These losses were investigated in Gerber and Wang (2014) and the leakage is demonstrated in Figure 3.7. In the figure, the radial and axial component of the magnetic flux density is shown. Using appropriate material near the magnetic fields is essential to avoid these losses.

Magnet Losses: Most magnetic materials are also electrically conductive, and as a result, eddy currents are present in the magnets themselves. This can be reduced by segmenting the magnets rather than using large magnets with high losses.

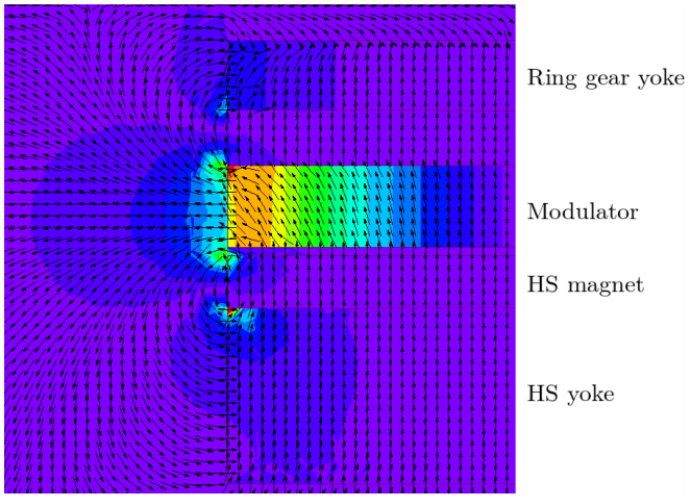

Figure 3.7: Side view of the gear showing the axial component of magnetic flux density, B_z (Gerber and Wang, 2014).

3.2.2 Mechanical losses

The mechanical losses generated in the magnetic gear generally consist of two components, namely bearing losses and aerodynamic losses, also called windage.

Bearing Losses: A typical bearing consists of five components namely: inner and outer rings with raceways, rolling elements, cage and seal (Harris, 2001). Bearing losses can be attributed to the contact friction between rotating parts within the bearings. Furthermore, bearing losses have two components, namely, rolling friction and sliding friction.

These frictions are caused by various factors during the operation of the bearing, namely: elastic hysteresis in rolling, sliding due to deformation between contacting elements, spinning of rolling elements, gyroscopic pivotal motion of the rolling elements, sliding between the cage and rolling elements, and sliding between the cage and bearing rings, viscous friction due to lubricant motion and seal friction, (Wrobel *et al.*, 2015). These effects are difficult to quantify due to their complexity and present methods for predicting bearing losses are based on empirical formulas, thus they do not account for specific applications (Wrobel *et al.*, 2015).

Another effect to keep in mind is electromagnetic losses within the bearing. The bearings are generally made of steel which is a magnetic material. If bearings are located near one of the high magnetic flux dense areas in the magnetic gear or electrical machine, eddy currents may be induced which causes heating of the bearing, thus increasing the frictional losses and decreasing the lifespan of the bearing.

Windage Losses: The aerodynamic losses can be attributed to the dynamic effects and friction of the air and machine rotors. However, windage losses can be neglected during low-speed operations and will only have a significant effect during high-speed operation, as given by Vrancik (1968), Chaari *et al.* (2012), and Wrobel *et al.* (2015).

3.3 Case Study

In this section a case study done on the first prototype magnetic gear is presented. The case study will cover the following: the first prototype's background, test setup, load performance evaluation, and a vibrational analysis.

3.3.1 First Prototype

The gear was designed by a masters' student from the Electrical Department of Stellenbosch University (Matthee, 2016). The design parameters for the first prototype are given in Appendix A.1. Figure 3.8 shows an exploded view of the gear with the three main components, namely the housing, the high-speed (HS) shaft, and the low-speed (LS) shaft.

During the testing of the fully assembled gear, it was discovered that the permanent magnet of the housing interfered with the LS rotor. As a result, the shafts did not rotate concentrically and in effect caused the air gap to be non-uniform. The origin of the problem was identified as neglecting an

alignment shoulder as part of the design (Matthee, 2016). Furthermore, the housing and permanent magnet carrier were assembled using threaded rods allowing the end plates to displace relative to each other. To address the issue, two aluminium rings where pressed over the gear to align the housing and the two casing side supports, as seen in Figure 3.9. However, this did not solve the problem completely and a swirl effect on the shafts was still observed. This was later identified to be caused by a large unbalanced magnetic force (UMF) and will be discussed further in Chapter 4.

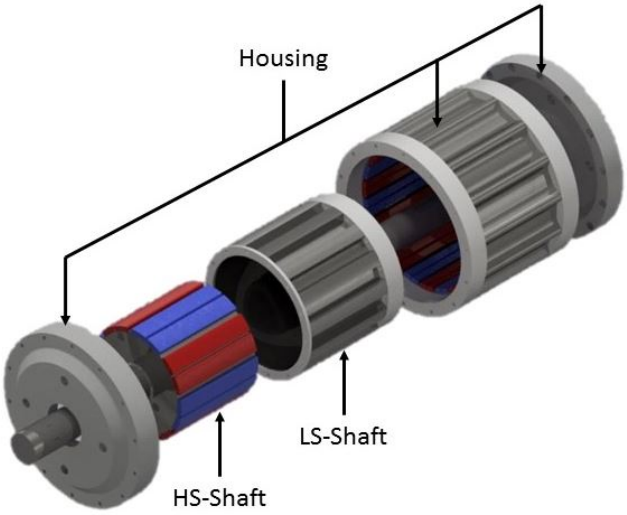

Figure 3.8: Exploded view of first prototype.

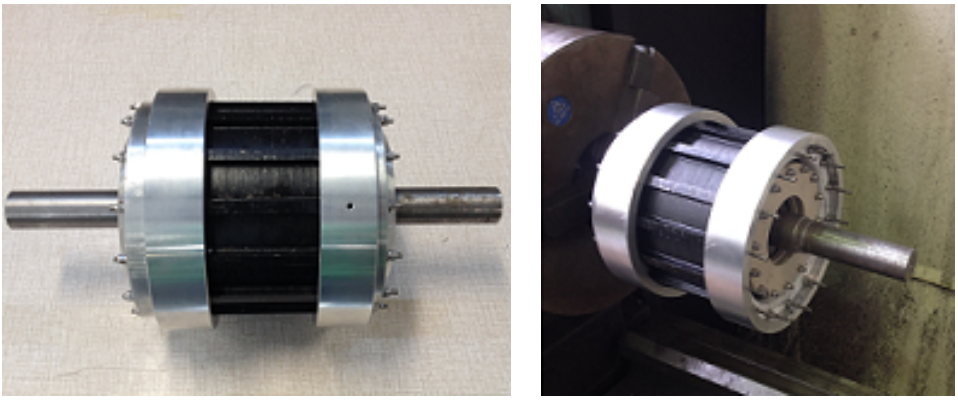

(a) (b)

Figure 3.9: Assembled first prototype MG: (a) Side view. (b) The assembling process showing the alignment rings (Matthee, 2016).

3.3.2 Test Setup

The performance of the magnetic gear was evaluated and compared to a mechanical counterpart. The test set-up for the magnetic gear consisted of the following equipment and can be seen in Figure 3.10.

1. Geared VSD induction motor.
2. Two Lorenz torque sensors.
3. Piezoelectric accelerometer.
4. Magnetic gear.
5. Second geared induction motor.

The geared variable speed drive (VSD) induction motor (1) acted as the prime mover of the system. The input, high-speed shaft, of the magnetic gear (4) was connected to the geared VSD induction motor (1). The output, low-speed shaft, of the magnetic gear (4) was connected to the geared VSD induction motor (5). The two Lorenz torque sensors (2) were placed in between the magnetic gear and the motors on both ends to measure the input and output speeds and torques. The second geared induction motor was operated in a regenerative mode and acted as an electrical load. The piezoelectric accelerometer (3) was fixed to the alignment ring with a grub screw. The torque and speed could be well controlled since an electrical load was used. Therefore the setup was ideal for testing the efficiency and vibrational effects of the gear at various loads.

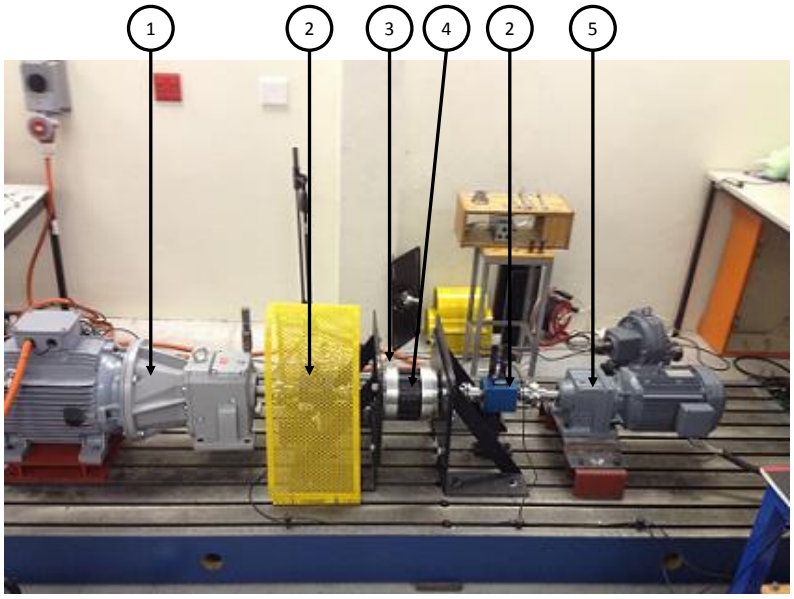

Figure 3.10: Testing layout of the magnetic gear (Matthee, 2016).

3.3.3 Load Performance Evaluation

The efficiency of the magnetic gear at $T_{ambient} = 20\,°C$, is presented at various power ratings and listed in Table 3.1. From Table 3.1 it can be seen that the efficiency of the gear varied from the lowest efficiency of 72.2 % to a maximum efficiency of 94.0 %, and the gear became more efficient as the load increased. For a more detailed temperature and efficiency comparison between the mechanical and magnetic gear see Matthee (2016).

Table 3.1: MG efficiency at various speeds and torques (Matthee, 2016).

Torque [Nm]	25	50	75	100	132
Speed [rpm]					
160	75.0	85.0	88.6	91.7	93.5
140	72.2	85.2	88.6	91.0	92.7
120	75.8	85.1	89.7	91.9	93.8
100	74.4	84.6	89.9	91.7	93.9
80	75.7	84.5	89.7	92.0	94.0

The no-load performance evaluation of the mechanical and magnetic gear is presented in Figure 3.11. From Figure 3.11 it can be seen that the magnetic gear suffered from unexpected no load-losses, from zero at start-up to a peak of 190 W at rated speed. It was suggested that these losses were due to the friction caused by the interference of the LS shaft and the carrier PM and high bearing losses.

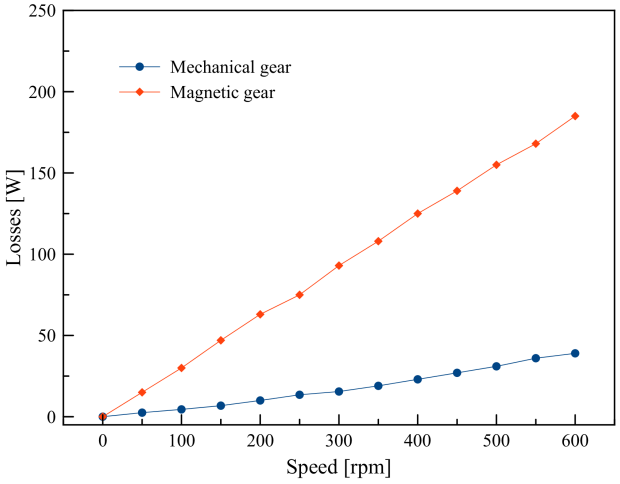

Figure 3.11: No-load losses for mechanical gear and magnetic gear (Matthee, 2016).

3.3.4 Vibration Results: First Prototype

The MG operated at its rated condition of 600 rpm, input speed, and rated power of 2.2 kW. A frequency measurement of 5 kHz was done to determine the frequency range, and it was observed that the most dominant frequencies were below 100 Hz. Thus, the frequency range was set to 100 Hz, and a sampling frequency of 200 Hz to avoid aliasing from occurring. Figure 3.12a shows a spectrogram of the MG which shows the integrity and quality of the measurement, while Figure 3.12b shows a PSD for the same signal. Figure 3.12a clearly shows the integrity of the measurement is constant over the entire reading. The peaks from Figure 3.12b can be identified from Table 3.2, where the most dominant frequency is the MG pole operating frequency at 40 Hz, and amplitude of $7\times10^{-3}\,g_0^2/\text{Hz}$.

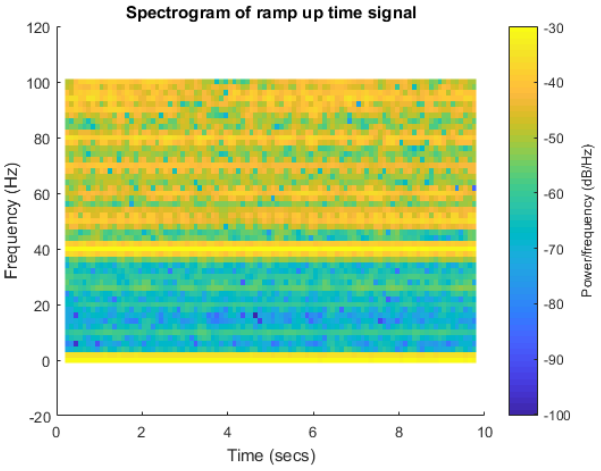

(a)

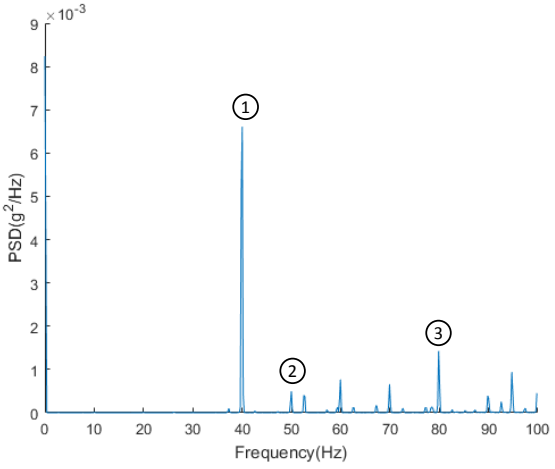

(b)

Figure 3.12: Vibration analysis at rated speed: (a) Spectrogram. (b) PSD.

Table 3.2: Frequencies to take note of at rated conditions.

Label	Description	Value	Unit
1	MG pole frequency	40	Hz
2	Motor frequency	50	Hz
3	2nd Harmonic of pole frequency	80	Hz

Figure 3.13 shows a series of the PSD plots at a constant torque of 132 N·m, while the speed vs. frequency is shown. Frequency is given on the x-axis, and speed is given on the y-axis. The PSD amplitude is shown on the z-axis. As the speed was increased the amplitude also increased and the most dominant frequency for all the measurements was found to be the MG pole frequency. It increased linearly with the speed from a frequency of 19.54 Hz at 80 rpm to a frequency of 39.06 Hz at 160 rpm. It can also be seen that at the speeds 120 rpm and 140 rpm the system goes through a resonance at a frequency 85.80 Hz and 97.66 Hz, respectively. Thus, operating at these speeds for long durations of time should be avoided to prevent damaging of equipment.

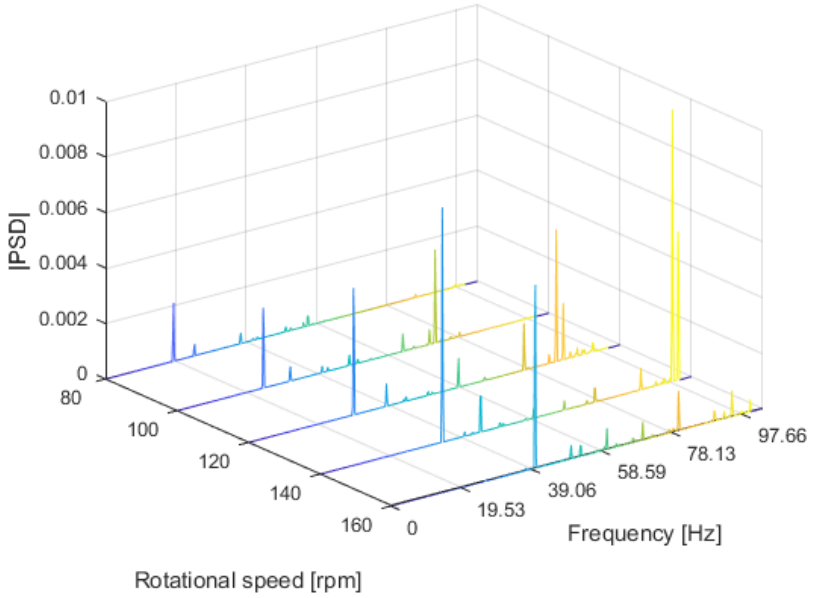

Figure 3.13: PSD plots at rated torque with varying speed.

Figure 3.14 shows a series of the PSD plots but this time with constant speed of 160 rpm and the torque vs. frequency shown. Once again the frequency is given on the x-axis, and the amplitude is shown on the z-axis. However, torque is given on the y-axis. From these figures, it can be clearly seen

how the amplitude increases with the operating speed. Also, it can be seen that the amplitude of the vibration is more dependent on the operating speed, as expected. Also, for a speed of 140 rpm, the system experienced higher frequencies at approximately 97 Hz. Therefore, this can be considered to be the natural frequency of the system.

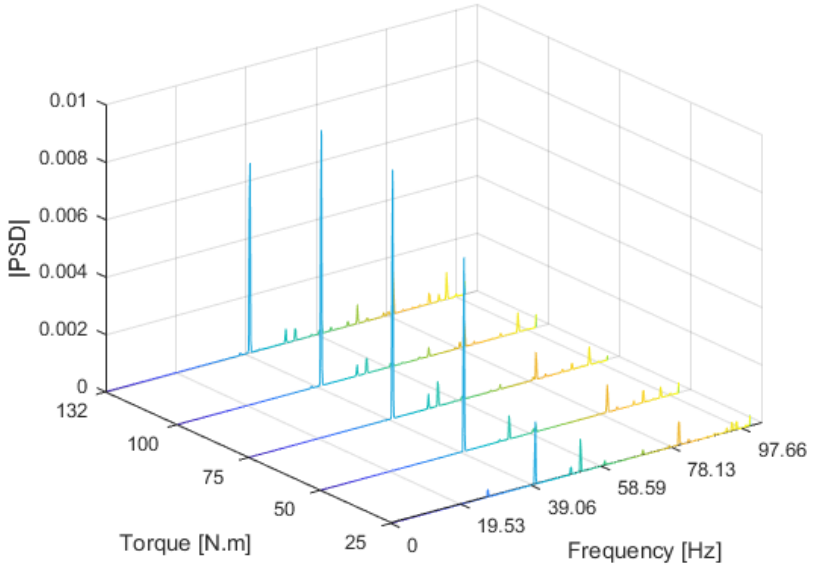

Figure 3.14: PSD plots at constant rated speed with varying torque.

3.4 Design Specifications

The specifications and design objectives of the second prototype of the MG will be discussed in this section, followed by a summary of the design considerations.

3.4.1 Design Layout & Objectives

Figure 3.15 gives a representation of the proposed design layout. The objective is to design an MG with a higher gear ratio of approximately 11:1, similar to the gear ratio of the mechanical gears used at the Medupi power station. Table 3.3 gives the required specifications for the fan that will be used. The calculations for determining some of these values are shown in Appendix B.1. Other design objectives for the second prototype are:

- Realisation of an MG with minimum UMF.
- Achievement of even higher efficiency.

- Mechanical design of a motor-gear interface.
- Ease of assembly and disassembly.
- Exploration of methods for reducing torque ripple.

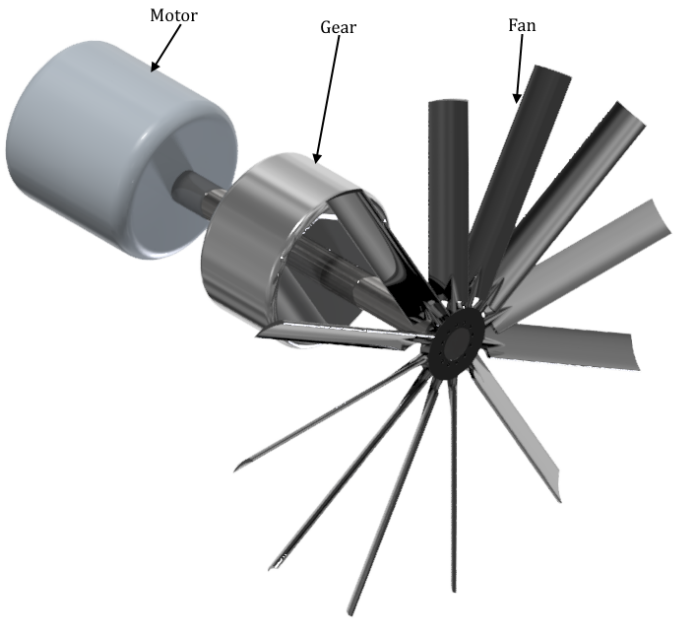

Figure 3.15: The design layout of the new prototype.

Table 3.3: Design specifications for second prototype.

Specification	Value	Unit
Fan Rated Power	2.2	kW
Fan Rated Speed	1500	rpm
FMMG Gear Ratio	± 11:1	-
Operating frequency	50	Hz
Output Rated Speed	1500	rpm
Output Rated Torque	14	N·m
Input Rated Speed	± 136	rpm
Input Rated Torque	± 154	N·m

3.4.2 Summary of Design Considerations

The designing of an MG requires various considerations and were discussed in this chapter. When choosing the specifications of an MG the most important features are summarised as follows:

- Gear ratio.
- Operating frequency.
- Cogging torque.
- Stall torque.

Appendix E provides a list of various gear ratio possibilities at an operating speed of 1500 rpm. The gear ratio of the MG is given by equations 2.1 and 2.2, in section 2.3.1. The fundamental operating frequency of an MG, at a specific speed, depends on which component is fixed. For a fixed outer ring, the frequency depends on the modulator speed. It is important to keep this frequency in check since the electromagnetic losses increase with a higher frequency. Also, eddy current losses can be reduced by laminating the modulator and choosing the appropriate materials in areas where high-frequency magnetic flux passes through.

Furthermore, the cogging torque of the gear is affected by the pole-pairs, or gear ratio, where a cogging factor of 1 is the ideal case. Another consideration for an MG is the stall torque which is affected by the magnet volume. Before a specific gear ratio was chosen, a study was done on how the internal forces of an MG are affected by the design selection, see Chapter 4.

Chapter 4

Force Analysis

As discussed in Chapter 3, fractional gear ratios are usually preferred for FMMGs in order to realise smooth torque transmission. However, for FMMGs with fractional gear ratios, there is usually no magnetic symmetry, which can lead to unbalanced magnetic forces. The relationship between the magnetic forces of the three concentric components of an FMMG, as shown in Figure 4.1, are analysed in this chapter.

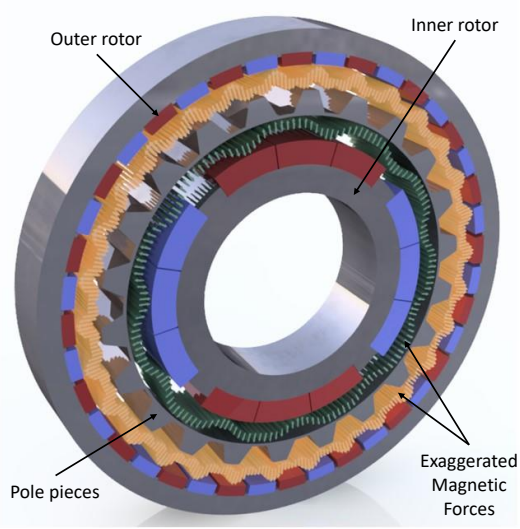

Figure 4.1: Illustration of the FFMG and the forces, with exaggerated air gaps.

4.1 Maxwell Stress Tensor Theory

The Maxwell stress tensor is often used to calculate electric and magnetic forces on objects. For magnetostatic forces, the total force on an object may be expressed in terms of volume integral of the force density as follows:

$$\vec{\boldsymbol{F}} = \int_V \vec{\boldsymbol{f}} dV \tag{4.1}$$

where the force density equation $\vec{\boldsymbol{f}}$ is defined in Furlani (2001) as

$$\vec{\boldsymbol{f}} = \frac{1}{\mu} \nabla \cdot \mathbb{T}. \tag{4.2}$$

The Maxwell stress tensor $\mathbb{T}$ is defined as

$$\begin{aligned}\mathbb{T} = T_{xx}\hat{\mathbf{x}}\hat{\mathbf{x}} + T_{xy}\hat{\mathbf{x}}\hat{\mathbf{y}} + T_{xz}\hat{\mathbf{x}}\hat{\mathbf{z}} + T_{yx}\hat{\mathbf{y}}\hat{\mathbf{x}} + T_{yy}\hat{\mathbf{y}}\hat{\mathbf{y}} + T_{yz}\hat{\mathbf{y}}\hat{\mathbf{z}} \\ + T_{zx}\hat{\mathbf{z}}\hat{\mathbf{x}} + T_{zy}\hat{\mathbf{z}}\hat{\mathbf{y}} + T_{zz}\hat{\mathbf{z}}\hat{\mathbf{z}}\end{aligned} \tag{4.3}$$

where $\hat{\mathbf{x}}$, $\hat{\mathbf{y}}$, and $\hat{\mathbf{z}}$ are the Cartesian unit vectors. Then it follows from equation 4.2 that

$$\begin{aligned}\vec{\boldsymbol{f}} = \frac{1}{\mu}\Bigg\{\left(\frac{\partial T_{xx}}{\partial x} + \frac{\partial T_{xy}}{\partial y} + \frac{\partial T_{xz}}{\partial z}\right)\hat{\mathbf{x}} + \left(\frac{\partial T_{yx}}{\partial x} + \frac{\partial T_{yy}}{\partial y} + \frac{\partial T_{yz}}{\partial z}\right)\hat{\mathbf{y}} \\ + \left(\frac{\partial T_{zx}}{\partial x} + \frac{\partial T_{zy}}{\partial y} + \frac{\partial T_{zz}}{\partial z}\right)\hat{\mathbf{z}}.\end{aligned} \tag{4.4}$$

Furthermore, from Furlani (2001) if a linear media is considered with a constitutive relation $\vec{\boldsymbol{B}} = \mu\vec{\boldsymbol{H}}$, the components of $\mathbb{T}$ are given as

$$[\mathbb{T}] = \begin{bmatrix} T_{xx} & T_{xy} & T_{xz} \\ T_{yx} & T_{yy} & T_{yz} \\ T_{zx} & T_{zy} & T_{zz} \end{bmatrix} = \begin{bmatrix} (B_x^2 - \frac{1}{2}|B|^2) & B_xB_y & B_xB_z \\ B_yB_x & (B_y^2 - \frac{1}{2}|B|^2) & B_yB_z \\ B_zB_x & B_zB_y & (B_z^2 - \frac{1}{2}|B|^2) \end{bmatrix}. \tag{4.5}$$

Subtituting equation 4.2 into 4.1 gives

$$\vec{\boldsymbol{F}} = \frac{1}{\mu}\int_V \nabla \cdot \mathbb{T} dV. \tag{4.6}$$

From the Divergence theorem, equation 4.6 can be written as a surface integral, namely:

$$\vec{\boldsymbol{F}} = \frac{1}{\mu}\oint_S \mathbb{T} \cdot \hat{\mathbf{n}} dS \tag{4.7}$$

where μ is the permeability of the medium through which the integration takes place, $\hat{\mathbf{n}}$ is the outward unit normal to the bounding surface, and the integration is performed over a surface S immediately surrounding the body. In principle, S should be the surface of the body itself. However, in practice (especially in FEA), S usually encompasses the body but is slightly offset from its surface, as discussed in Furlani (2001).

It is common in FEA to have these forces in cylindrical coordinates, as

$$F_r = \frac{L}{2\mu_0} \oint_l (B_r^2 - B_t^2) dl \tag{4.8}$$

$$F_t = \frac{L}{\mu_0} \oint_l B_r B_t dl \tag{4.9}$$

where L is the stack length of the MG, B_r is the radial magnetic-flux density, B_t is the tangential magnetic-flux density, and μ_0 the magnetic permeability of the air gap. This method is quite common and was used by Islam and Husain (2009) and Lee and Chang (2017) for force computations.

4.2 Magnetic Field Solution

In this section the following will be investigated: Firstly, the formulation of the magnetic field problem and the vector field solution of an FMMG are discussed. Then the transformation of these vectors from cylindrical coordinates to Cartesian coordinates are discussed. Finally, how the vector magnitudes and directions were verified is discussed.

4.2.1 Governing Equations

For finite element analysis of general electric machines, the 2D Cartesian representation of a magnetic field may be expressed in Poisson's equation as follows:

$$\frac{\partial}{\partial x}\left(\nu \frac{\partial \vec{\boldsymbol{A}}}{\partial x}\right) + \frac{\partial}{\partial y}\left(\nu \frac{\partial \vec{\boldsymbol{A}}}{\partial y}\right) = -\vec{\boldsymbol{J}} \tag{4.10}$$

where $\vec{\boldsymbol{A}}$ is the magnetic vector potential, $\vec{\boldsymbol{J}}$ is the current density and ν is the inverse of magnetic permeability. Using variational techniques, the partial differential equations of the field problem can be expressed by the energy functional F_e.

$$F_e = \int \int_S \left[\int_0^B \vec{\boldsymbol{H}} \cdot \vec{\boldsymbol{B}} - \vec{\boldsymbol{J}} \cdot \vec{\boldsymbol{A}} \right] dS \tag{4.11}$$

where $\vec{\boldsymbol{B}}$ and $\vec{\boldsymbol{H}}$ are the magnetic flux density and magnetic field intensity, respectively. The field problem from equation 4.10 may be solved by minimising equation 4.11.

4.2.2 Mesh and Boundary Conditions

In FEM simulation's mesh size directly affects the accuracy and the computational time of the simulation. Usually, fine meshes are applied to areas where high accuracy is required while coarse meshes are used for less critical areas.

Figure 4.2 shows a meshed FMMG FE model. A mesh dependency and sensitivity analysis was done and the converged mesh sizes are given in Table 4.1. Since a full FE model is used, only a Dirichlet boundary condition is applied to the outer periphery of the FE model.

Table 4.1: Simulation mesh.

Description	Mesh Size	Description
Mesh 1	(0.002)	Inner and outer yokes, air boundaries.
Mesh 2	(0.0005)	Magnets and modulator.
Mesh 3	(0.00025)	Air gaps.

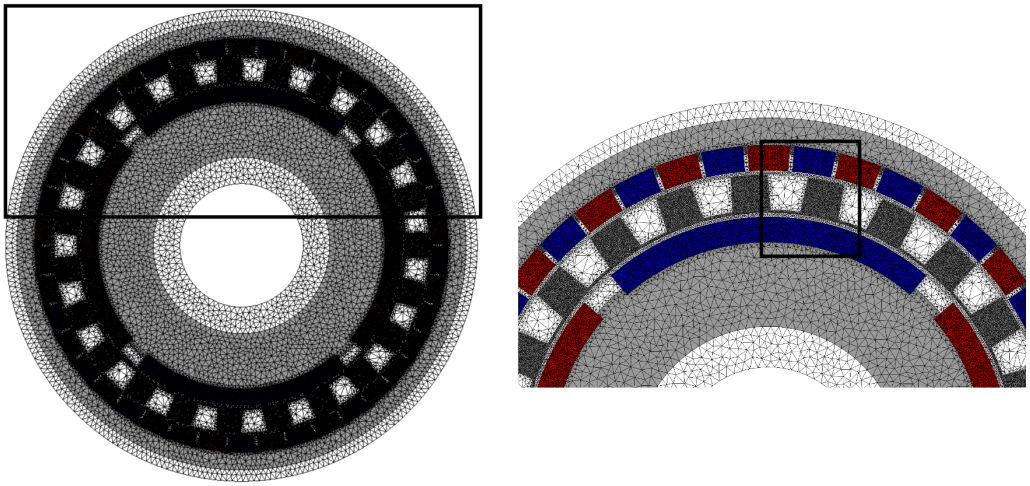

(a) Full scale view (b) Zoomed scale view

Figure 4.2: Two views of the 2D meshed simulation model.

4.2.3 Maxwell Stress Tensor Method

As mentioned, determining the magnetic forces requires knowledge of the Maxwell stresses along the circumference of each component. These stresses were obtained from a SEMFEM simulation model, and the initial parameters used for the simulation are given in Table A.2, in Appendix A.2. To compute the forces, the stresses need to be integrated over a closed surface, which reduces to a closed path in a 2D Cartesian problem. Figure 4.3 shows two closed paths (B1-B2) used in the study.

Since the modulator experiences forces from both inner and outer PMs, the resultant force acting on the modulator is of particular interest for this study. As a result, the integration paths B1 and B2 will be analysed in detail.

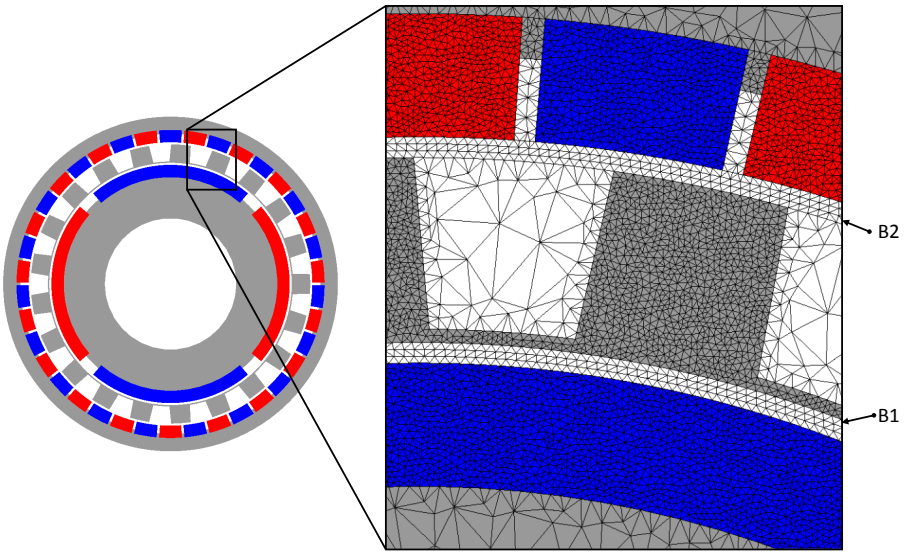

Figure 4.3: Integration paths in the FE model of the FMMG.

Figures 4.4a and 4.4b show the space distribution of radial and tangential components of the stress along B1, respectively. Similarly, Figure 4.5 shows the radial and tangential stress components along B2.

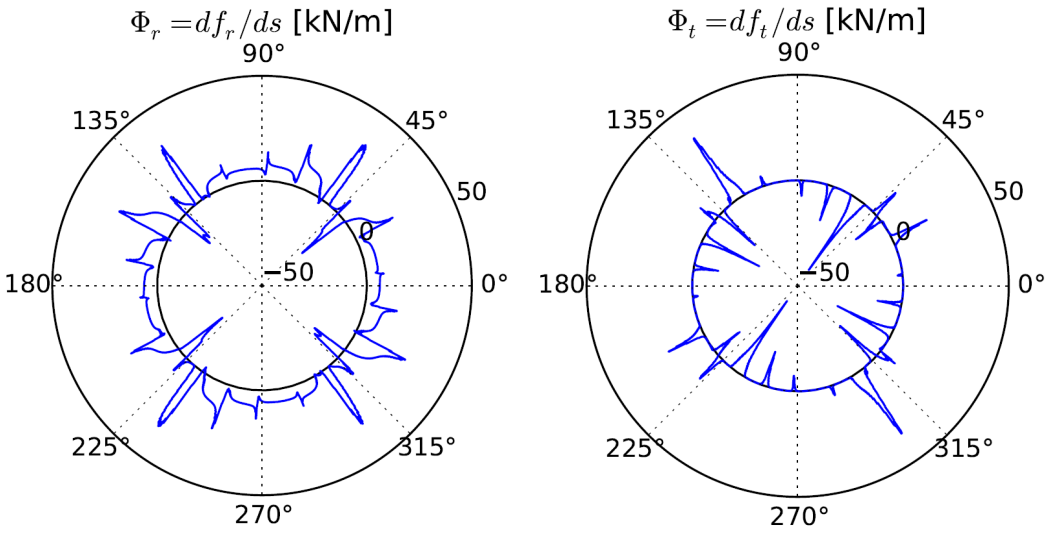

(a) (b)

Figure 4.4: Vector potentials for B1: (a) Radial. (b) Tangential.

4.2.4 Conversion to Cartesian Components

To calculate the resultant forces, the stress components obtained in cylindrical coordinates can be transformed to Cartesian coordinates. Figure 4.6

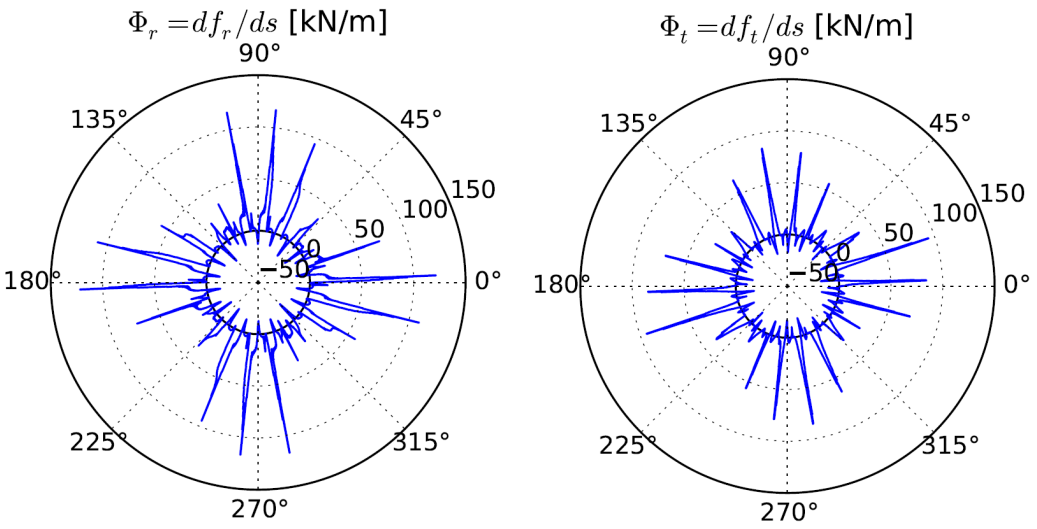

(a) (b)

Figure 4.5: Vector potentials for B2: (a) Radial. (b) Tangential.

illustrates the transformation of a stress component, where ϕ_r is the radial component, ϕ_{t_ccw} and ϕ_{t_cw} are the tangential components in the counter clockwise (CCW) and the clockwise directions (CW), respectively, ϕ_R is the resultant stress, while ϕ_x and ϕ_y are the corresponding xy components. The transformation matrix for CCW rotation is given by matrix 4.12 and for CW rotation by matrix 4.13.

$$CCW : \begin{bmatrix} \phi_x \\ \phi_y \end{bmatrix} = \begin{bmatrix} +\cos\theta & -\sin\theta \\ +\sin\theta & +\cos\theta \end{bmatrix} \begin{bmatrix} \phi_t \\ \phi_r \end{bmatrix} \tag{4.12}$$

$$CW : \begin{bmatrix} \phi_x \\ \phi_y \end{bmatrix} = \begin{bmatrix} +\cos\theta & +\sin\theta \\ -\sin\theta & +\cos\theta \end{bmatrix} \begin{bmatrix} \phi_t \\ \phi_r \end{bmatrix} \tag{4.13}$$

SEMFEM defines CCW rotation as positive, thus matrix 4.12 is used for the vector transformation.

To ensure the correctness of the vector conversion, two verifications were conducted, i.e.: force magnitude verification and transformation verification.

Force Magnitude Verification: The force magnitudes were verified by comparing the torque calculated using Coulomb's virtual work method to the torque calculated by multiplying the tangential force in each air-gap contour with the corresponding radius. This comparison can be seen in Table 4.2, along with the calculated resultant forces. As can be seen, the torque calculated in each air-gap contour compared well to the torque from the simulation output.

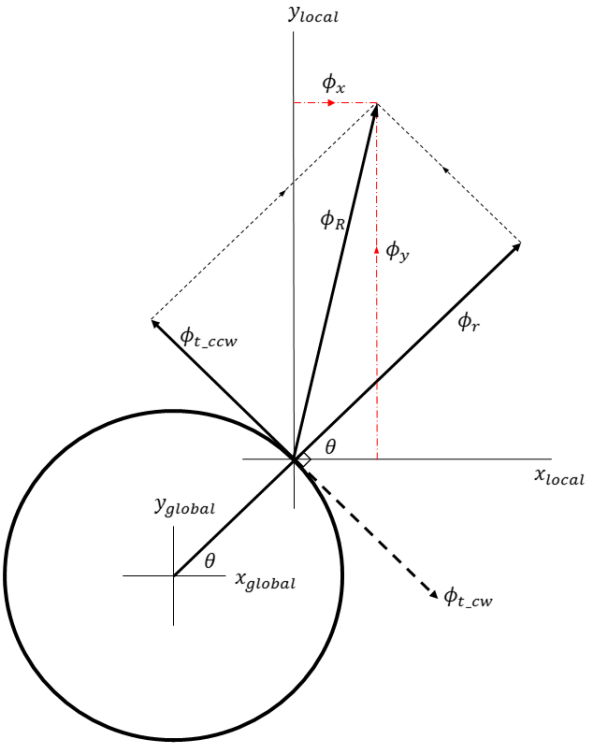

Figure 4.6: Illustration of stress transformation from radial and tangential to x and y.

Transformation Verification: The transformation verification was done to ensure that the vector components were transformed correctly from the cylindrical coordinates to Cartesian coordinates. From Figure 4.6 it can be seen that the magnitude of the resultant vectors are the same and are given by equation 4.14.

$$\phi_R = \sqrt{\phi_r^2 + \phi_t^2} = \sqrt{\phi_x^2 + \phi_y^2}. \tag{4.14}$$

Figure 4.7 shows the resultant vectors for the coordinate system in boundary layer B1. A similar result was obtained in boundary layer B2, thus the figure shows that the vectors were transformed correctly.

Table 4.2: Torque Comparison.

Boundary Layer	Simulated Torque [N·m]	Calculated Torque [N·m]	Resultant Force [N]
B1	24.33	24.31	32.68
B2	255.07	255.03	12.56

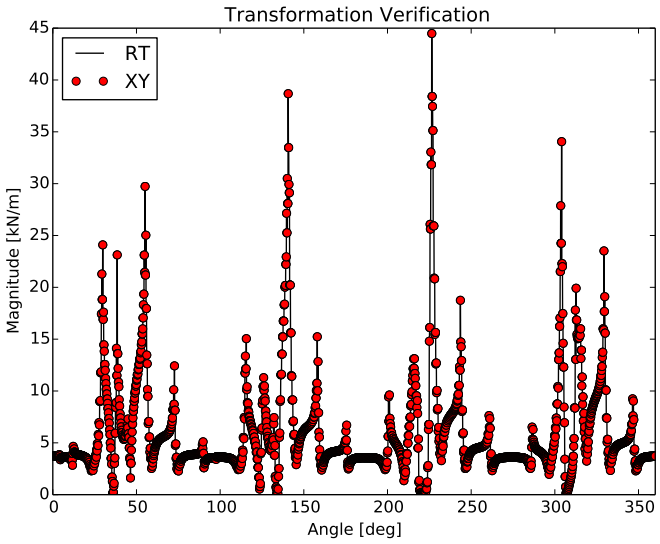

Figure 4.7: The transformation verification in B1.

4.3 Force Integration

The resultant force in each air-gap contour was calculated by applying the Maxwell stress tensor method as discussed in section 4.1, with a Python™ script and $4{\times}10^4$ sample points. As a result, the total tangential force was calculated from equation 4.9 and multiplied with the arc radius to calculate the torque, as seen in Table 4.2. Then, by applying the transformation matrix 4.12 the forces in the x and y directions were obtained. This was done for B1 and B2 and the sum of the resultant forces were determined by adding the x and y forces, as given by equations 4.15 and 4.16, respectively. Furthermore, the magnitude and angle of the resultant force due to both air gaps was determined by applying equations 4.17 and 4.18, respectively. This is demonstrated for an outer pole pair of 23 and 25, as seen in Figure 4.8a and Figure 4.8b.

$$F_{Tx} = F_{B1x} + F_{B2x} \tag{4.15}$$

$$F_{Ty} = F_{B1y} + F_{B2y} \tag{4.16}$$

$$F_R = \sqrt{F_{Tx}^2 + F_{Ty}^2} \tag{4.17}$$

$$\theta = arctan2(F_{Ty}, F_{Tx}). \tag{4.18}$$

The HS rotor was rotated in steps of 22.5° and the resultant forces for the first 90° are plotted in Figures 4.9a and 4.9b, respectively. Comparing these two figures shows that the gear ratio influences the magnitude of the resultant forces significantly.

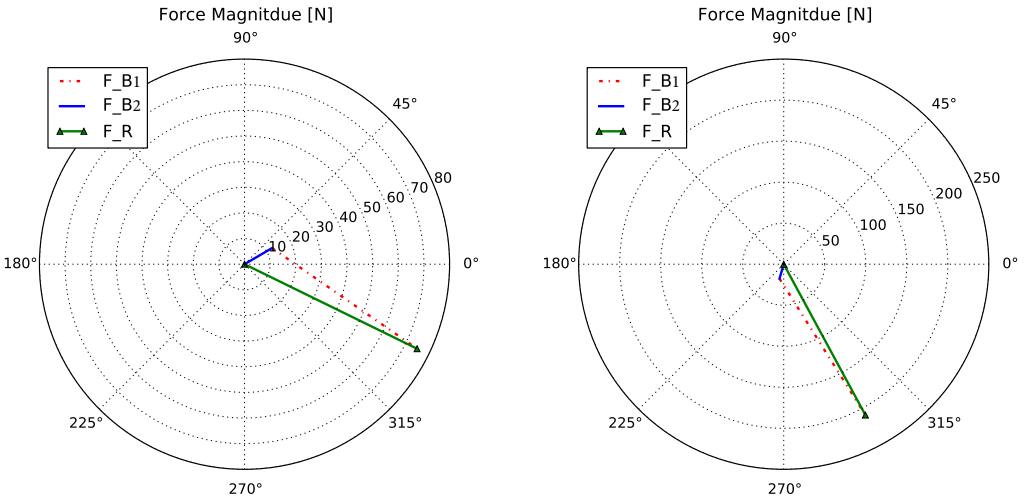

(a) (b)

Figure 4.8: Two views of the maximum resultant vectors: (a) 23 outer magnet pole pairs. (b) 25 outer magnet pole pairs.

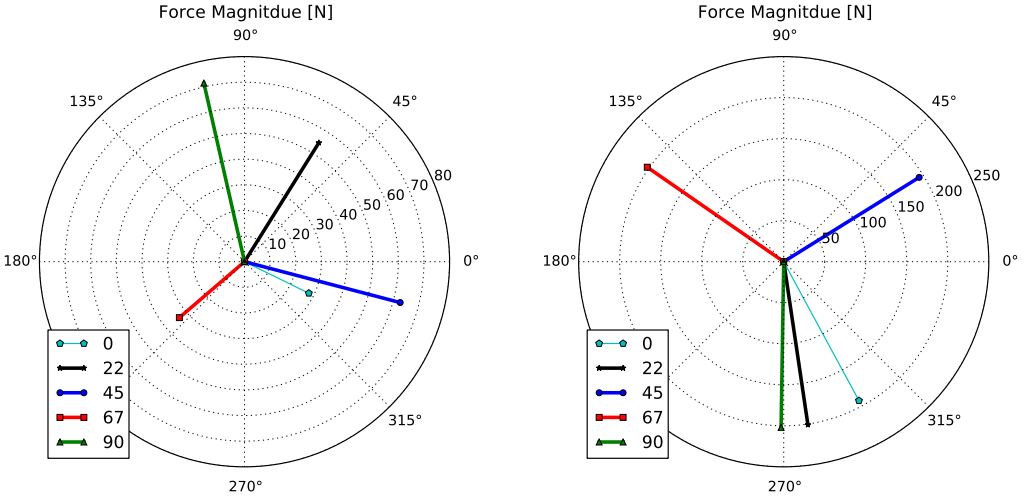

(a) (b)

Figure 4.9: Two views of the combined vectors as the HS rotor is rotated in steps of 22 degrees: (a) 23 modulating poles. (b) 25 modulating poles.

A discrete force integration was performed in B2 by applying the theory from section 4.1, and the transformation matrix 4.12. However, intermediate integrals were done on the lengths between each modulating pole piece and the result can be seen in Figure 4.10. In this figure the magnetic force's direction correlate well to the position of the HS magnet pole pairs, thus implying the force integration was done correctly.

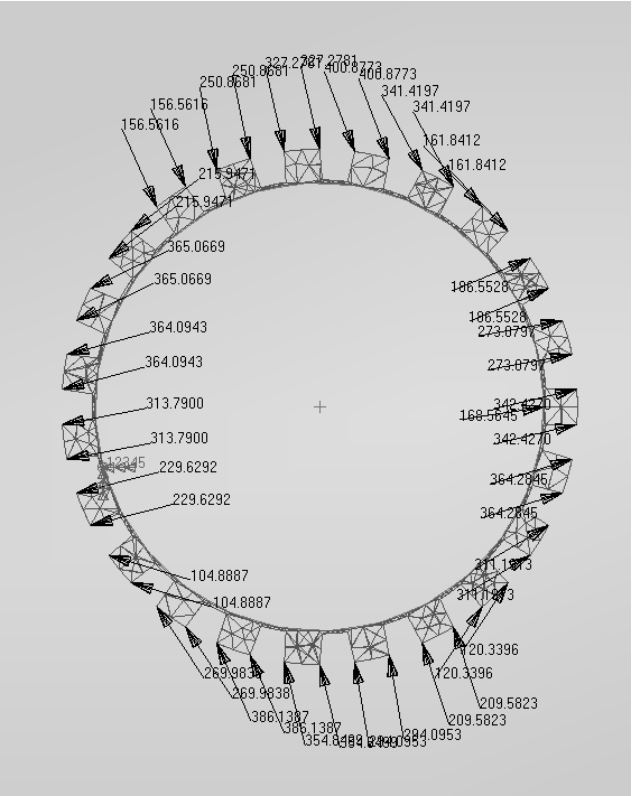

Figure 4.10: Discrete force representation for B2.

4.4 Unbalanced Magnetic Force Analysis

In this section the unbalanced magnetic forces for different gear ratios are investigated. The magnitude of these forces is also calculated as the gear rotates, as well as how increasing the gear size affects the force magnitude. Lastly, a summary of the findings is given.

4.4.1 Force & Gear Ratio Analysis

Tables E.1 and E.2, in Appendix E, show the data obtained for the unbalanced magnetic forces (UMF) at different gear ratios. For each case the following parameters are given: the operating frequency, LS and HS magnet pole pairs, modulating pole pieces, LS and HS gear ratios, the cogging factor for HS and LS, and UMF. The UMF's were taken as the highest value force for a 180° rotation of the HS shaft.

Three cases from Table E.1 are reiterated in Table 4.3, with an extra case which shows the UMF calculated for a gear ratio similar to the first prototype. Figure 4.11 shows the magnitude of the UMF on the y-axis, while the angular position of the HS shaft is given from 0° to 180° on the x-axis. Figure 4.11 clearly shows that case 1 exhibits the lowest UMF. From this study the importance of judicious selection of pole/slot combinations was realised, and

the following gear ratio selection criterion, in conjunction with Table E.1, was derived:

1. Class 1 design: low UMF, low torque ripple, and low operating frequency.
2. Class 2 design: low UMF, low torque ripple, and medium operating frequency.
3. Class 3 design: low UMF, lower torque ripple, and high operating frequency.

Thus, by applying the latter gear ratio selection criterion, a gear ratio of 11, at an operating frequency of 50 Hz, was chosen, where $p_{hs} = 2$, $p_{ls} = 20$, and $q = 22$.

Table 4.3: Gear ratio cases studied.

Case	freq	p_{hs}	p_{ls}	q	Gr	Grq	fch	fcl	UMF [N]
9	50	2	20	22	10	11	2	2	4
10	50	2	21	23	10,5	11,5	1	1	75
12	50	2	23	25	11,5	12,5	1	1	200
P1	100	4	11	15	2.75	3.75	1	1	395

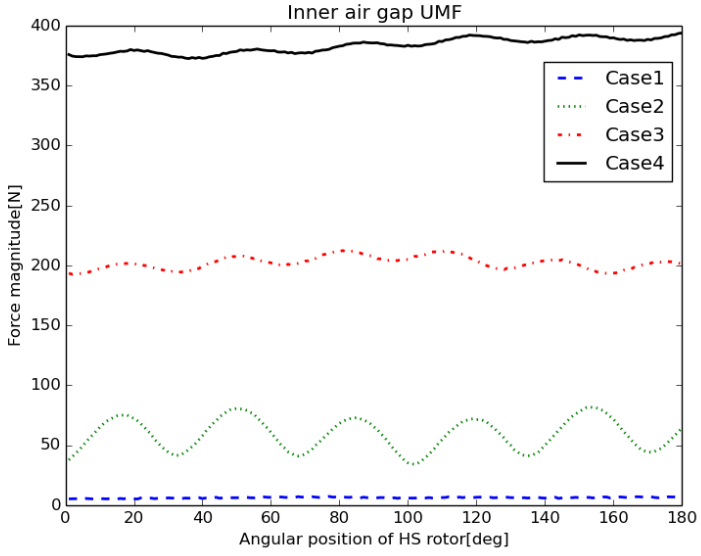

Figure 4.11: The force magnitude for the different cases as the HS shaft rotates.

4.4.2 UMF & Scaling

Further analysis was done to determine how the gear size affects the UMF. A scale factor was introduced to the gear parameters, gradually increasing the gear size from a scale of 1 to 2. Case 3 was used for this analysis, and the result can be seen in Figure 4.12. Thus the UMFs are linearly proportional to the gear size.

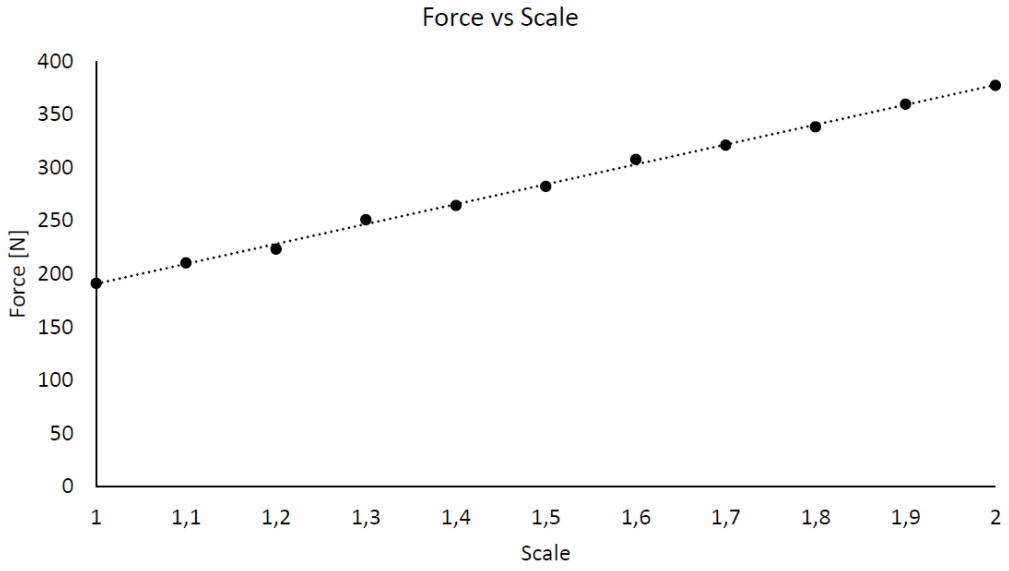

Figure 4.12: The force of case 3 as the gear size.

4.4.3 Summary of Findings

In this chapter the relationship between the magnetic forces and the three concentric components of an FMMG was discussed, more specifically the UMF and the number of magnetic pole pairs were investigated. Also, the effect of UMFs as the gear size increased were investigated. The findings are summarised as:

- Large UMF are present for certain gear ratios.
- First prototype had very large UMF.
- Importance of judicious selection of pole combinations to reduce UMF was discovered.
- General guideline for choosing gear ratios was derived and applied.
- UMFs increase with gear size.

Chapter 5

Prototype Design

In this chapter the design process of the prototype magnetic gear according to the specifications given in section 3.4 is described and consists of the following sections: electromagnetic design, mechanical design, strength analysis, and modal analysis.

5.1 Electromagnetic Design

The electromagnetic design is the starting phase of the MG design, which aims to determine the size and dimensions of the MG in order to satisfy the design specifications. To realise an optimum design, certain design objectives need to be formulated. In this section the design parameters and process are discussed. Then the MG volumetric torque density and torque ripple optimisations are discussed. Next, the final gear parameters are discussed, and lastly, the effect of yoke saturation is discussed.

5.1.1 Design Parameters and Process

Figure 5.1 shows the flow diagram for the optimisation, which was performed with the aid of VisualDoc software, and a SEMFEM simulation. The VisualDoc software starts by writing the initial input values to an input file, which is then read by the SEMFEM Python™ script. The simulation is executed, and an output file is sent back to VisualDoc. The constraints are then checked, followed by convergence. If either one of the conditions is not met new parameters are then determined by a selected algorithm. This cycle repeats until convergence is met within the required boundaries.

The MG parameters are all shown in Figure 5.2 and described in Table 5.1. The initial gear parameters were obtained by introducing a scaling factor to the parameters of the first prototype of Matthee (2016), as given in Table A.1.

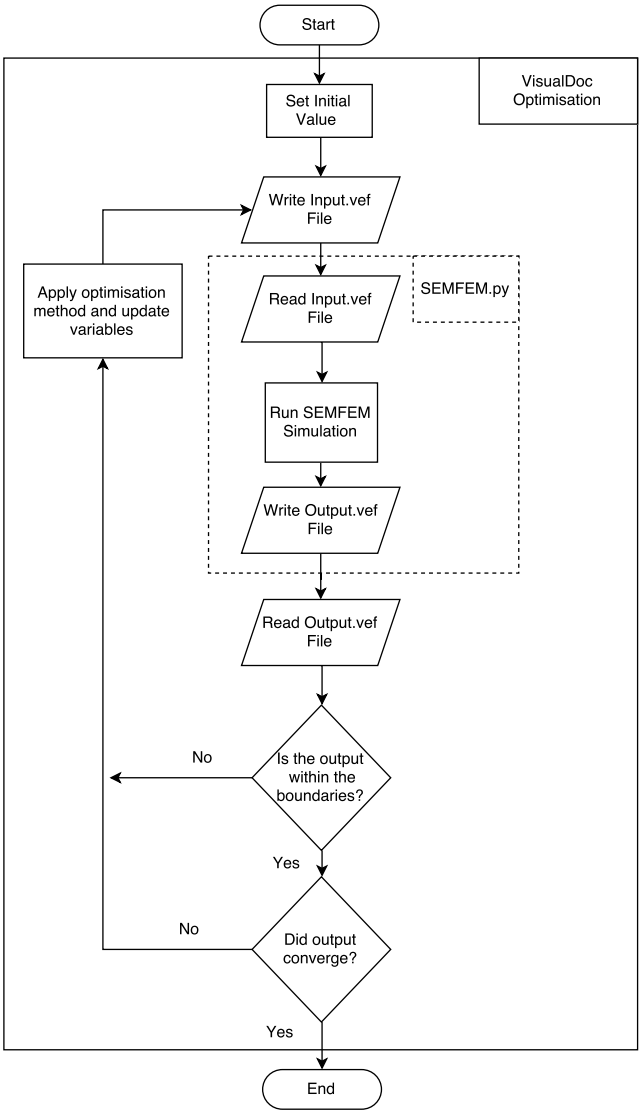

Figure 5.1: Flow diagram for the optimisation.

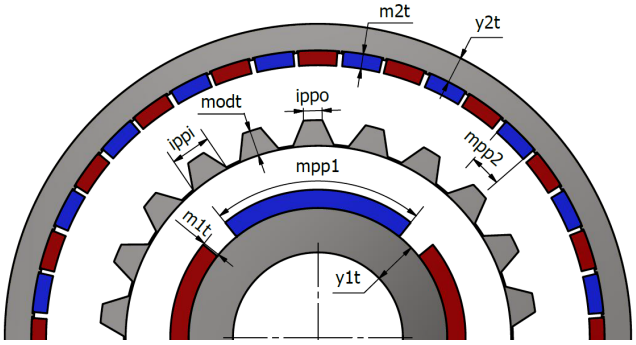

Figure 5.2: Design parameters of the MG, with exaggerated air gaps.

Table 5.1: Design parameters description.

Variable	Description
r_oy2	outer gear radius
y2t	outer yoke thickness
m2t	outer magnet thickness
modt	modulator thickness
m1t	inner magnet thickness
y1t	inner yoke thickness
sl	stack length
mpp2	outer magnet pole pitch
mpp1	inner magnet pole pitch
ippo	outer modulator pitch
ippi	inner modulator pitch

5.1.2 Torque per Volume

The objective function for the torque volume optimisation is given by equation 5.1, with the constraint of the torque given by equation 5.2, where τ_{out} is the stall torque, V is the volume of the gear, and $(x_0, x_1, ..., x_j)$ are all the parameters described in Table 5.1.

$$f(x_0, x_1, ..., x_j) = \text{MAX}\left(\frac{\tau_{out}}{V}\right) \tag{5.1}$$

Subject to:

$$\tau_{out} \geq 280\,\text{N·m}. \tag{5.2}$$

The design parameters with their initial values, upper and lower boundaries are given in Table 5.2. Generally, these boundaries are set to values which will not limit the optimisation process. However, they must be kept in a reasonable range which is still practical for manufacturing. As mentioned, the output torque and gear volume are calculated in SEMFEM. The volume of gear is calculated by summing the 2D areas of the gear and then multiplying them by the stack length to calculate the total volume of the gear.

Two algorithms were considered for the torque density optimisation, namely: Modified Method of Feasible Direction (MMFD) and Particle Swarm Optimisation (PSO). Furthermore, these optimisations were run multiple times with different initial values to ensure that the optimum point was not a local optimum point. The history plots for these two methods are given in Figures A.1a and A.1b, respectively. The MMFD was quick to execute but required to be reiterated a few times due to local minimums, while the PSO took longer to converge but did not suffer from local minimum values. The final design parameters for the MMFD and PSO are given in Table 5.2.

Table 5.2: Torque density intial values and boundary conditions.

Variable	Initial value	Lower boundary	Upper boundary	MMFD	PSO	Unit
r_oy2	110	100	120	110.5	106.0	mm
y2t	12	9	15	9	9	mm
m2t	8.5	5	10	7	5	mm
modt	11	7	15	8	10	mm
m1t	8.5	5	10	10	10	mm
y1t	31	24	40	24	24	mm
mpp2	0.85	0.7	0.95	0.80	0.76	-
mpp1	0.85	0.7	0.9	0.83	0.80	-
ippo	0.55	0.2	0.5	0.33	0.4	-
ippi	0.35	0.4	0.7	0.50	0.5	-

5.1.3 Torque Ripple

The torque ripple was reduced using methods similar to those described in section 5.1.2, but with a different objective function defined by equation 5.3, subjected to equation 5.4. This upper constraint was applied to avoid unnecessary simulations in the torque domain, where, the torque ripple, τ_{ripple}, is defined as the maximum torque, τ_{max}, and subtracted from the minimum torque, τ_{min}, as seen in equation 5.5.

$$f(x_0, x_1, ..., x_j) = \frac{\tau_{out}}{\text{minimise}(\tau_{ripple})} \tag{5.3}$$

$$280\,\text{N·m} \leq \tau_{out} < 290\,\text{N·m} \tag{5.4}$$

$$\tau_{ripple} = \tau_{max} - \tau_{min} \tag{5.5}$$

The optimisation was computationally expensive, since various simulation steps were required to detect the torque ripple, and was therefore done separately from the torque density optimisation. Furthermore, a one-at-a-time (OAT) sensitivity analysis was performed on the MG parameters to determine which parameters affect the torque ripple significantly and to eliminate the parameters which had a negligible effect on the torque ripple. The parameters found to be predominate are presented in Table 5.3, with their initial conditions, upper boundaries and lower boundaries. It was found that the parameters related to the thickness of the gear did not affect the shape of the output torque ripple as much as the pitch parameters.

Table 5.3: Torque ripple intial values and boundary conditions.

Variable	Initial value	Lower boundary	Upper boundary	Optimised point
mpp2	0.8	0.7	0.9	0.878
mpp1	0.8	0.7	0.9	0.865
ippo	0.275	0.35	0.4	0.30
ippi	0.55	0.15	0.75	0.73

The particle swarm algorithm was used since it proved to be more reliable in terms of avoiding the local minimum. The 2D unoptimised gear is shown in Figure 5.3a and the optimised gear simulation model is shown in Figure 5.3b. Figure 5.4 shows the simulated initial and optimised torque ripple. The output torque of the HS shaft is given on the y-axis and the angular position is given on the x-axis.

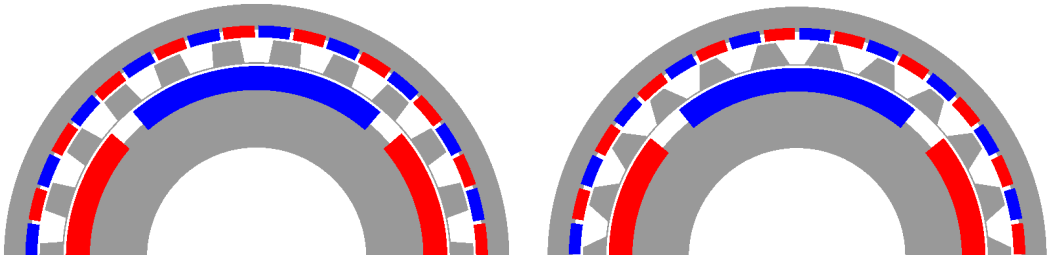

(a) (b)

Figure 5.3: Torque ripple simulation models: (a) Initial model. (b) Optimised model.

5.1.4 Discussion of Final Parameters

The thickness of the gear parameter was taken from the PSO torque volume optimisation and the pitch parameters from the torque ripple optimisation. Another OAT sensitivity analysis was performed on the torque ripple parameters to determine the robustness of the design point, (see Appendix A.5). It was found that the most sensitive parameter was mpp1 and further analysis on mpp1 showed that the output torque went through a phase change between a pole pitch of 0.86 and 0.87. Thus the design point was aimed at the optimum value of 0.865. As a result, precise machining was crucial to obtaining the design point, and the final gear parameters are given in Table A.3. Furthermore, to reduce the magnet losses discussed in section 3.2, the HS magnets were segmented into three smaller magnets.

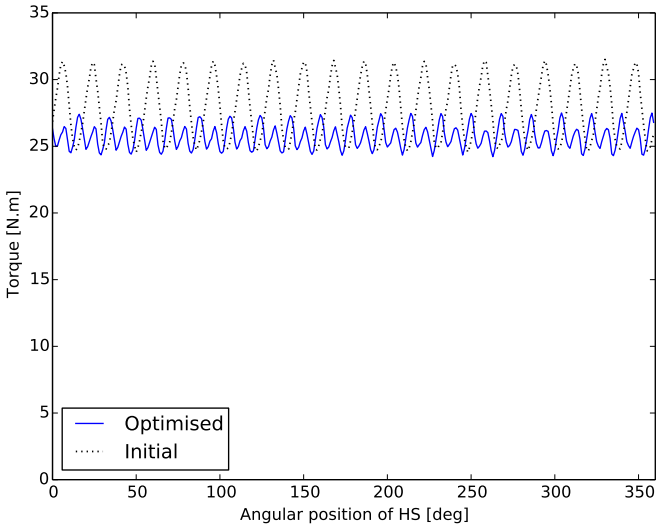

Figure 5.4: Output torque versus angular position of the HS shaft.

5.1.5 The Effect of Yoke Saturation

During the no-load evaluation of the prototype excessive losses were measured, and an investigation was done to determine the source of these losses. It was found that the outer yoke of the gear was saturated causing flux leakage into the aluminium housing, and in effect eddy current generation. The root of the problem was in the air boundary condition in the SEMFEM simulation which restricted the flux flow. This was confirmed by a 2D FEM simulation and the simulation models can be seen in Figure 5.5, while the results are shown in Figure 5.6. From Figure 5.6 a significant electrical losses can be seen.

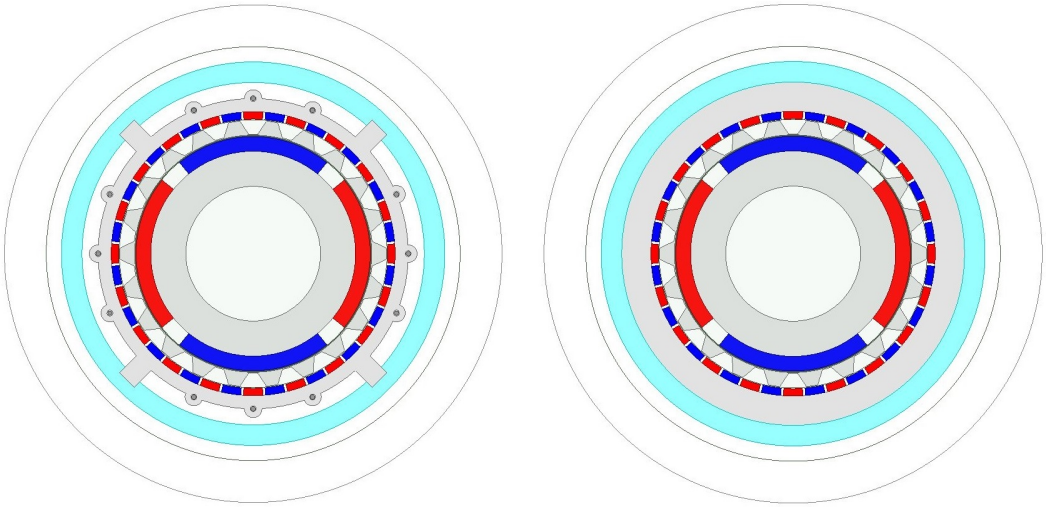

(a) (b)

Figure 5.5: Losses simulation models: (a) Initial yoke. (b) Improved yoke.

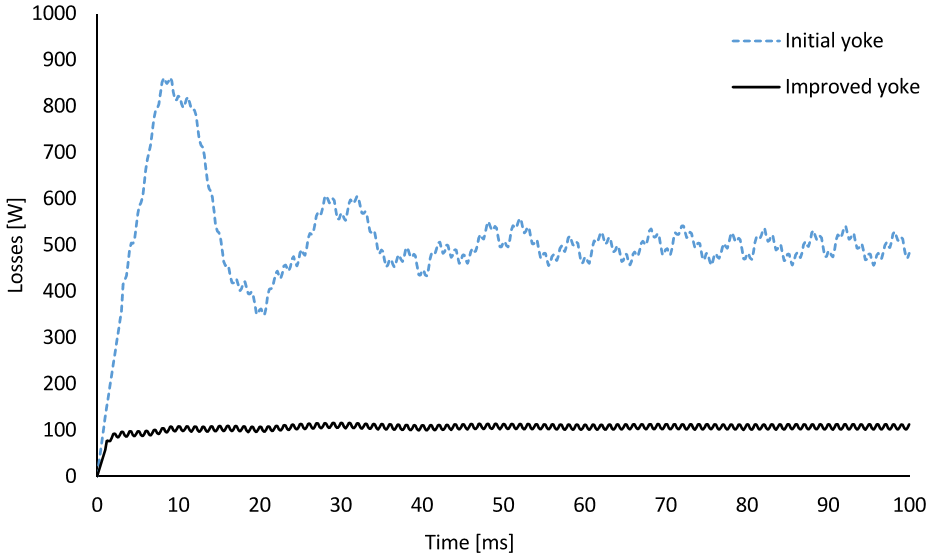

Figure 5.6: Losses of the initial yoke and improved yoke, at a rated speed of 1500 rpm.

Two solutions were attained and applied to the final magnetic gear. The first improvement was adding extra yoke material between the LS yoke and the housing of the initial design, as seen in Figure 5.7b.

The second improvement was to replace the aluminium housing with an acetal housing, in combination with the extra yoke, as seen in Figure 5.7c. As a result, three MG gear designs are presented in this research, namely: the initial design (see Figure 5.7a), the improved design (see Figure 5.7b), and the final design (see Figure 5.7c). These improvements were not difficult to implement since the mechanical design was modular, as discussed in section 5.2.

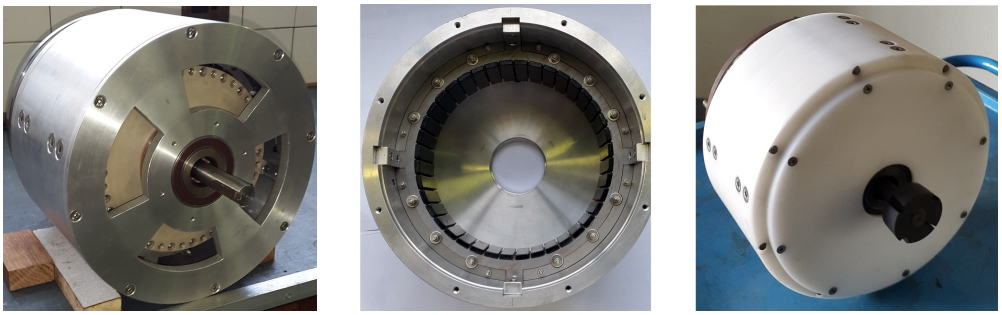

(a) (b) (c)

Figure 5.7: Three designs: (a) Initial design. (b) Improved design. (c) Final design.

5.2 Mechanical Design

The mechanical design layout of prototype two will be discussed in this section, followed by the various mechanical design features which make the final product easy to assemble and allow the design to be reused in future studies.

5.2.1 Main Assembly

The design model and drawings of the MG were done in the commercial software package Autodesk® Inventor Professional 2016. The optimisation and design drawings were done in parallel, and the parameters had to be frequently updated. As a result, the model was defined with each parameter linked to an Excel™ file which allowed the parameters to be updated easily. The final design and drawings of the gear were separated into 4 assemblies: namely the housing assembly, low-speed (LS) assembly, modulator assembly, and high-speed (HS) assembly. Figure 5.8 shows an exploded view of the assemblies for the final design. Not all fasteners are shown in the figure and the construction of the final assembly can be seen in Figure F.1 and was done as follows:

1. The HS shaft was aligned with the modulator and inserted with a lathe.
2. Side plate 2 was fixed with corresponding fasteners.
3. The modulator was aligned with the housing and inserted with a lathe.
4. Housing lid 1 and 2 were fastened.

5.2.2 Housing and LS Assembly

The housing and LS assembly are discussed together and an exploded view can be seen in Figure 5.9. The materials and fasteners of each component can be found in Table 5.4. The constructed assembly can be seen in Figure F.2 and was assembled as follows:

1. Stacking the outer yoke of the housing body.
2. Fixing the positioning blocks with corresponding bolts.
3. Applying the epoxy to the lamination stack.
4. Fixing the magnets with the aid of a designed tool.

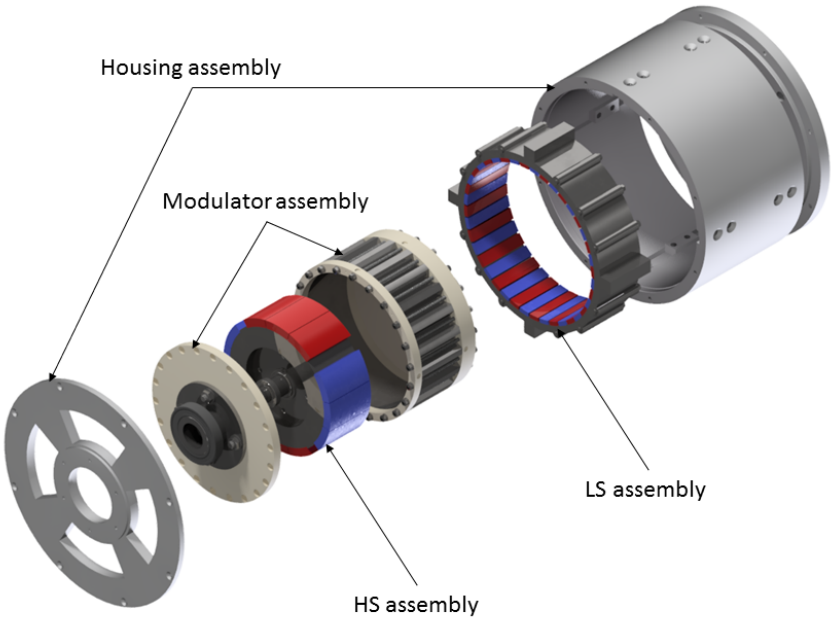

Figure 5.8: Exploded view of the magnetic gear showing the assemblies.

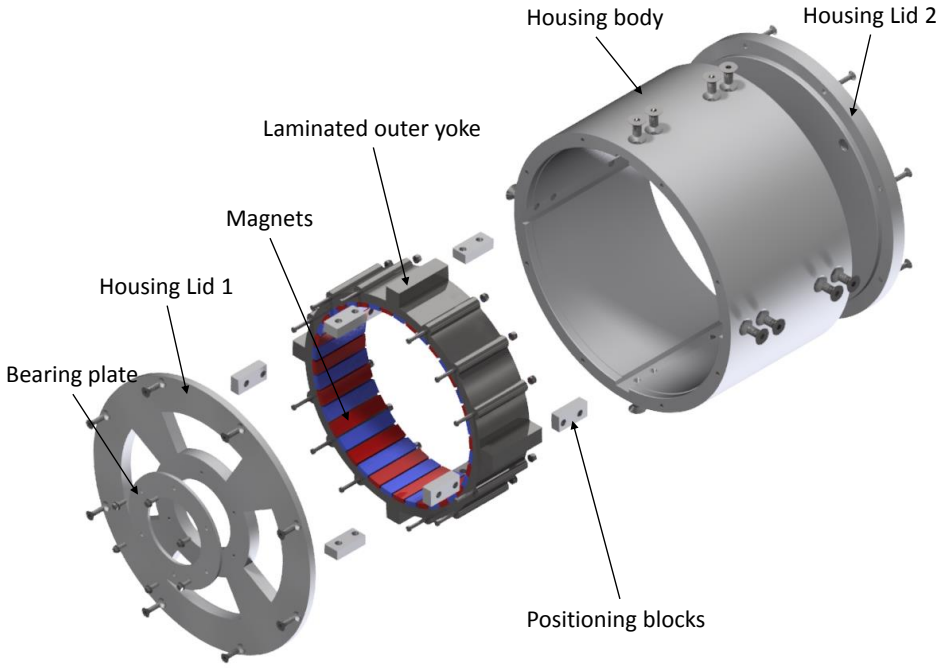

Figure 5.9: Exploded view of the housing and low speed magnets.

5.2.3 Modulator Assembly

An exploded view of modulator assembly is presented in Figure 5.10 and the materials and fasteners of each component can be found in Table 5.4. The constructed assembly can be seen in Figure F.3 and was assembled as follows:

1. Stacking the modulator laminations over a mould.
2. Compressing the laminations with side plate 1 and compressive ring.
3. Casting the epoxy into the lamination stack.
4. Baking epoxy at 40 °C for 16 hours.
5. Machining to outer dimensions.
6. Removing mould and machining to final dimensions.

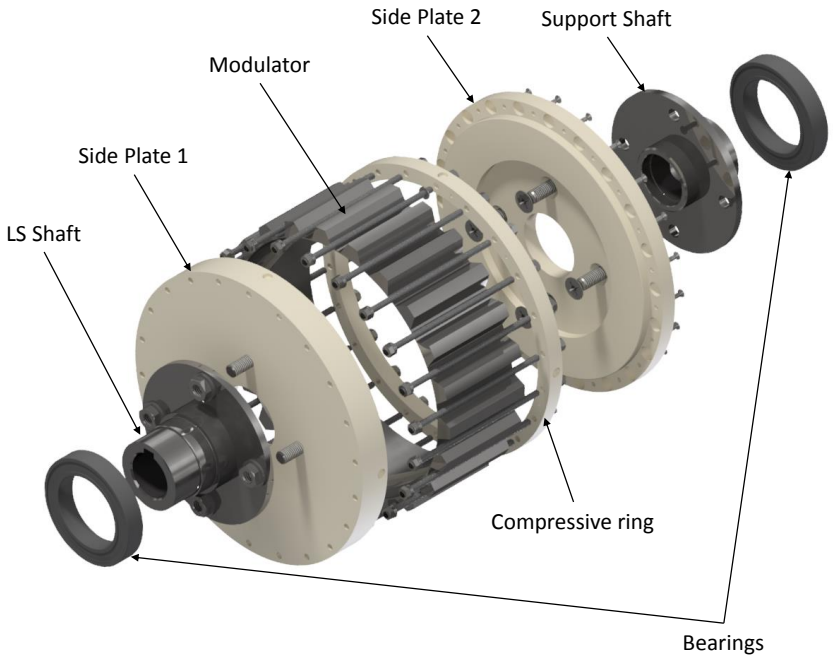

Figure 5.10: Exploded view of the modulator.

5.2.4 HS Assembly

An exploded view of the HS assembly is presented in Figure 5.11 and the materials and fasteners of each component can be found in Table 5.4. The constructed assembly can be seen in Figure F.4 and it was assembled as follows:

1. Fixing the magnets to the yokes with epoxy.

2. Aligning and assembling the two HS yokes in a milling machine.
3. Applying the appropriate fasteners.

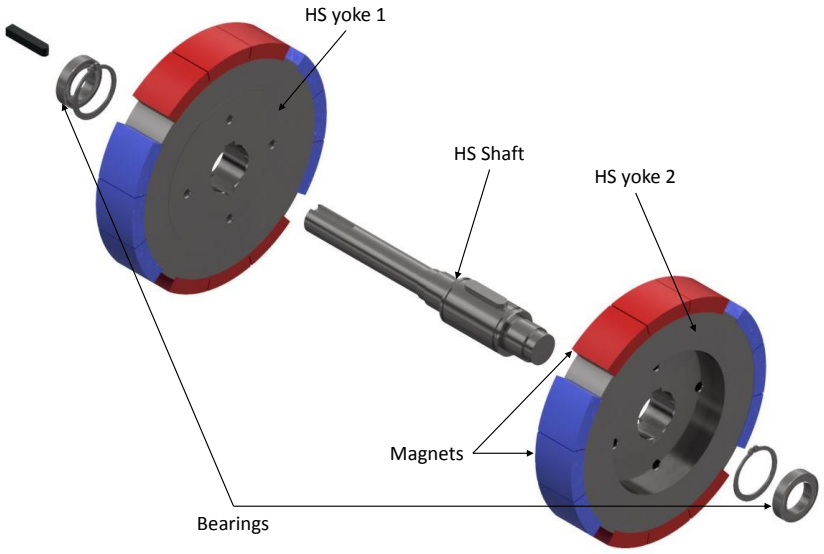

Figure 5.11: Exploded view of the high speed assembly.

5.2.5 Material Selection

The materials and fasteners used for the assemblies are given in Table 5.4. As mentioned in section 3.2, areas experiencing high magnetic flux density require non-magnetic and low electrical conductive materials to avoid electromagnetic losses. As a result, various materials were considered during the design, since using magnetic materials such as steel can cause flux to be misguided and can cause losses.

For the housing, aluminium 6081 was chosen because of its non-magnetic characteristics, strength, and good machinability. Stainless steel 316 was also considered, however, it was more expensive.

The material for the modulator was of special concern since it was located close to the active magnets. The first material considered for the modulator side plates was ceramic, however, it is very expensive to manufacture and break easily under tensile stress, and was disregarded. The second material considered was carbon fibre, this was also expensive to manufacture and there is a risk of inducing eddy currents in the carbon fibres, and it was therefore avoided. The third material considered were thermoplastics more specifically: TUFNOL®, (see (TUFNOL, 2017)), and Ketron® PEEK, (see (Quadrant, 2017)).

Material fillers can be added to PEEK to increase its stiffness and material properties. The fillers considered are the glass filler and carbon filler. The glass fibre reinforced PEEK is very expensive and tends to damage cutting machinery, while carbon fibre reinforced PEEK has a risk of inducing eddy currents in the carbon fibres. As a result, the unfilled PEEK was chosen due to its high strength and very low moisture absorption.

For the HS yokes and shafts, EN 8 mild steel was used because of its strength, cheapness, and good machinability. For the fasteners, stainless steel 316 was used because of its low magnetic and electrical conductivity.

Table 5.4: Materials and fasteners for the assemblies.

Description	Material	Fasteners
	Housing and LS assembly	
Bearing Plate	Aluminium 6081	6 x M4, S/Steel bolts
Housing lid 1	Aluminium 6081	8 x M5, S/Steel bolts
Housing lid 2	Aluminium 6081	8 x M5, S/Steel bolts
Housing Body	Aluminium 6081	-
Positioning blocks	Aluminium 6081	16 x M8, S/Steel bolts
Magnets	NdFeB 48H	Araldite® AV138 & HV998
Outer yoke	Electrical steel M400-50A	22 x M4, S/Steel bolts
	Modulator assembly	
Bearings	Mild Steel Sealed	45 x 68 x 12
Compressive ring	Ketron® PEEK	22 x M4, S/Steel bolts
LS Shaft	Mild Steel EN8	4 x M8, S/Steel bolts
LS Shaft	Mild Steel EN8	4 x M8, S/Steel bolts
Modulator	Electrical steel M400-50A	22 x M4, S/Steel bolts & Ampreg 21 (Epoxy)
Side Plate 1	Ketron® PEEK	22 x M4 S/Steel bolts
Side Plate 2	Ketron® PEEK	22 x M3 S/Steel screws
	HS assembly	
Bearings	S/Steel Sealed	20 x 32 x 7
HS Shaft	Mild Steel EN8	2 x M6 S/Steel bolts
HS Yoke 1	Mild Steel EN8	Circlip, 2 x M6 S/S bolts
HS Yoke 2	Mild Steel EN8	Circlip, 2 x M6 S/S bolts
Magnets	NdFeB 48H	Araldite® AV138 & HV998

5.2.6 Motor-Gear Interface

The motor-gear interface was one of the specifications given in section 3.4. Mechanical gears mounted to motors are generally used with an down-speed configuration. However, due to the layout of the test-setup, the MG was designed with a up-speed configuration. An ISO quarter sectioned view is presented in Figure 5.12a, and a sectioned side view in Figure 5.12b. From these figures it can be seen that the MG mounts onto the motor flange, and the motor slides into the MG.

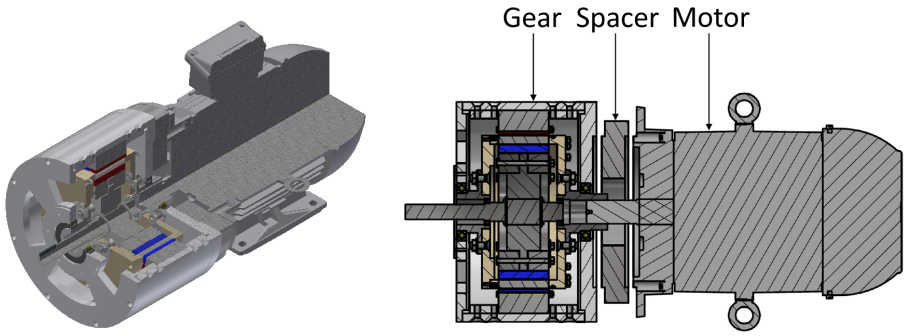

(a) (b)

Figure 5.12: Motor-gear interface: (a) ISO sectioned view. (b) exploded side view.

5.2.7 Assembling & Maintenance Improvements

Another research objective and specification from section 3.4 was to improve the construction, assembly, and maintenance of the MG and will be discussed here.

A magnetic grip was designed to aid in the placing of the magnets, and the usage of the tool is presented in Figure 5.13. Firstly, the magnet is fastened in the magnetic grip by the clamping screw (Figure 5.13a). Secondly, the tool is used to place the magnet in the appropriate slot (Figure 5.13b). Thirdly, the grip is detached from the magnet (Figure 5.13c). This processes was repeated for all magnets and proved to reduce the effort and construction time of the gear. Also, no epoxy was removed during the fixing of the magnets and no magnets were damaged, while for the first prototype two magnets were damaged and the magnet placement proved to be problematic.

With further design refinement the tool can be automated, thus increasing the productivity of construction and reducing the risk of damage to the magnets and employees.

Figures 5.14a and 5.14a show the front and sectioned side view of a proposed way of performing maintenance on the MG. Bolts are used to support the modulator allowing the LS bearings to be replaced, and the HS assembly

to be removed with its bearings. During the implementation of the improvements, the gear was assembled and disassembled with ease. This demonstrated how maintenance of the second prototype can now be done with ease.

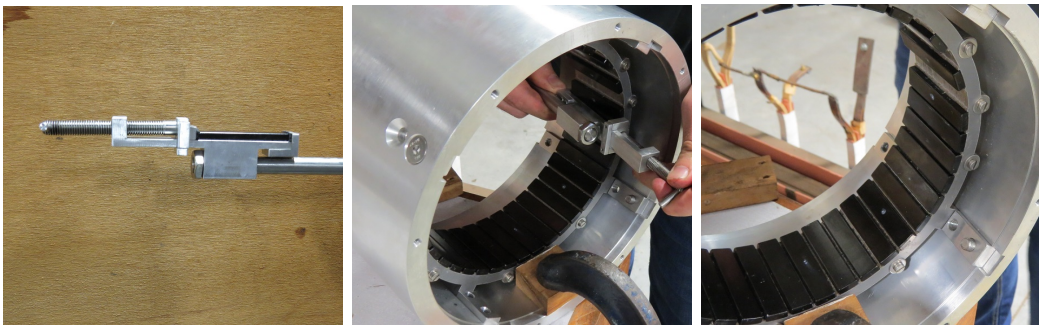

(a) (b) (c)

Figure 5.13: Four views of using magnetic grip: (a) Fasten magnet in grip. (b) Place magnet with grip. (c) Detach magnet from grip.

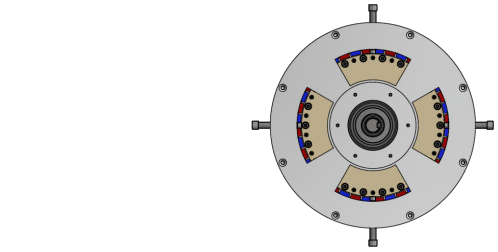

(a)

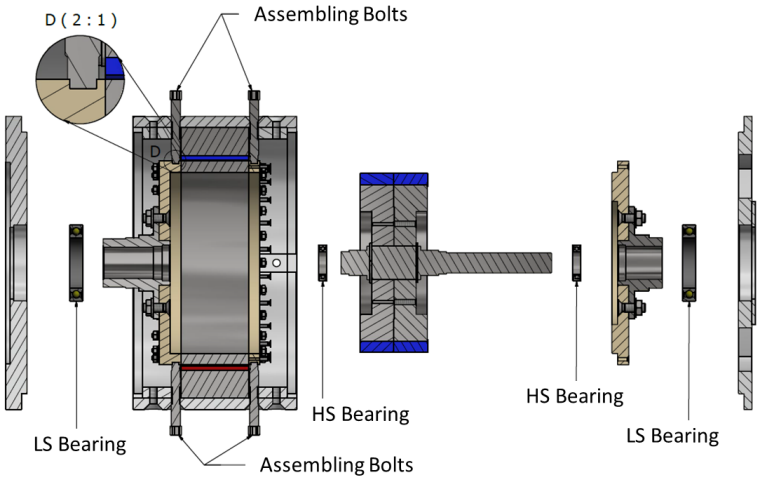

(b)

Figure 5.14: Maintenace demonstration: (a) Front view. (b) Sectioned side view.

5.2.8 Modular Design

The design was made modular to ensure components can be easily replaced, and the components were kept symmetrical as far possible. Thus, reducing the manufacturing time and in effect cost. Furthermore, this allows the design to be reused in future research projects.

Another phase of the product considered was the product end-of-life of the prototype. This process will be done as recommended in Dieter and Schmidt (2013), and is performed as follows:

1. Reuse all materials possible.
2. Remanufacture parts that can be used again.
3. Recycle all materials that can be recycled.
4. Dispose of rare earth materials in an appropriate manner.

5.3 Strength Analysis

To realise a reliable MG design the mechanical strength and durability of the components are investigated as described in this section. This is done by applying the analysis method described in Budynas and Nisbett (2011). First, the shafts are analysed, followed by the bearings, and finally the modulator bolts. All calculations are done with the assumption of pure shear stress. The procedure followed for this is listed below as:

1. Identify components that will endure the highest stress.
2. Calculate the position and magnitude of the maximum stresses.
3. Calculate safety factors against failure.

5.3.1 HS and LS Shaft Calculations

According to FEM specifications, (see section 3.4), the rated torque on the HS and LS shafts are 14 N·m and 154 N·m, respectively. A service of 1.5 was accepted resulting in a torque of 21 N·m and 231 N·m, respectively. Furthermore, the shafts were designed to withstand higher torques than the maximum torque of the gear and 23 N·m and 255 N·m was used as the maximum torque applied to the shafts, respectively. For both LS and HS shafts the highest stress occurs at the key-way. The safety factor n_z at the key-way was obtained by using the modified-Goodman equation, given as:

$$n_z = \frac{1}{\frac{\sigma'_{az}}{S_{ez}} + \frac{\sigma'_{mz}}{S_{ut}}} \tag{5.6}$$

where, S_{ut} is the ultimate tensile stress, S_{ez} is the endurance limit, σ'_{az} is the amplitude stress, and σ'_{mz} is the median stress. The safety factor for the HS shaft was found to be 2.42 and for the LS shaft 2.80. These calculations can be found in Appendix B. These safety factors are satisfactory since the modified-Goodman is considered a conservative method of calculating the fatigue safety factor compared to other methods (Budynas and Nisbett, 2011).

5.3.2 Bearing Calculations

Suitable bearings were chosen from SKF (2017) catalogues according to the required dimensions. Bearings calculations were done to ensure that they are suitable for the application, and these calculations for the HS and LS assemblies can be found in Appendix B. For the bearing loads the simulation force obtained in Chapter 4 was used along with the weight of the assembly.

5.3.3 Modulator Calculations

As seen from Figure 5.10 the modulator pole pieces are compressed with 22 bolts, and the LS shaft is connected to the side plate with 4 bolts. The integrity of these bolts was calculated and can be found in Appendix B.

5.4 Modal Analysis

This section will investigate the vibration characteristics of the prototype by performing an FE modal analysis. From the analysis, it was found that modes 1 and 2 were the transverse displacement and torsional displacement, respectively. Also, modes 3, 4, and 5 were similar to each other with mode 5 being the most severe mode. Modes 6 and 7 showed similar displacement but in opposite directions. Figure 5.15 shows the displacement of modes 1, 5, and 7, with their corresponding resonant frequencies.

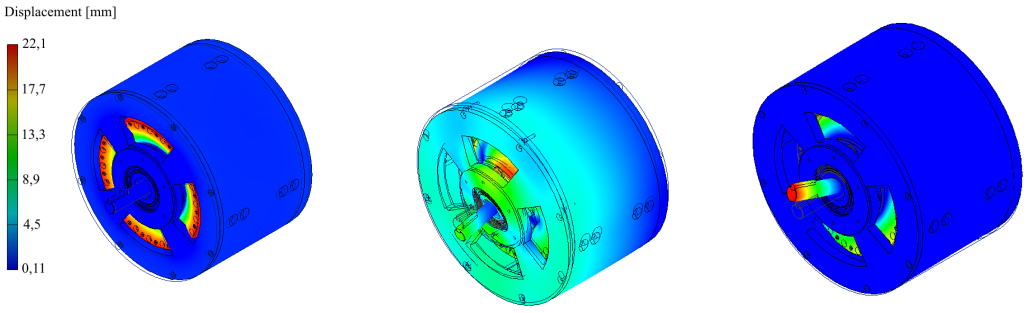

(a) (b) (c)

Figure 5.15: Full gear modal analysis: (a) Mode 1 at 485 Hz. (b) Mode 4 at 789 Hz. (c) Mode 7 at 893 Hz.

Chapter 6

Prototype Evaluation

A performance evaluation of the magnetic gear prototype is presented in this chapter. Figure 6.1a gives a schematic of the test-setup configuration, and Figure 6.1b shows the actual test-setup. The equipment used during the evaluation is listed here, and the calibration of the equipment can be found in Appendix D:

1. Delta AC servo motor - ECMA series.
2. AC servo drive - ASDA A2 series.
3. Two torque sensors - Lorenz DR 3000.
4. Piezoelectric accelerometer - Brüel Kjær type 4381.
5. Charge Amplifier - Brüel Kjær type 2635.
6. Data acquisition - LMS SCADAS SCM01.
7. Two laptop - Lenovo L530 and Dell Inspiron 3542
8. Motor Coupling, Appendix C.
9. Magnetic gear, Figure 5.7.
10. Fan with 6 polymer blades.

6.1 No-load Tests

The no-load losses of the prototype were measured by removing all connections to the output shaft, i.e. the torque sensor and fan load, and as the name implies no load was transferred, and thus the internal losses of the gear were evaluated. Figure 6.2 shows the no-load loss evaluation of the three design cases versus the output speed. As mentioned, these designs are labelled as: the initial design, the improved design, and the final design.

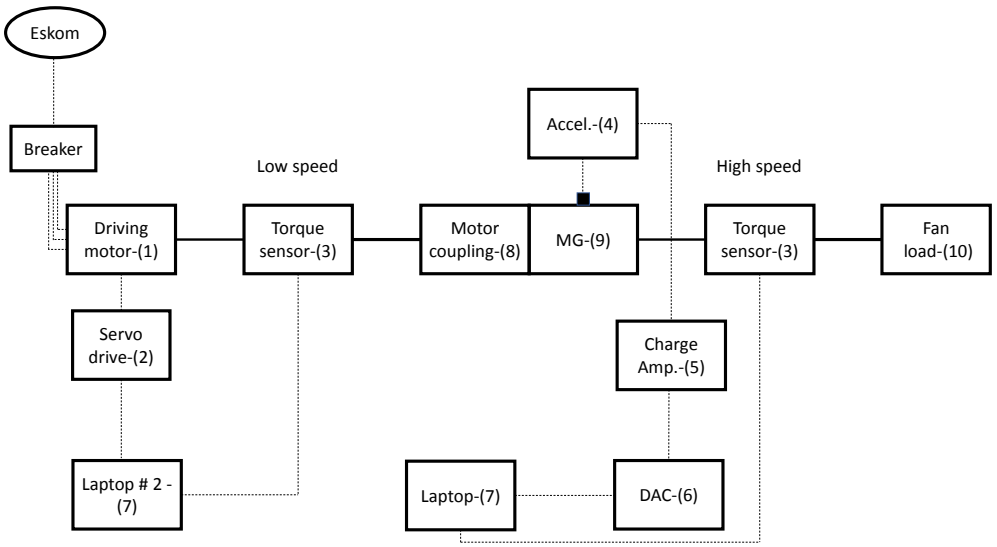

(a)

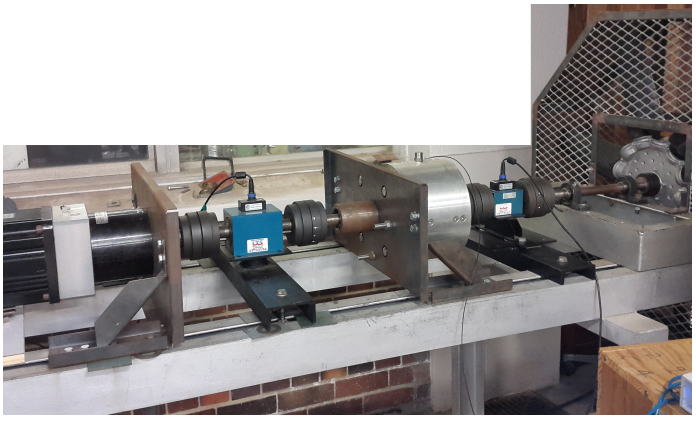

(b)

Figure 6.1: Test set-up: (a) Schematic. (b) Actual set-up.

From Figure 6.2 it can be seen that the power loss for the MG is proportional to the speed and was the highest at the rated speed of 1500 rpm, in all three designs.

The initial design suffered from very high no-load losses with a peak value of 720 W. The improved design shows a great reduction in losses with a peak value of 290 W, and the final design shows the lowest losses with a peak value of 180 W. The cause of these losses was discussed in Chapter 5. The no-load losses are listed in Table 6.1 and by comparing the final design to the first prototype an improvement of 10 W can be noted.

However, from section 3.2 the electromagnetic losses of an MG are proportional to the operating frequency, and the first prototype operated at a frequency 10 Hz lower than the final design. Thus, if the final design operated at a frequency of 40 Hz (1200 rpm), its no-load losses can be obtained as 120 W.

This implies that at a similar operating frequency, the second prototype improved by 70 W, or a 36.8 % no-load loss decrease, which is substantial.

Table 6.1: No-load losses.

Design	Losses [W]	Frequency [Hz]
Initial	720	50
Improved	290	50
Final	180	50
First prototype	190	40
Final (lower freq.)	120	40

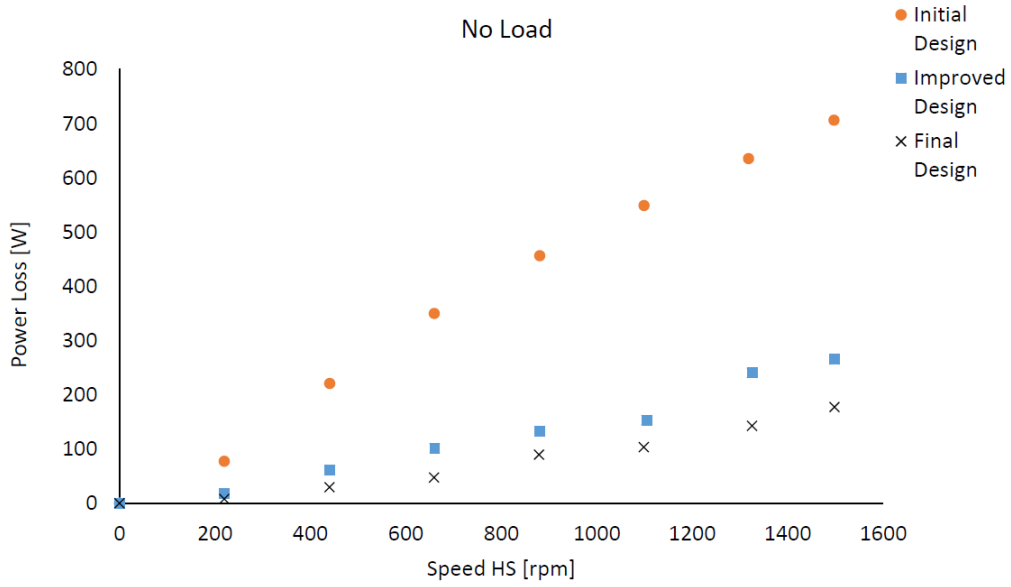

Figure 6.2: No-load loss curves for the initial design, the improved design, and the final design.

6.2 Load Tests

The fan load results for the improved and final designs are presented in this section. The initial design was not tested with the fan load to prevent damage to the magnets from the heat loss generated.

Two fan curves were obtained for fan pitch angles: 25° and 30°. The fan curves for the improved design and the final design can be seen in Figure 6.3 and Figure 6.4, respectively. Ideally the output power should approximate the input power. Then, by comparing the improved design with the final design,

it can be clearly seen that the input and output curves for the final design are closer to each other. Thus, implying that a higher efficiency and stable power transfer was achieved by the improved design.

Furthermore, these figures show that the power slightly increased for the final design fan curves. This was due to the fact that the exact fan pitch angles: 25° and 30° were within a human error of ± 1°. The torque sensors were accurate to ± 0.1 N·m and the error from this is negligible.

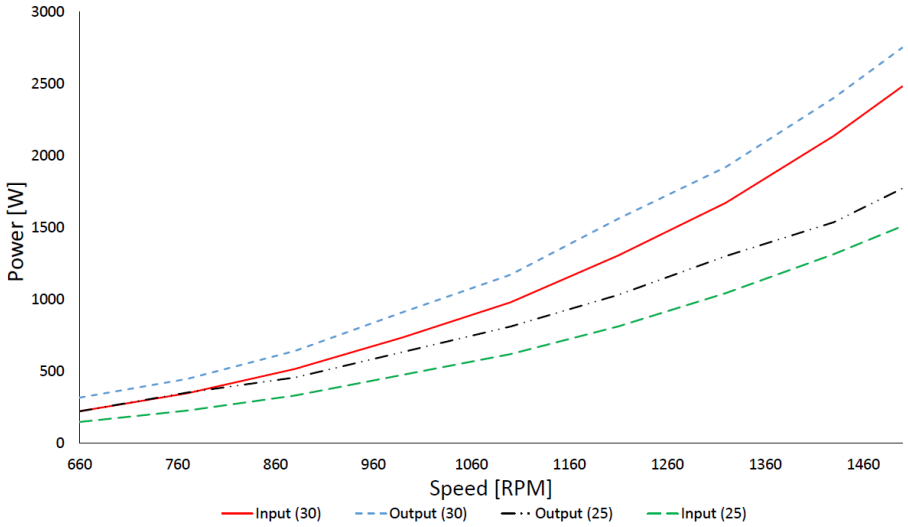

Figure 6.3: Fan curves for improved design.

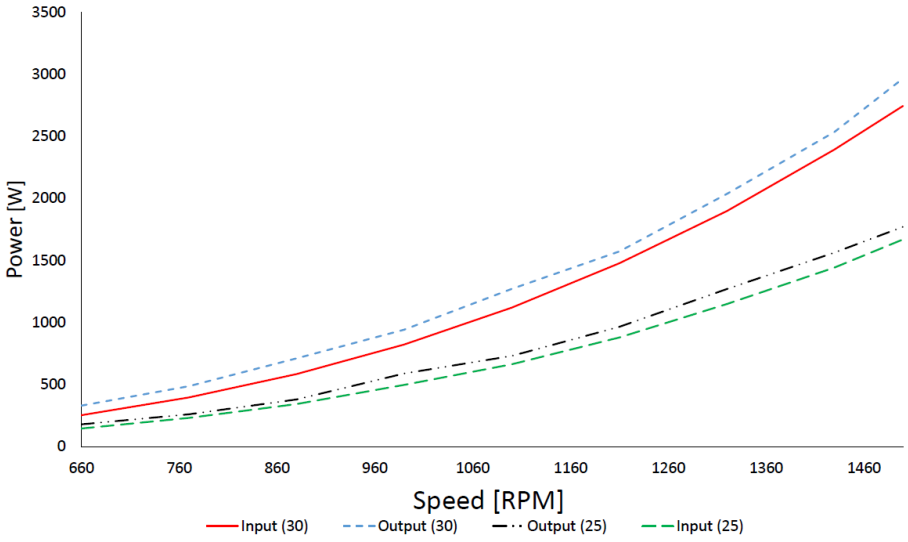

Figure 6.4: Fan curves for final design.

From the fan curve data, the efficiency maps were obtained for the improved and final designs by implementing equation 6.1, and the results are presented in Figures 6.5a and 6.5b, respectively.

$$\eta = \frac{P_{out}}{P_{in}} \tag{6.1}$$

For both designs, it can be seen that there is an increase in efficiency with increasing speed and torque until the rated condition is reached. Furthermore, the highest efficiency achieved for the improved and final design was 90 % and 95 %, respectively, an improvement of 5 %. However, by comparing the full efficiency distribution a significant increase in efficiency can be observed throughout the operating domain of the final design. This indicates that the range of the rated operating conditions expanded.

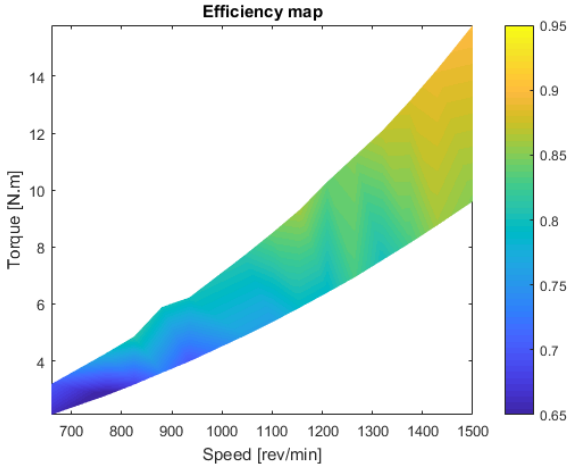

(a)

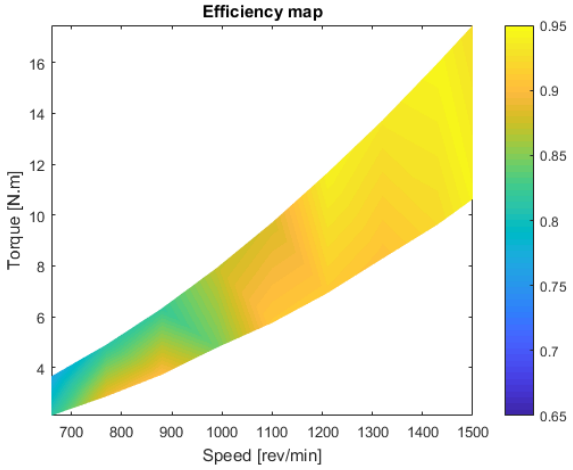

(b)

Figure 6.5: Efficieny map for: (a) Improved design. (b) Final design.

6.3 Vibration Tests

The vibrational analysis for the second prototype was done on the improved design with a fan load. The PSD at rated speed is given in Figure 6.6, and gives the amplitude of the frequencies in m^2/s^3. The labels in Figure 6.6 correspond to the measured values given in Table 6.2, while the calculated values were obtained as discussed in section 2.4.1. Thus, measured values compare well to the calculated values, where the dominant frequency (1), relates to the operating speed of the output shaft, while the excited frequency of the MG (2), and (3) is the HS bearing frequency. Furthermore, peak (4) is the frequency of the drive and peak (5) is the vane passing frequency of the fan. Thus, the excited frequency of the MG (2), relating to the transmission forces, was three times lower than the speed frequency (1). Thus, the UMF and vibrations in the second prototype were greatly reduced and the MG was stable during operation.

Spectrograms for the speed ramp up, rated output speed, and ramp down are shown in Figures G.2a, G.2b, and G.2c, respectively. The spectrograms clearly show the excited frequencies presented in Table 6.2. Since the excited frequencies of the MG exist in the low-frequency domain, the modes presented in section 5.4 were not excited during operation.

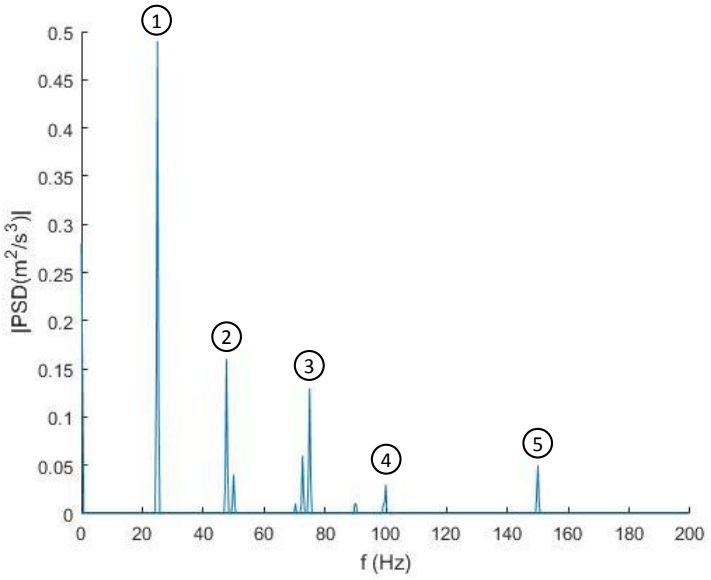

Figure 6.6: PSD of the operating speed.

Table 6.2: Frequencies at rated conditions.

Label	Description	Calculated [Hz]	Measured [Hz]
1	Output speed	25	25
2	MG pole	50	48
3	HS bearing	82	75
4	Servo drive frequency	100	100
5	Fan vain frequency	150	150

6.4 Stall Torque Tests

The stall torque of an MG is the maximum torque of the gear before slipping, and it will be evaluated in this section. This was done by fixing the HS output and then loading the LS input by a moment arm until the gear slipped, as seen in Figure G.1. The stall torque for the improved and final designs was the same since only the housing was replaced.

The simulated stall torque for the initial and improved/final designs are given in Figure 6.7, while Figure 6.8 shows the measured stall torque for the initial and improved/final designs. The results are summarised in Table 6.3, and, as discussed in section 3.1.2, the 2D simulations for the initial design show a 21.4 % difference to the measured torque, while the improved/final design show a 18.2 % difference. The 3D simulations for the initial design show a 0.9 % difference, while the improved/final designs show a 2.9 % difference. Thus, the measured values compare well to the simulated values. Human error can be the cause of the small discrepancy in these values.

Also, the stall torque increased by 40 N·m for the improved/final design.

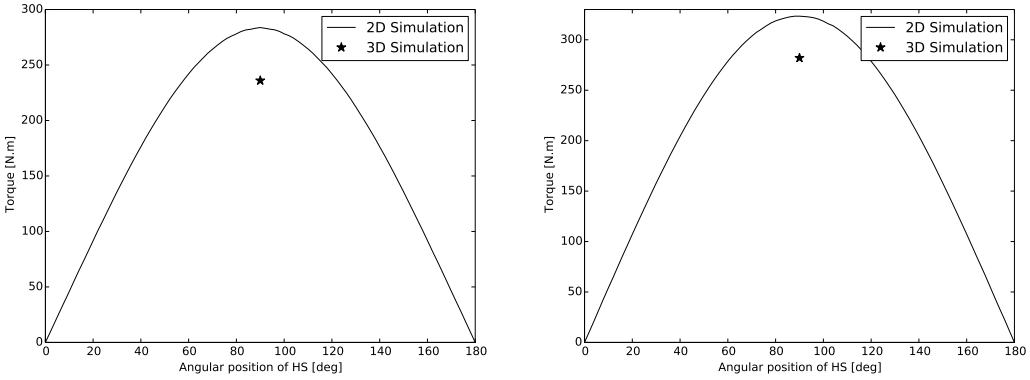

(a) (b)

Figure 6.7: The simulated stall torque for: (a) Initial design. (b) Improved/Final design.

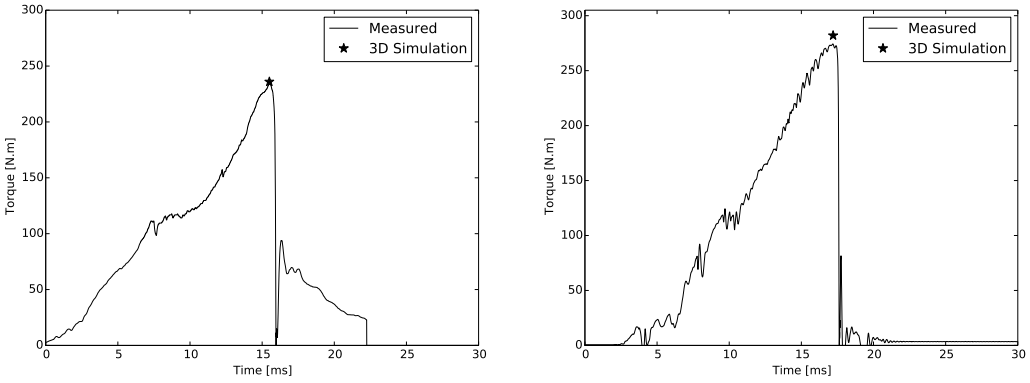

(a) (b)

Figure 6.8: The measured stall torque for: (a) Initial design. (b) Improved/Final design.

Table 6.3: Stall torque comparison.

	Initial design	Improved/Final design
2D [N·m]	284	324
3D [N·m]	236	282
Measured [N·m]	234	274
2D Difference [%]	21.4	18.2
3D Difference [%]	0.9	2.9

6.5 Torque Ripple

Torque ripple percentage is defined in section 3.1.3 and reiterated by equation 6.2. The measured torque ripple for a fan pitch angle of 25° can be seen in Figure 6.9 and Table 6.4 gives a comparison between simulated and measured torque ripple. The measured torque ripple had a difference of 9.5 % and, thus, compares well to the simulated torque ripple. By applying equation 6.2 a percentage torque ripple of 14.4 % was measured. This is a very good torque ripple for an MG considering the high gear ratio used and also that a cogging factor of 2 was used. Measuring the torque ripple for large machines is challenging and the fact that the measured value was so close to the simulated value shows that the MG was designed with sound mechanical integrity.

Since the torque ripple was found to be close to the simulated, skewing of the HS shaft was not required.

$$\tau_{ripple,\%} = \frac{\tau_{max} - \tau_{min}}{\tau_{avg}} \cdot 100\,\% \tag{6.2}$$

Table 6.4: Torque ripple comparison at 1500 rpm, blade angle 25°.

Simulation [N·m]	Measured [N·m]	Error [%]	Torque ripple [%]
2.1	2.3	9.5	14.4

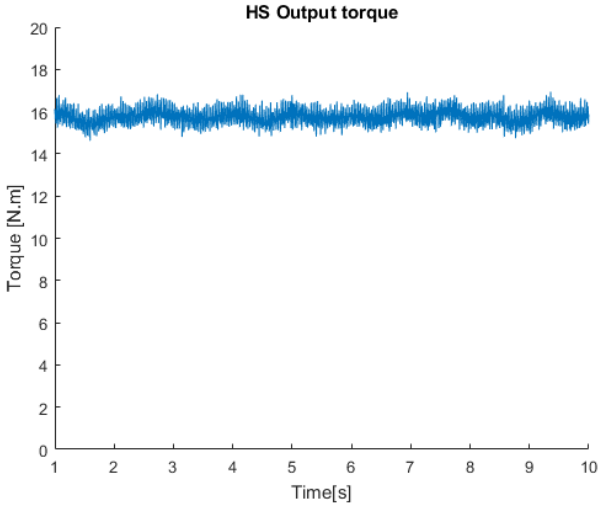

Figure 6.9: Output torque ripple of HS shaft at rated speed.

6.6 Discussion of Results

During the no-load evaluation of the initial MG high no-load losses were measured with a peak value of 720 W, relative to the rated power of 2.2 kW. As a result, two design improvements were made to the final MG, namely the improved design and the final design (see Chapter 5). These improvements were easily implemented due to the modular mechanical design of the MG.

The improved design showed a maximum no-load loss value of 290 W, while the final design had a maximum no-load loss value of 180 W, relative to the rated power of 2.8 kW. Furthermore, for an operating frequency similar to the first prototype the maximum no-load loss value of 120 W was obtained. This implies that at a similar operating frequency, the second prototype improved by a substantial 36.8 % decrease in no-load losses.

The improved and final design was then evaluated with a fan load, and their fan curves can be seen Figures 6.3 and 6.4, respectively. By comparing these

curves it is clear that for the final design the input and output curves are very close to each other indicating stable power transfer and high efficiency. This is confirmed by the efficiency maps for each design presented in Figures 6.5a and 6.5b, respectively. The highest efficiency for the improved design was 90 %, while the final design was 95 %. Furthermore, by comparing the full efficiency distribution a significant increase of efficiency was achieved throughout the domain of the final design. Thus, the entire range of the rated operating conditions increased.

The vibrational analysis for the second prototype showed that the dominant frequency and the excited frequency of the MG, relating to the transmission forces, was three times lower than the dominant frequency. On the other hand, the first prototype had a dominant frequency that coincided with the transmission forces. Thus, by comparison, the UMF and vibrations in the second prototype were greatly reduced and the MG was stable during operation.

The 2D simulation results compared well to what was expected for the initial and improved/final. The difference relative to the measured torque was 21.4 % and 18.2 %, respectively. Furthermore, the 3D simulated stall torque approximated the measured stall torque results within 0.9 % and 2.9 % for the initial and improved/final designs, respectively. The stall torque also increased by 40 N·m for the improved and final designs.

The measured torque ripple compares well to the simulated torque ripple and had a difference of 9.5 %. Furthermore, a percentage torque ripple of 14.4 % was measured. The fact that the measured value was close to the simulated value shows that the MG was designed with sound mechanical integrity and low vibrations are present in the MG.

Chapter 7

Conclusion and Recommendations

During this research, an MG was investigated as an alternative gear for ACC systems. This was done by defining various research objectives. Each objective was successfully accomplished by following the research approach and staying within the research scope, and the main findings of each objective are summarised below.

7.1 Discussion of Objectives

A previous MG prototype had an efficiency of 94 %, however the prototype had significantly higher no-load losses compared to a traditional mechanical gear. Thus, a mechanical case study was done to determine the source of these losses. From the case study it was observed that the shafts did not rotate concentrically which caused the air gap to be non-uniform. A vibration analysis showed the dominant frequency to be the MG pole frequency, which indicated that large forces were excited at the MG pole frequency which caused the non-uniform air gap. The root of this problem was identified as the large UMFs.

The UMF of the MG was studied and it was found that the magnitude of the forces changes significantly for different gear ratios. Thus, the importance of judicious selection of pole/slot combinations when designing an FMMG was realised. Furthermore, a criterion for identifying gear ratios with a minimum UMF was derived. Further analysis showed that for a fixed gear ratio the UMF was linearly proportional to the gear size, implying that for large MGs even larger UMFs exist and can become very problematic.

A second prototype was then developed by implementing the guidance developed from the UMF study. The internal gear parameters were obtained by applying two optimisations, namely: torque density and torque ripple. Furthermore, two design improvements were made on the prototype resulting in an initial, improved, and final design. Also, a motor-gear interface was designed,

and improvements were made for the manufacturing, assembly, and maintenance of the MG. Strength analysis on the shafts showed that the safety factor of the HS and LS shaft were 2.42 and 2.80, respectively. A modal analysis revealed that the prototype's resonance frequencies were higher than the operating frequency of the MG, indicating the excited frequencies are much lower than the modal frequencies.

A modular design for the MG was achieved by keeping the components symmetrical, and, as a result, reducing the manufacturing time and cost. A motor-gear interface was designed for the MG to allow the design to fit easily with to standard motor flanges. Manufacturing and maintenance techniques were developed for the MG, and various design considerations were made which allowed the MG to be easily reused. More specifically, a magnetic grip was designed to aid in the placing of the magnets.

A performance evaluation was done on the second prototype, and three designs were obtained, namely the initial design, the improved design, and the final design. At rated speed, the no-load losses for each design was measured to be 720 W, 290 W, and 180 W, relative to the rated power of 2.2 kW for the initial design and 2.8 kW for the improved/final design. For an operating frequency similar to the first prototype the maximum no-load loss value of 120 W was obtained, which indicates that the second prototype improved with 70 W of no-load losses. Furthermore, for an operating frequency similar to the first prototype a no-load loss value of 120 W was obtained which implies a decrease of 36.8 % in no-load losses.

Fan load results were presented for the improved and final designs, and the efficiency for both increased gradually with the transferred power until rated conditions were reached. The highest efficiency for the improved design was 90 %, while the final design was 95 %. Furthermore, the input and output fan curves for the final design were very close to each other, indicating stable power transfer and high efficiency and was confirmed by an efficiency map comparison. Furthermore, the entire efficiency distribution increased significantly for the final design. Thus, the entire range of the rated operating conditions increased.

Furthermore, a vibrational analysis revealed the dominant frequency to be the operating speed of the output shaft, while the amplitude of the excited frequency, relating to the transmission forces, of the MG was three times lower than the running speed, while, the first prototype had a dominant frequency of the transmission forces. Thus, by comparison, the UMF and vibrations in the second prototype were greatly reduced and the MG was stable during operation.

The stall torque results compared exceptionally well to the simulated results with a 0.9 % difference for the 3D initial design and a 2.9 % difference for the improved and final designs. The 2D simulation difference was 21.4 % and 18.2 % for the initial and improved/final designs, respectively. The stall torque also increased by 40 N·m for the improved and final designs. These results were

expected from the literature review.

The torque ripple compared well to the simulated torque ripple and had a difference of 9.5 %. The torque ripple percentage was found to be 14 %. Since the measured torque ripple was close to the simulated value the mechanical design was considered a great success with sound mechanical integrity and low vibrations.

7.2 Highlights

The research highlights are as follows:

Due to the design layout of the MG, assembly and disassembly was done with little effort. Furthermore, this allows for easy maintenance to be performed on the MG. The magnetic grip proved to be very helpful and increased the productivity of construction and reduced the risk of damage to the magnets or injury to employees. The motor-gear interface rounded off the product to industry standards and allows the gear to be easily attached to a motor flange. The modular mechanical design proved to be very useful and allowed the design to be easily improved and, also allows the prototype to be reused in future research.

Judicious materials selection for the final design helped ensure low magnetic flux leakages, which helped achieve an efficiency of 95 %, which is an improvement on the first prototype. Furthermore, by comparing the no-load losses of the first prototype to that of the second prototype a decrease of 36.8 % was observed, which is substantial.

A case study on the first prototype with a vibrational analysis revealed that large UMFs were present in the gear due to mechanical unsuitability and excessive vibrations. These UMFs were investigated and it was found that selecting the number of magnetic pole pairs has a great influence on the UMF. A guideline for selecting a gear ratio was derived, and this guideline was followed during the design of the second prototype. A vibrational analysis was done on the second prototype and it was found that the UMFs and vibrations were greatly reduced.

Furthermore, the torque ripple for large machines and gear ratios have been problematic in the past. During the evaluation, a torque was realised similar to the simulated torque ripple and the waveform was also similar. This further proved the mechanical integrity of the prototype.

Thus, UMFs were successfully identified, investigated, a solution was successfully obtained and verified by a vibrational analysis. As a result, the research of this project proves to be extremely valuable to the research field of MGs.

In conclusion, this research showed that by integrating the mechanical and electromagnetic design of an MG, it can be used as a viable alternative in ACC systems.

7.3 Recommendations

The housing of the initial and improved design developed in this thesis can be reused to develop a new MG using the guidelines presented in this research. The guidelines can then be further analysed to determine if even lower UMFs and lower torque ripple are possible.

The housing can also be reused to perform case studies on the internal electromagnetic losses caused by the HS rotor and in the fastening bolts of the housing and modulator. The effect of laminating the HS rotor can also be investigated to reduce the eddy-currents generated in it.

If the product goes into mass production cast iron is recommended as a cost-effective material for the housing. Also, the shafts should be considered to be made from stainless steel 316 to further reduce eddy-currents and flux leakage.

To further minimise the flux leakage and magnetisation of the bearings, it is suggested that full-ceramic and hybrid-ceramic bearings be investigated.

Research can also be done to determine how a step skew on the HS shaft will affect the torque ripple, as demonstrated in Figure 7.1.

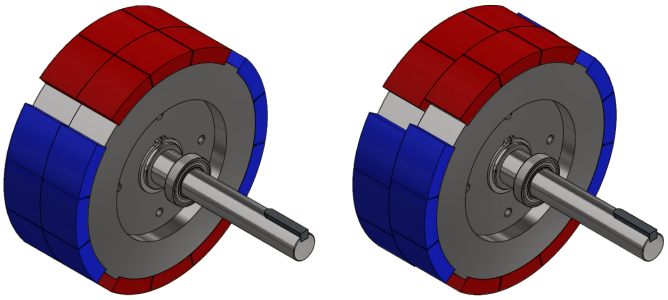

(a) (b)

Figure 7.1: Two views of HS assembly: (a) Normal. (b) Step skewed.

Appendices

Appendix A

Parameters

This Appendix contains all the various gear parameters, history plots for optimisations and sensitivity analysis.

A.1 Prototype 1 Gear Parameters

Table A.1: Design parameters of the first prototype (Matthee, 2016).

Parameter	Value
HS number of pole pairs	4
LS number of steel segments	15
PM carrier number of pole pairs	11
Gear outer radius [mm]	81.5
PM carrier yoke thickness [mm]	5.5
PM carrier magnet thickness [mm]	6
Modulator (LS) thickness [mm]	9
HS magnet thickness [mm]	6
HS yoke thickness [mm]	20
LS yoke thickness [mm]	6.5
Modulator segment inner thickness [ratio of pole pitch	0.57
Modulator segment outer thickness [ratio of pole pitch]	0.46
Modulator bridge thickness [mm]	0.65
Outer air-gap width [mm]	1.0
Inner air-gap width [mm]	1.0
PM carrier magnets volume [ratio of area]	0.90
HS magnets volume [ratio of area]	0.90
Stack length [mm]	100

A.2 UMF Simulation Gear Parameters

Table A.2: General 2D model design parameters.

Parameter	Value
HS number of pole pairs	2
LS modulator steel segments	23
Stator number of pole pairs	21
Gear ratio	11.5:1
Gear outer radius [mm]	122.25
Stack length [mm]	50
PM carrier magnet thickness [mm]	9
HS magnet thickness [mm]	9
Modulator (LS) thickness [mm]	13.5
HS yoke thickness [mm]	30
PM carrier yoke thickness [mm]	9.75
Modulator bridge thickness [mm]	0.978
Outer air-gap width [mm]	1.5
Inner air-gap width [mm]	1.5
Magnet grade	N48H
Flux density	1.4
Permitivity magnet	1.1196
PM carrier magnets volume [ratio of area]	0.90
HS magnets volume [ratio of area]	0.90
Modulator torque (2D results) [Nm]	285.27
LS torque (2D results) [Nm]	260.54
HS torque (2D results) [Nm]	24.73
LS Rated speed [rpm]	130.43
HS Rated speed [rpm]	1500

A.3 Final Gear Parameters

Table A.3: Final gear parameters.

Parameter	Value
HS number of pole pairs	2
LS modulator steel segments	22
Stator number of pole pairs	20
Gear ratio	11:1
Gear outer radius [mm]	106
Stack length [mm]	60
PM carrier magnet thickness [mm]	5
HS magnet thickness [mm]	10
Modulator (LS) thickness [mm]	10
HS yoke thickness [mm]	24
PM carrier yoke thickness [mm]	9
Modulator bridge thickness [mm]	0.35
Outer air-gap width [mm]	1
Inner air-gap width [mm]	1
Magnet grade	N48H
Flux density	1.4
Permitivity magnet	1.1196
PM carrier magnets volume [ratio of area]	0.878
HS magnets volume [ratio of area]	0.865
Modulator torque (3D results) [Nm]	236
Modulator torque (2D results) [Nm]	280.27
LS torque (2D results) [Nm]	255.54
HS torque (2D results) [Nm]	24.73
LS Rated speed [rpm]	136.4
HS Rated speed [rpm]	1500

A.4 History Plots

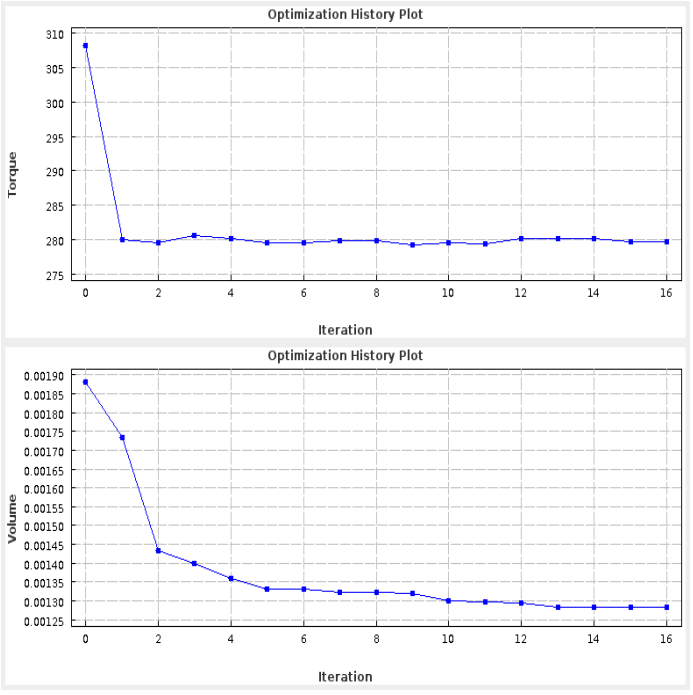

(a)

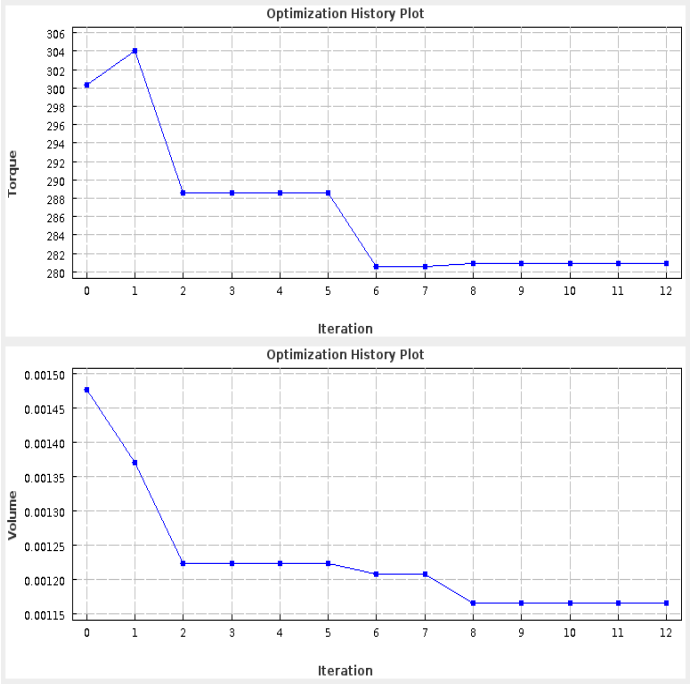

(b)

Figure A.1: History plots for: (a) MMFD. (b) PSO.

A.5 Sensitivity Analysis

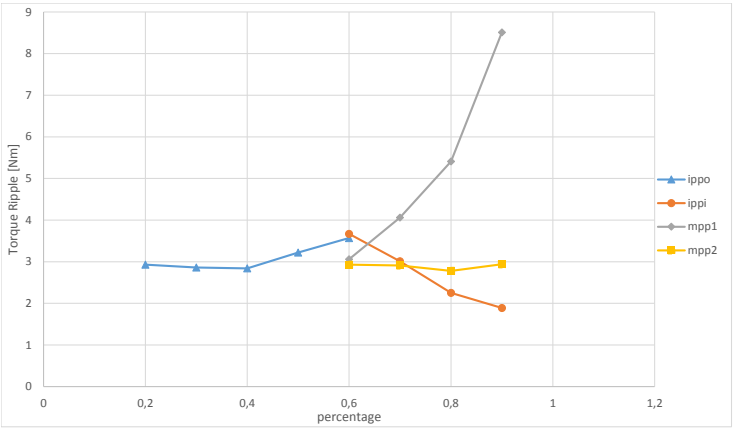

Figure A.2: OAT sensitivity study.

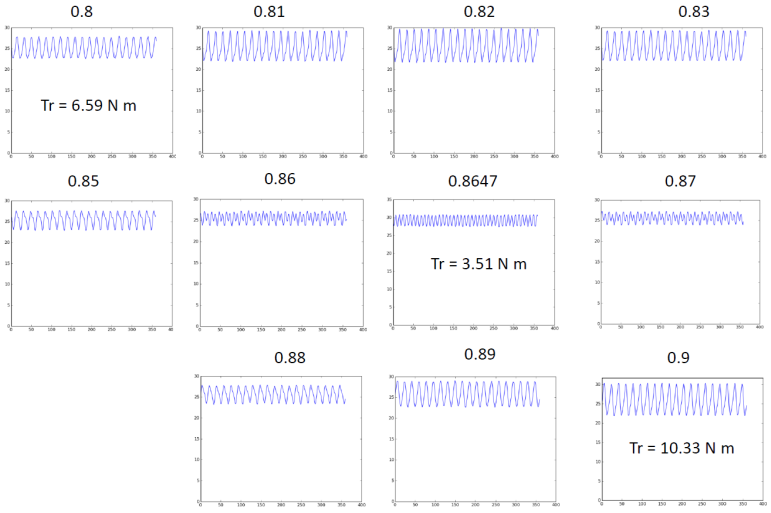

Figure A.3: OAT sensitivity study on MPP1, between 0.8 and 0.9.

Appendix B

Calculations

This Appendix contains all the various gear calculations described in the thesis, namely: specification calculations, shaft calculations, bearing calculations, and modulator bolt calculations.

B.1 Specification Calculations

Rated operating conditions of the input shaft

$P_{rated} := 2,2\ kW$ Power rating

$GR := 11$ Gear ratio

$n_{s1} := 1500\ rpm$ Output speed

$n_{s1} = 157,0796\ \frac{rad}{s}$ Output speed rad/s

$n_{s2} := \frac{n_{s1}}{GR} = 136,3636\ rpm$ Input speed

$n_{s2} := \frac{n_{s1}}{GR} = 14,28\ \frac{rad}{s}$ Input speed rad/s

$\tau_{s1} := \frac{P_{rated}}{n_{s1}} = 14,0056\ N\,m$ Rated output torque required

$\tau_{s2} := \tau_{s1} \cdot GR = 154,062\ N\,m$ Rated input torque required

$sf := 1,5$ Saftey factor

$\tau_{max} := \tau_{s1} \cdot sf = 21,0085\ N\,m$ Output maximum torque

$\tau_{2d} := 1,25 \cdot \tau_{max} = 26,2606\ N\,m$ Output torque required from 2D simulation

$\tau_{max2} := \tau_{s2} \cdot sf = 231,093\ N\,m$ Input maximum torque

$\tau_{2} := \tau_{2d} \cdot GR = 288,8662\ N\,m$ Input torque required from 2D simulation

Figure B.1: The design specification calculations of the FMMG.

B.2 Shaft Calculations

High speed shaft calculations:

Rated operating conditions of the input shaft

$n_{s1} := 1500\ rpm$ $P_{motor} := 2,2\ kW$

$n_{s1} = 157,0796\ \frac{rad}{s}$

$\tau_{s1} := \frac{P_{motor}}{n_{s1}} = 14,0056\ N\,m$ sf := 1,5 service factor

spf := 1,1 slip factor

$\tau_{max} := \tau_{s1} \cdot sf \cdot spf = 23,1093\ N\,m$

The critical area on this shaft was taken at the end where the shaft diameter is the smallest and the key stress concentration is present. Furthermore, the assumption of pure torsional stress was made since the UMF cancel out from the simulation.

Section details:

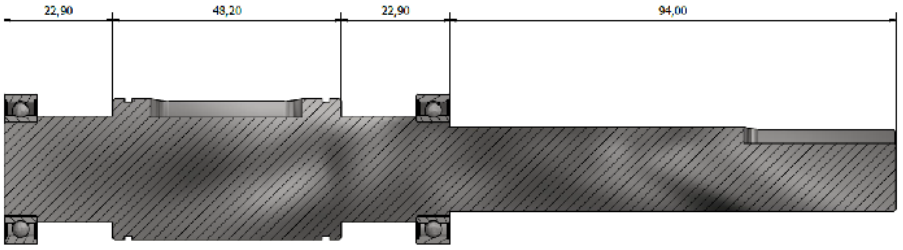

$d_1 := 18\ mm$

Read from table 7-1

$K_{t\_z} := 2,7$ $K_{ts\_z} := 2,2$ Worst Case if sharp corner is machined

$M_{max\_z} := 0 = 0\ N\,m$ $M_{min\_z} := 0 = 0\ N\,m$

$M_{m\_z} := \frac{M_{max\_z} + M_{min\_z}}{2} = 0\ N\,m$ $M_{a\_z} := \frac{M_{max\_z} - M_{min\_z}}{2} = 0\ N\,m$

$I_z := \frac{\pi}{64} \cdot \left(d_1^{\,4}\right) = 5,153 \cdot 10^{-9}\ m^4$

$\sigma_{m\_z} := \frac{M_{m\_z} \frac{d_1}{2}}{I_z} = 0$ $\sigma_{a\_z} := \frac{M_{a\_z} \frac{d_1}{2}}{I_z} = 0\ MPa$

Figure B.2: The shaft calculation page 1.

$T_{max\_z} = \tau_{max} = 23,1093\,N\,m$ $T_{min\_z} = 0 = 0\,N\,m$

$T_{m\_z} = \frac{T_{max\_z} + T_{min\_z}}{2} = 11,5546\,N\,m$ $T_{a\_z} = \frac{T_{max\_z} - T_{min\_z}}{2} = 11,5546\,N\,m$

$J_{G\_z} = 2 \cdot I_z = 1,0306 \cdot 10^{-8}\,m^4$

$\tau_{m\_z} = \frac{T_{m\_z} \frac{d_1}{2}}{J_{G\_z}} = 10,0904\,MPa$ $\tau_{a\_z} = \frac{T_{a\_z} \frac{d_1}{2}}{J_{G\_z}} = 10,0904\,MPa$

$\sigma'_{m\_z} = \sqrt{\left(K_{t\_z} \sigma_{m\_z}\right)^2 + 3 \cdot \left(K_{ts\_z} \tau_{m\_z}\right)^2} = 38,4497\,MPa$

$\sigma'_{a\_z} = \sqrt{\left(K_{t\_z} \sigma_{a\_z}\right)^2 + 3 \cdot \left(K_{ts\_z} \tau_{a\_z}\right)^2} = 38,4497\,MPa$

Material Properties (EN 8) Mild Steel

$S_y = 280\,MPa$ $S_{ut} = 550\,MPa$ $E = 200\,GPa$ (Table A-20 Shigley)

Using the Marin equation to calculate the endurance limit at the various critical points on the shaft.

Estimate the endurance limit:

if $S_{ut} \le 1400\,MPa$

$S'_e = 0,5 \cdot S_{ut}$ (eqn. 6-8)

else

$S'_e = 1400\,MPa$

$S'_e = 275\,MPa$

Surface condition modification factor:

$a = 4,51$ $b = -0,265$ Read from table 6-2 for Machined or cold-drawn

$k_a = a \cdot \left(\frac{S_{ut}}{1\,MPa}\right)^b = 0,8472$ (eqn. 6-19)

Size modification factor:

$k_{b\_z} = 1,24 \cdot \left(\frac{d_1}{1\,mm}\right)^{-0,107} = 0,9101$ (eqn. 6-20)

Load modification factor:

$k_c = 0,59$ (eqn. 6-26)

Reliability factor:

Figure B.3: The shaft calculation page 2.

Read from table 6-5 for 99.99% reliability

Marin equation for endurance limit:

$k_e = 0,897$ (eqn. 6-18)

$S_{e\_z} = k_a k_{b\_z} k_c k_e S'_e = 112,2187\,MPa$

Use the modified-Goodman equation to determine the safety factor for each section:

Section z:

$$n_z = \frac{1}{\frac{\sigma'_{a\_z}}{S_{e\_z}} + \frac{\sigma'_{m\_z}}{S_{ut}}} = 2,424 \quad \text{(eqn. 6-46)}$$

The endurance safety factor for the HS shaft is given above, and is considered a good safety factor.

Low speed high torque shaft calculations:

Rated operating conditions of the output shaft

$GR = 11$ Gear ratio

$\tau_{maxLS} = \tau_{max} GR = 254,2023\,N\,m$

$d_1 = 45\,mm$ $d_2 = 29,6\,mm$

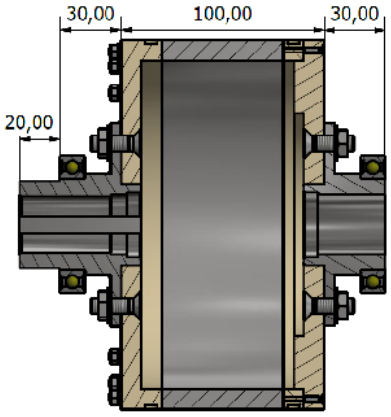

Read from table 7-1

Worst Case if sharp corner is machined

$K_{t\_z} = 2,7$ $K_{ts\_z} = 2,2$

$M_{max\_z} = 0,0\,N\,m$ $M_{min\_z} = 0,0\,N\,m$

$$M_{m\_z} = \frac{M_{max\_z} + M_{min\_z}}{2} = 0\,N\,m$$

$$M_{a\_z} = \frac{M_{max\_z} - M_{min\_z}}{2} = 0\,N\,m$$

Figure B.4: The shaft calculation page 3.

$$I_z = \frac{\pi}{64}\left(d_1^{\,4} - d_2^{\,4}\right) = 1,6361 \cdot 10^{-7}\ m^4$$

$$\sigma_{m\_z} = \frac{M_{m\_z}\frac{d_1}{2}}{I_z} = 0 \qquad \sigma_{a\_z} = \frac{M_{a\_z}\frac{d_1}{2}}{I_z} = 0\ MPa$$

$$T_{max\_z} = \tau_{maxLS} = 254,2023\ N\,m \qquad T_{min\_z} = 0 = 0\ N\,m$$

$$T_{m\_z} = \frac{T_{max\_z} + T_{min\_z}}{2} = 127,1011\ N\,m$$

$$J_{G\_z} = 2 \cdot I_z = 3,2721 \cdot 10^{-7}\ m^4 \qquad T_{a\_z} = \frac{T_{max\_z} - T_{min\_z}}{2} = 127,1011\ N\,m$$

$$\tau_{m\_z} = \frac{T_{m\_z}\frac{d_1}{2}}{J_{G\_z}} = 8,7398\ MPa \qquad \tau_{a\_z} = \frac{T_{a\_z}\frac{d_1}{2}}{J_{G\_z}} = 8,7398\ MPa$$

$$\sigma'_{m\_z} = \sqrt{\left(K_{t\_z}\sigma_{m\_z}\right)^2 + 3\left(K_{ts\_z}\tau_{m\_z}\right)^2} = 33,3031\ MPa$$

$$\sigma'_{a\_z} = \sqrt{\left(K_{t\_z}\sigma_{a\_z}\right)^2 + 3\left(K_{ts\_z}\tau_{a\_z}\right)^2} = 33,3031\ MPa$$

Use the modified-Goodman equation to determine the safety factor for each section:

Section z:

$$n_z = \frac{1}{\frac{\sigma'_{a\_z}}{S_{e\_z}} + \frac{\sigma'_{m\_z}}{S_{ut}}} = 2,7986 \qquad \text{(eqn. 6-46)}$$

The endurance safety factor for the LS shaft is given above, and is considered a good safety factor.

Figure B.5: The shaft calculation page 4.

B.3 Bearing Calculations

HS Bearing Calculation:

Suitable bearings were chosen using the skf catalog and the required
These bearings will now be checked using calculations to ensure that they
suitable for the application

Calculation factors, from REF: (SKF)

Bearings W 61804-2Z

Worst case

Input shaft speed for maximum torque case which will put the highest strain on the bearings

$V_{in} := 1500\,rpm$

$Operate\_Hours := 10^5\,hr = 6 \cdot 10^6\,min$

$L_{expect} := Operate\_Hours\,V_{in} = 9 \cdot 10^9\,rev$ Expected life in revolutions

$HS_{weight} := 8,511\,kg$ From Inventor

$d := 20\,mm$ Inner Diameter

$D := 32\,mm$ Outer Diameter

$b := 7\,mm$ Width

$C := 3,12\,kN$ Dynamic Load Rating

$C_0 := 2,08\,kN$ Static Load Rating

$f_0 := 13,3$ Calculation Factor

$F_a := 0\,N$ Axial Force

$F_{sim} := 5\,N$

$F_r := HS_{weight} g_e + F_{sim} = 88,4644\,N$ Radial Force

$k_r := 0,02$

$F_{rm} := k_r$

$f_0 \frac{F_a}{C_0} = 0$

$k := 3$ Ball Bearing

$V := 1$ shaft rotates

$X := 0,46$ Radial factor

$R := F_r$ Radial load

$Y := 1,71$ Thrust factor

$T := F_a$ Applied thrust load

$P := V \cdot X \cdot R + Y \cdot T$ Equivalent Load

$L := \left(\frac{C}{P}\right)^k \cdot 10^6 = 4,507 \cdot 10^{11}$ Rated Bearing Life in revolutions, Introduction to machine design 244, Eqn (2.22)

$S_0 := \frac{C_0}{P} = 51,1137$ Static safety factor

$s := \frac{L}{\frac{L_{expect}}{rev}} = 50,0774$ Dynamic saftey factor based on bearing life

Figure B.6: The HS bearing calculation.

LS Bearing Calculation:

Suitable bearings were chosen using the skf catalog and the required
These bearings will now be checked using calculations to ensure that they
suitable for the application

Calculation factors, from REF: (SKF)

Bearings (61809-2RZ)

Worst case

Input shaft speed for maximum torque case which will put the highest strain on the bearings

$V_{in} := \frac{1500}{11}\,rpm = 136,3636\,rpm$

$Operate\_Hours := 10^{5}\,hr = 6 \cdot 10^{6}\,min$

$L_{expect} := Operate\_Hours\,V_{in} = 8,1818 \cdot 10^{8}\,rev$ Expected life in revolutions

Bearing A SKF (61809-2RZ)

$LS_{weight} := 8,511\,kg + 4,00\,kg$ From Inventor

$d := 45\,mm$ Inner Diameter

$D := 58\,mm$ Outer Diameter

$b := 7\,mm$ Width

$C := 4,94\,kN$ Dynamic Load Rating

$C_0 := 5\,kN$ Static Load Rating

$f_0 := 9,1$ Calculation Factor

$F_a := 0\,N$ Axial Force

$F_{sim} := 5\,N$

$F_r := LS_{weight}\,g_e + F_{sim} = 127,691\,N$ Radial Force

$k_r := 0,02$

$F_{rm} := k_r$

$f_0 \frac{F_a}{C_0} = 0$

$k := 3$ Ball Bearing

$V := 1$ shaft rotates

$X := 0,46$ Radial factor

$R := F_r$ Radial load

$Y := 1,71$ Thrust factor

$T := F_a$ Applied thrust load

$P := V \cdot X \cdot R + Y \cdot T$ Equivalent Load

$L := \left(\frac{C}{P}\right)^{k} \cdot 10^{6} = 5,9488 \cdot 10^{11}$ Rated Bearing Life in revolutions, Introduction to machine design 244, Eqn (2.22)

$S_0 := \frac{C_0}{P} = 85,124$ Static safety factor

$s := \frac{L}{\frac{L_{expect}}{rev}} = 727,0708$ Dynamic saftey factor based on bearing life

Figure B.7: The LS bearing calculation.

B.4 Modulator Bolt Calculations

Shaft to bolt analysis

CASE 1: LS Shaft to plates

$n_{bolts} := 4$ number of bolts:

$r_{shaft} := \frac{65}{2}\,mm = 0,0325\,m$ radius to bolts

$F := \frac{Torque}{r_{shaft}} = 5076,9231\,N$

$A_{bolt} := \frac{d_{bolt}^{2}}{4} \cdot \pi = 3,0798 \cdot 10^{-5}\,m^{2}$

$\tau := \frac{F}{n_{bolts} \cdot A_{bolt}} = 4,1212 \cdot 10^{7}\,Pa$

$n := \frac{S_{sy}}{\tau} = 4,7603$ Safety factor

$Torque := 165\,N\,m$ Torque from simulation

$d_{bolt} := 6,262\,mm$ minor diameter of bolt

$S_y := 340\,MPa$ Grade 4.8

$S_{sy} := 0,577 \cdot S_y = 1,9618 \cdot 10^{8}\,Pa$

CASE 2: Lid 1 and Compressing Ring

$n_{bolts} := 22$ number of bolts:

$r_{shaft} := 63,5\,mm$ radius to bolts

$d_{bolt} := 3,141\,mm$ minor diameter of bolt

$Torque := 265\,N\,m$ Torque from simulation

$F := \frac{Torque}{r_{shaft}} = 4173,2283\,N$

$A_{bolt} := \frac{d_{bolt}^{2}}{4} \cdot \pi = 7,7486 \cdot 10^{-6}\,m^{2}$

$\tau := \frac{F}{n_{bolts} \cdot A_{bolt}} = 2,4481 \cdot 10^{7}\,Pa$

$n := \frac{S_{sy}}{\tau} = 8,0137$ Safety factor

$S_y := 340\,MPa$ Grade 4.8

$S_{sy} := 0,577 \cdot S_y = 1,9618 \cdot 10^{8}\,Pa$

Figure B.8: The bolt calculation.

Appendix C

Motor Flange

This Appendix shows a motor flange which was used in the testing setup.

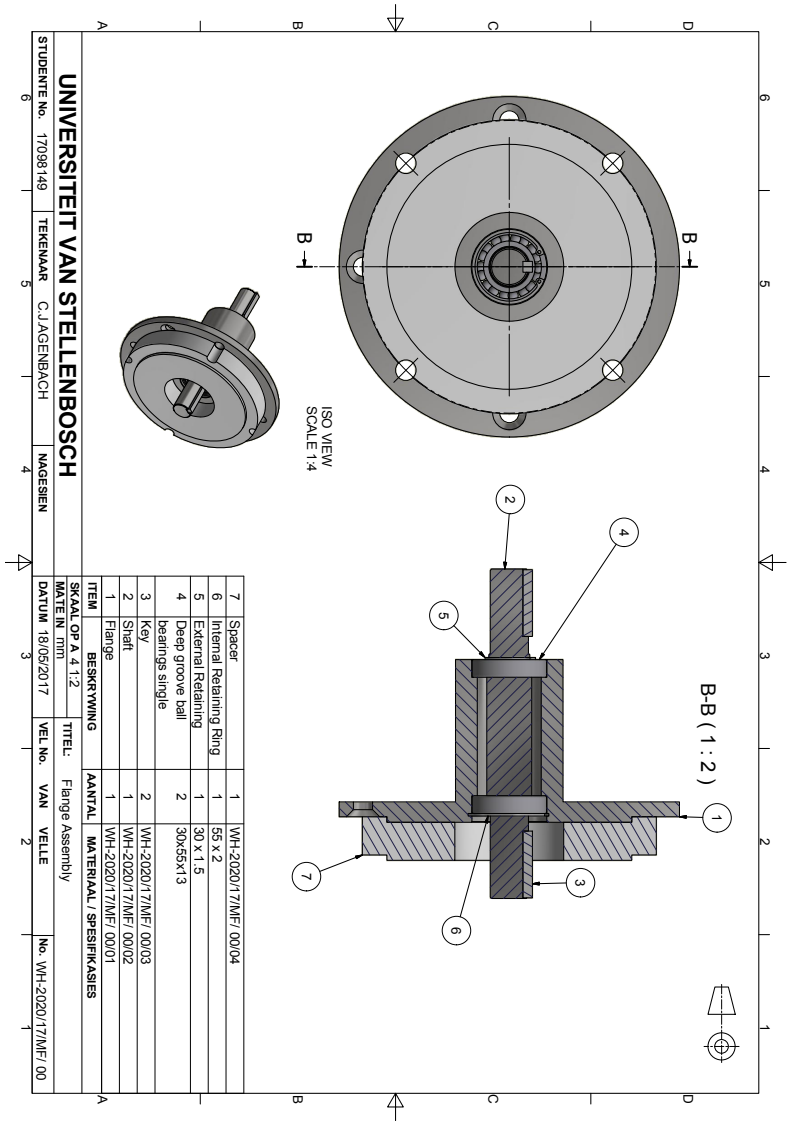

Appendix D

Calibration of Equipment

This Appendix discusses and demonstrates the calibration of the piezoelectric accelerometer and torque sensors.

D.1 Accelerometer

The piezoelectric accelerometer (Brüel Kjær type 4381) and charge amplifier (Brüel Kjær type 2635) used in this thesis were calibrated using a SV111 Vibration Calibrator, as seen in Figure D.1a. The accelerometer is placed on the vibration plate, while the plate acceleration and frequency of oscillation are specified in the settings panel, as seen in Figure D.1b.

The accelerometer, cable and charge amplifier was calibrated as a unit.The sensitivity of the accelerometer was established by relating the output voltage of the accelerometer to the motion of the vibration plate. The calibration was performed in a quiet environment where no external factors could influence the motion measured by the accelerometers.

(a) (b)

Figure D.1: Accelerometer calibration: (a) Vibration calibrator setup. (b) Vibration calibrator settings.

D.2 Torque Sensors

The calibration of the torque sensors was done by the manufacturer, Lorenz® Messtechnik. However, to verify that the torque sensors both measured accurately they were placed in series as illustrated in Figure D.2 and their speed and torque values compared very well.

Figure D.2: Torque sensor calibration setup.

Appendix E

UMF Study

This Appendix gives a study of the UMF for various pole pair combinations.

Table E.1: Force study 1.

Case	freq	Ph	Pl	q	Gr	Grq	fch	fcl	UMF [N]
1	25	1	9	10	9	10	2	2	7
2	25	1	10	11	10	11	1	1	185
3	25	1	11	12	11	12	2	2	16
4	25	1	12	13	12	13	1	1	335
5	25	1	13	14	13	14	2	2	9
6	25	1	13	14	13	14	2	2	385
7	50	2	18	20	9	10	4	4	13
8	50	2	19	21	9,5	10,5	1	1	100
9	50	2	20	22	10	11	2	2	4
10	50	2	21	23	10,5	11,5	1	1	75
11	50	2	22	24	11	12	4	4	28
12	50	2	23	25	11,5	12,5	1	1	200
13	50	2	24	26	12	13	2	2	10
14	50	2	25	27	12,5	13,5	1	1	80
15	50	2	26	28	13	14	4	4	23
16	50	2	27	29	13,5	14,5	1	1	250
17	50	2	28	30	14	15	2	2	12
18	50	2	29	31	14,5	15,5	1	1	78
19	50	2	30	32	15	16	4	4	3
20	75	3	27	30	9	10	6	6	17
21	75	3	30	33	10	11	3	3	13
22	75	3	31	34	10,33	11,33	2	2	10
23	75	3	32	35	10,67	11,67	1	1	46
24	75	3	33	36	11	12	6	6	8
25	75	3	34	37	11,33	12,33	1	1	168

Table E.2: Force study 2.

Case	freq	Ph	Pl	q	Gr	Grq	fch	fcl	UMF [N]
26	75	3	35	38	11,67	12,67	2	2	34
27	75	3	36	39	12	13	3	3	28
28	75	3	37	40	12,33	13,33	2	2	2
29	75	3	38	41	12,67	13,67	1	1	40
30	75	3	39	42	13	14	6	6	35
31	75	3	40	43	13,33	14,33	1	1	200
32	75	3	41	44	13,67	14,67	2	2	8
33	75	3	42	45	14	15	3	3	25
34	75	3	43	46	14,33	15,33	2	2	7,5
35	75	3	44	47	14,67	15,67	1	1	33
36	100	4	36	40	9	10	8	8	8
37	100	4	40	44	10	11	4	4	5
38	100	4	41	45	10,25	11,25	1	1	11
39	100	4	42	46	10,5	11,5	2	2	7
40	100	4	43	47	10,75	11,75	1	1	33
41	100	4	44	48	11	12	8	8	4
42	100	4	45	49	11,25	12,25	1	1	180
43	100	4	46	50	11,5	12,5	2	2	8
44	100	4	47	51	11,75	12,75	1	1	11
45	100	4	48	52	12	13	4	4	6
46	100	4	49	53	12,25	13,25	1	1	10
47	100	4	50	54	12,5	13,5	2	2	8
48	100	4	51	55	12,75	13,75	1	1	28
49	100	4	52	56	13	14	8	8	52
50	100	4	53	57	13,25	14,25	1	1	165
51	100	4	54	58	13,5	14,5	2	2	8
52	100	4	55	59	13,75	14,75	1	1	17
53	100	4	56	60	14	15	4	4	9
54	100	4	57	61	14,25	15,25	1	1	8
55	100	4	58	62	14,5	15,5	2	2	60
56	100	4	59	63	14,75	15,75	1	1	24
57	125	5	45	50	9	10	10	10	7
58	125	5	50	55	10	11	5	5	12
59	125	5	55	60	11	12	10	10	8
60	125	5	60	65	12	13	5	5	5
61	125	5	65	70	13	14	10	10	6
62	125	5	70	75	14	15	5	5	8
63	125	5	75	80	15	16	10	10	12

Appendix F

Construction

This Appendix shows the construction of the magnetic gear.

F.1 Main Assembly

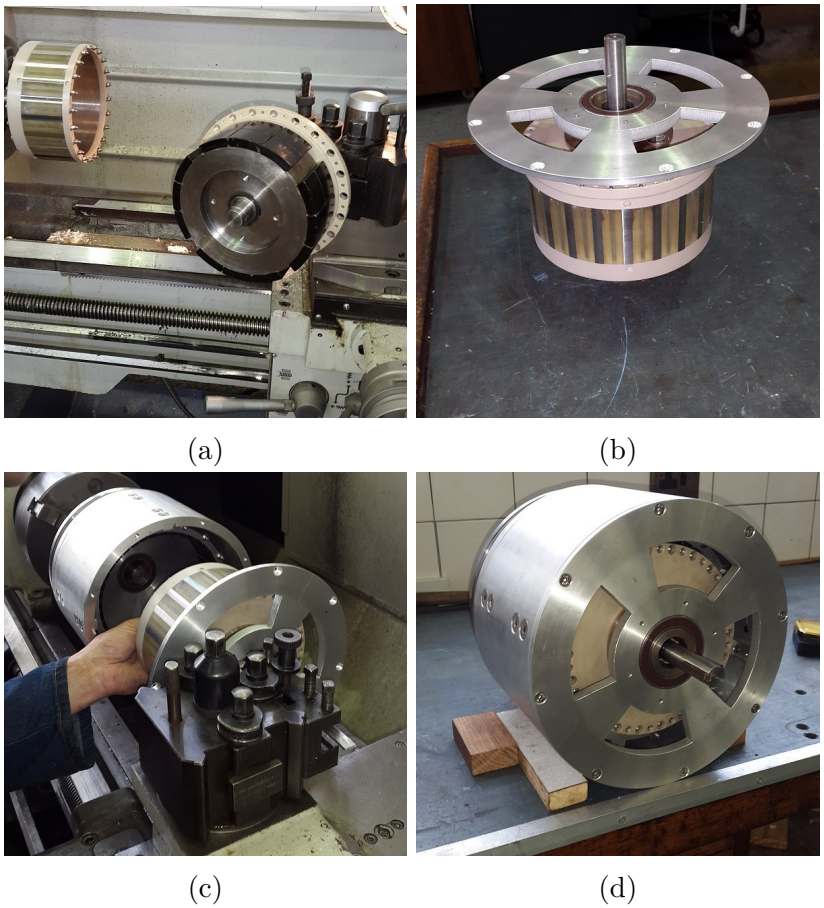

(a) (b)

(c) (d)

Figure F.1: Four views of the main assembly.

F.2 Housing & Low Speed Shaft

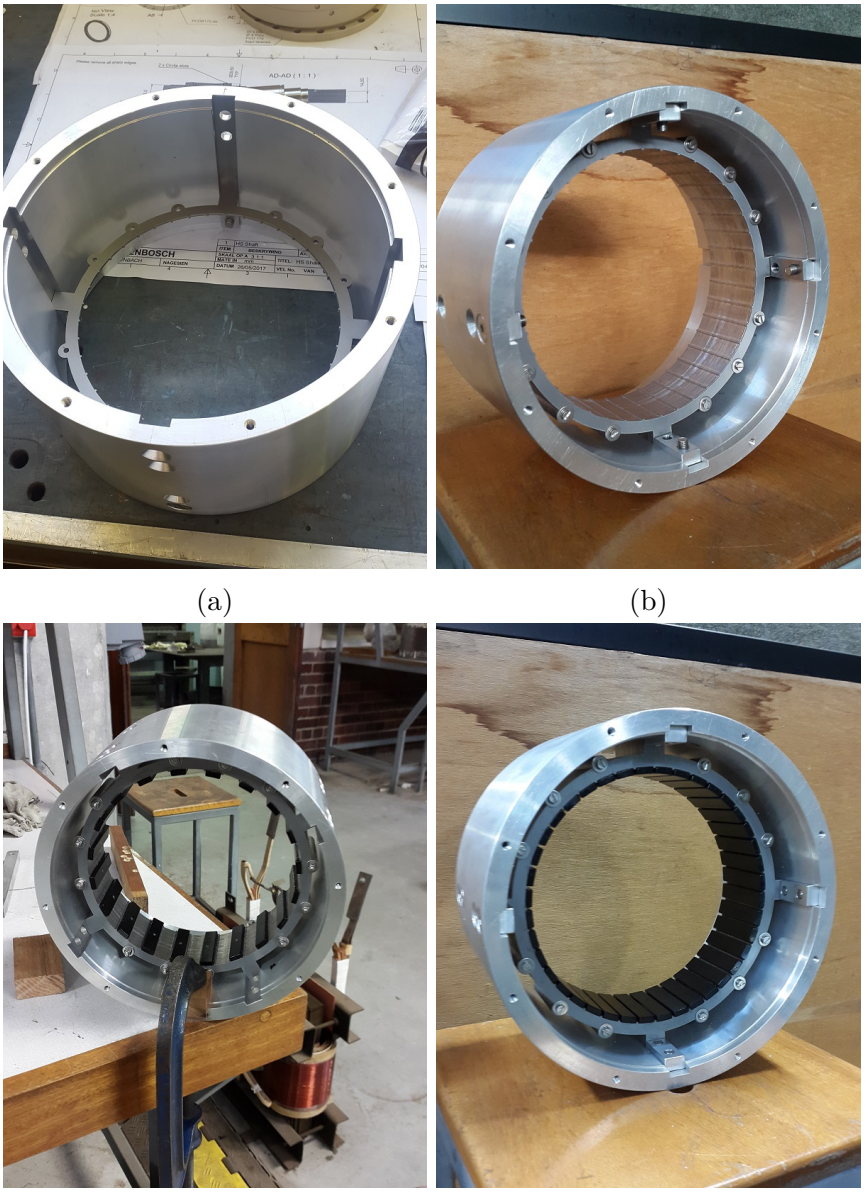

(a) (b)

(c) (d)

Figure F.2: Four views of the construction of the housing.

F.3 Modulator

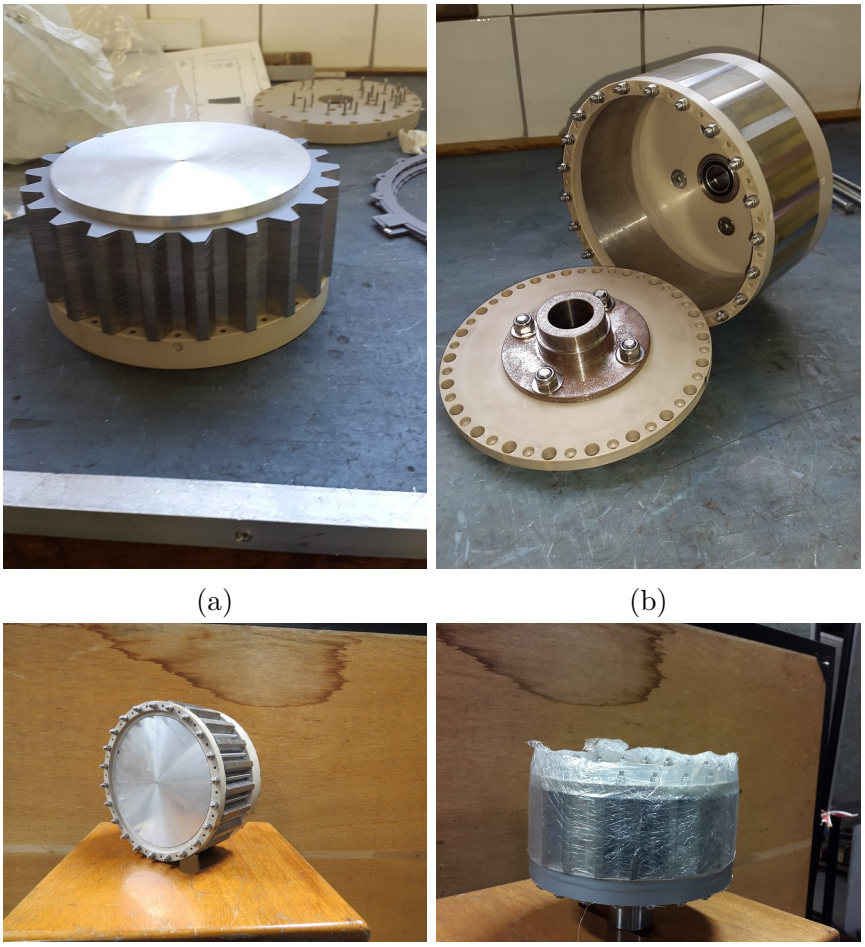

(a) (b)

(c) (d)

Figure F.3: Four views of the construction of the modulator.

F.4 High Speed Shaft

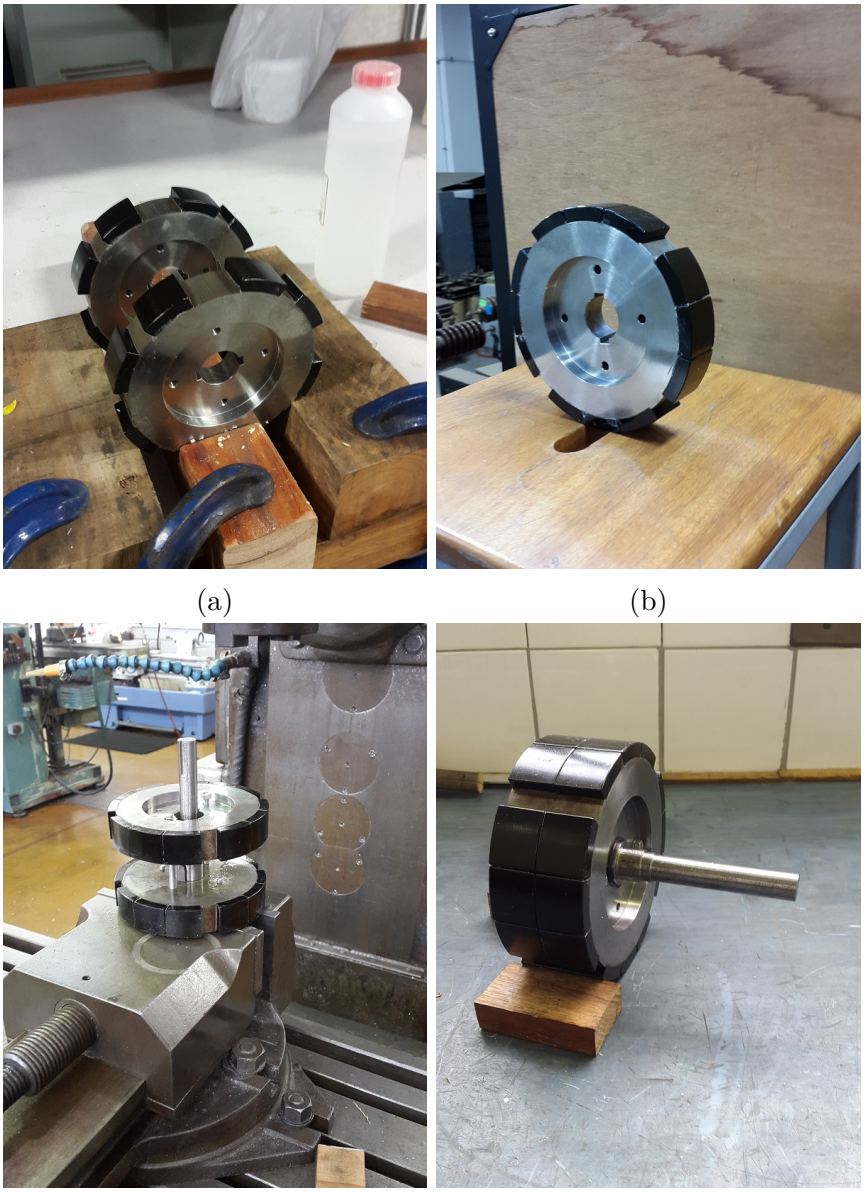

(a) (b)

(c) (d)

Figure F.4: Four views of the construction of the high-speed assembly.

Appendix G

Evaluation Setup & Data

This Appendix shows the stall torque setup and spectograms for the vibration analysis.

G.1 Stall Torque Setup

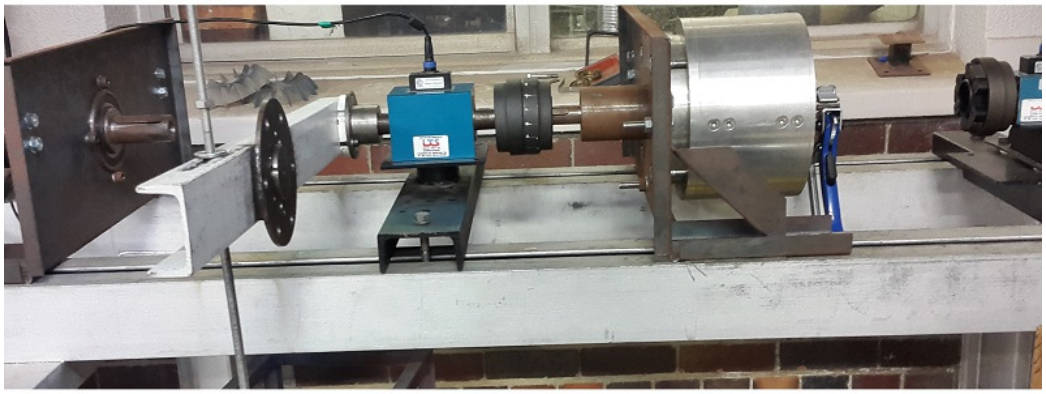

Figure G.1: Stall torque setup.

G.2 Spectograms for vibration analysis

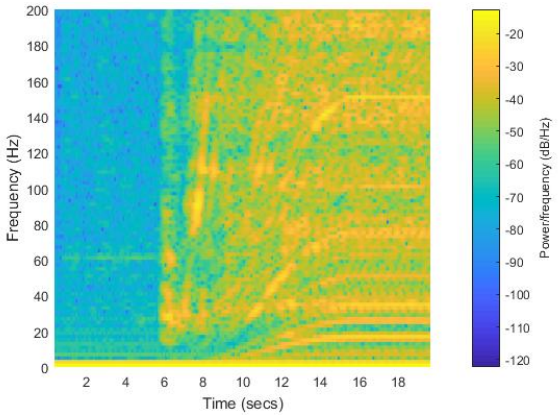

(a)

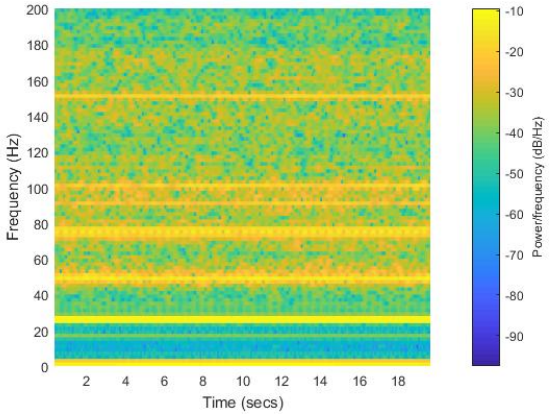

(b)

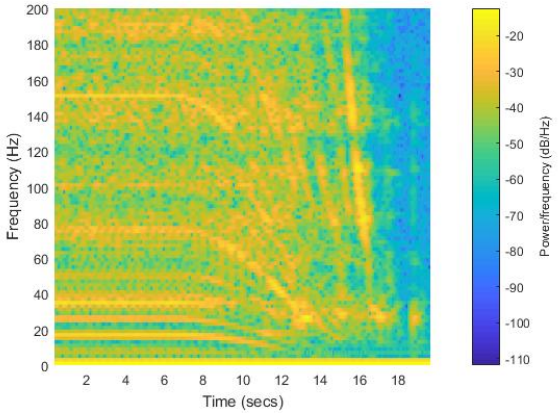

(c)

Figure G.2: Three spectograms for vibration analysis of the test setup: (a) Ramp up. (b) Rated speed. (c) Ramp down.

List of References

ANA (2016 January). Women artisans at forefront of medupi project. Available at: https://www.ofm.co.za/article/human-interest/176818/women-artisans-at-forefront-of-medupi-project

Armstrong, C. (1901 November 26). Power-transmitting device. US Patent 687,292. Available at: https://www.google.com/patents/US687292

Atallah, K., Calverley, S. and Howe, D. (2004). Design, analysis and realisation of a high-performance magnetic gear. *IEE Proceedings-Electric Power Applications*, vol. 151, no. 2, pp. 135–143.

Atallah, K. and Howe, D. (2001). A novel high-performance magnetic gear. *IEEE Transactions on magnetics*, vol. 37, no. 4, pp. 2844–2846.

Baermann, M. (1974 June 4). Magnetic worm drive. US Patent 3,814,962.

Bronn, L., Wang, R. and Kamper, M. (2010). Development of a shutter type magnetic gear. In: *Proceedings of the 19th Southern African Universities power engineering conference (SAUPEC)*, pp. 78–82.

Budynas, R.G. and Nisbett, J.K. (2011). *Shigley's Mechanical Engineering Design*. McGraw-Hill.

Chaari, F., Romdhane, M.B., Baccar, W., Fakhfakh, T. and Haddar, M. (2012). Windage power loss in spur gear sets. *Wseas transactions on applied and theoretical mechanics*, vol. 7, no. 2, pp. 159–168.

Desvaux, M., Multon, B., Ahmed, H.B. and Sire, S. (2017). Behaviour comparison between mechanical epicyclic gears and magnetic gears. In: *International Symposiu on Multibody Systems and Mechatronics*, pp. 401–410. Springer.

Dieter, G.E. and Schmidt, L.C. (2013). *Engineering Design*. 5th edn. McGraw-Hill.

Emetor, A. (2017). *Emetor: Torque ripple* [Online]. Available at: http://www.emetor.org/glossary/torque-ripple/

Fernando, N. and Saha, S. (2017). Torsional shear stress minimization techniques and implications on electromagnetic performance of flux-modulated double rotors. *IEEE Transactions on Energy Conversion*.

Frank, N.W. and Toliyat, H.A. (2009*a*). Gearing ratios of a magnetic gear for marine applications. In: *Electric Ship Technologies Symposium, 2009. ESTS 2009. IEEE*, pp. 477–481. IEEE.

Frank, N.W. and Toliyat, H.A. (2009*b*). Gearing ratios of a magnetic gear for wind turbines. In: *Electric Machines and Drives Conference, 2009. IEMDC'09. IEEE International*, pp. 1224–1230. IEEE.

Frank, N.W. and Toliyat, H.A. (2011). Analysis of the concentric planetary magnetic gear with strengthened stator and interior permanent magnet inner rotor. *IEEE Transactions on Industry Applications*, vol. 47, no. 4, pp. 1652–1660.

Fukuoka, M., Nakamura, K. and Ichinokura, O. (2011). Dynamic simulation of planetary type magnetic gear based on reluctance network analysis. In: *Power Electronics and Applications (EPE 2011), Proceedings of the 2011-14th European Conference on*, pp. 1–7. IEEE.

Furlani, E.P. (2001). *Permanent Magnet and Electromechanical Devices*. New York: Academic Press.

Ge, Y.-J., Nie, C.-Y. and Xin, Q. (2012). A three dimensional analytical calculation of the air-gap magnetic field and torque of coaxial magnetic gears. *Progress In Electromagnetics Research*, vol. 131, pp. 391–407.

Gerber, S. (2011). *A finite element based optimisation tool for electrical machines*. Master's thesis, Stellenbosch: University of Stellenbosch.

Gerber, S. (2015). *Evaluation and design aspects of magnetic gears and magnetically geared electrical machines*. Ph.D. thesis, Stellenbosch: Stellenbosch University.

Gerber, S. (2016 May). *SEMFEM Part 1: What is SEMFEM?* [Online]. Available at: `http://www0.sun.ac.za/semfem/tut_p1.html`

Gerber, S. and Wang, R. (2013). Evaluation of a prototype magnetic gear. In: *Industrial Technology (ICIT), 2013 IEEE International Conference on*, pp. 319–324. IEEE.

Gerber, S. and Wang, R. (2014). Analysis of the end-effects in magnetic gears and magnetically geared machines. In: *Electrical Machines (ICEM), 2014 International Conference on*, pp. 396–402. IEEE.

Gillet, C. and Friedrich, A. (2015). Guidelines for designing a concentrator for high-current sensing applications with an allegro hall-effect sensor ic. Tech. Rep., Allegro MicroSystems, LLC.

Goldschagg, H. (2013). Acc fan gearboxes: Eskom's experience in selection and maintenance of acc gearboxes. In: *ACCUG Navada conference*.

Gouda, E., Mezani, S., Baghli, L. and Rezzoug, A. (2011). Comparative study between mechanical and magnetic planetary gears. *IEEE Transactions on Magnetics*, vol. 47, no. 2, pp. 439–450.

Hanly, S. (2016 June 16). *Vibration Analysis: FFT, PSD, and Spectrogram Basics* [Online].
Available at: `https://blog.mide.com/vibration-analysis-fft-psd-and-spectrogram`

Harris, T.A. (2001). *Rolling bearing analysis*. John Wiley and sons.

Huang, C.-C., Tsai, M.-C., Dorrell, D.G. and Lin, B.-J. (2008). Development of a magnetic planetary gearbox. *IEEE Transactions on Magnetics*, vol. 44, no. 3, pp. 403–412.

Integrated Publishing, I. (2017 October). *DC GENERATOR THEORY: Hysteresis Loss* [Online].
Available at: `http://nuclearpowertraining.tpub.com/h1011v2/css/Hysteresis-Losses-89.htm`

Islam, R. and Husain, I. (2009). Analytical model for predicting noise and vibration in permanent magnet synchronous motors. In: *Energy Conversion Congress and Exposition, 2009. ECCE 2009. IEEE*, pp. 3461–3468. IEEE.

Jian, L., Xu, G., Mi, C.C., Chau, K. and Chan, C. (2011). Analytical method for magnetic field calculation in a low-speed permanent-magnet harmonic machine. *IEEE Transactions on Energy Conversion*, vol. 26, no. 3, pp. 862–870.

Kröger, D.G. (2004). *Air-cooled heat exchangers and cooling towers*, vol. 1. PennWell Books.

Lee, J. and Chang, J. (2017). Analysis of the vibration characteristics of coaxial magnetic gear. *IEEE Transactions on Magnetics*, vol. 53, no. 6, pp. 1–4.

Li, Y., Tang, D., Zhang, J. and Wen, J. (2011). An experimental study of pulsatile airflow in the fan inlet of an air-cooling heat exchanger using power spectrum analysis. In: *Power Engineering and Automation Conference (PEAM), 2011 IEEE*, vol. 1, pp. 138–141. IEEE.

Liu, P., Duan, H. and Zhao, W. (2009*a*). Numerical investigation of hot air recirculation of air-cooled condensers at a large power plant. *Applied Thermal Engineering*, vol. 29, no. 10, pp. 1927–1934.

Liu, X., Chau, K., Jiang, J. and Yu, C. (2009*b*). Design and analysis of interior-magnet outer-rotor concentric magnetic gears. *Journal of Applied Physics*, vol. 105, no. 7, p. 07F101.

Lubin, T., Mezani, S. and Rezzoug, A. (2010). Analytical computation of the magnetic field distribution in a magnetic gear. *IEEE Transactions on magnetics*, vol. 46, no. 7, pp. 2611–2621.

Matthee, A. (2016). *Development of a Magnetic Gear for Dry-Cooling Power Plant Applications*. Master's thesis, Stellenbosch University.

Nair, S.S., Wang, J., Chen, L., Chin, R., Manolas, I. and Svechkarenko, D. (2016). Prediction of 3-d high-frequency eddy current loss in rotor magnets of spm machines. *IEEE Transactions on Magnetics*, vol. 52, no. 9, pp. 1–10.

Nakamura, K. and Ichinokura, O. (2008). Dynamic simulation of pm motor drive system based on reluctance network analysis. In: *Power Electronics and Motion Control Conference, 2008. EPE-PEMC 2008. 13th*, pp. 758–762. IEEE.

Nave, R. (2016 October). *hyperphysics: Hysteresis* [Online]. Available at: `http://hyperphysics.phy-astr.gsu.edu/hbase/Solids/hyst.html`

Niguchi, N., Hirata, K., Muramatsu, M. and Hayakawa, Y. (2010). Transmission torque characteristics in a magnetic gear. In: *Electrical Machines (ICEM), 2010 XIX International Conference on*, pp. 1–6. IEEE.

Quadrant (2017 October). *Quadrant CHEMPLAST®Engineering Plastics* [Online]. Available at: `http://www.quadrantplastics.com/za-en/home.html`

Rasmussen, P.O., Andersen, T.O., Jorgensen, F.T. and Nielsen, O. (2005). Development of a high-performance magnetic gear. *IEEE Transactions on Industry Applications*, vol. 41, no. 3, pp. 764–770.

Rens, J., Atallah, K., Calverley, S.D. and Howe, D. (2010). A novel magnetic harmonic gear. *IEEE Transactions on Industry Applications*, vol. 46, no. 1, pp. 206–212.

Scott (2014 April). *Gears: An Historical Note* [Online]. 2014, april 21. Available at: `http://www.acceleratingtheaccelerando.com/`

Shaltout, A.A. (1994). Analysis of torsional torques in starting of large squirrel cage induction motors. *IEEE transactions on energy conversion*, vol. 9, no. 1, pp. 135–142.

Shi, L., Shi, C., Wang, J. and Wu, X. (2009). Numerical investigation of influence on heat transfer performance of direct air cooled condenser under different wind directions. In: *Computational Sciences and Optimization, 2009. CSO 2009. International Joint Conference on*, vol. 1, pp. 378–382. IEEE.

SKF (2017 October). *SKF Bearing Calculator* [Online]. Available at: `http://www.skf.com/africa/en/knowledge-centre/engineering-tools/skfbearingcalculator.html`

Stamper, E. (2017 January). *Harmonic Response Analysis Phase Angle Relationships* [Online]. Available at: `https://www.linkedin.com/pulse/harmonic-response-analysis-phase-angle-relationships-eric-stamper`

Tlali, P., Wang, R. and Gerber, S. (2014). Magnetic gear technologies: A review. In: *Electrical Machines (ICEM), 2014 International Conference on*, pp. 544–550. IEEE.

Tlali, P.M. (2015). *Design and performance evaluation of an outer stator magnetically geared permanent magnet machine*. Ph.D. thesis, Stellenbosch: Stellenbosch University.

TUFNOL (2017 October). *TUFNOL Composites limited* [Online]. Available at: `http://www.tufnol.com/contact/contact.aspx`

Vrancik, J.E. (1968). Prediction of windage power loss in alternators.

Wang, R., Brönn, L., Gerber, S. and Tlali, P. (2013). Design and evaluation of a disc-type magnetically geared pm wind generator. In: *Power Engineering, Energy and Electrical Drives (POWERENG), 2013 Fourth International Conference on*, pp. 1259–1264. IEEE.

Wowk, V. (1991). *Machinery vibration measurement and analysis*. McGraw-Hill, Inc.

Wrobel, R., Vainel, G., Copeland, C., Duda, T., Staton, D. and Mellor, P.H. (2015). Investigation of mechanical loss components and heat transfer in an axial-flux pm machine. *IEEE Transactions on Industry Applications*, vol. 51, no. 4, pp. 3000–3011.

Wurtz, W. (2008 September). Air-cooled condensers eliminate plant water use. Available at: `http://www.powermag.com`

Zhao, W. and Liu, P. (2009). Effect of wind on recirculation of direct air-cooled condenser for a large power plant. In: *Power and Energy Engineering Conference, 2009. APPEEC 2009. Asia-Pacific*, pp. 1–4. IEEE.

Zhao, W., Liu, P. and Wang, Q. (2011). The influence of thermal flow field on recirculation of air-cooled tower for a large power plant. In: *Power and Energy Engineering Conference (APPEEC), 2011 Asia-Pacific*, pp. 1–4. IEEE.

Zuo, S., Lin, F. and Wu, X. (2015). Noise analysis, calculation, and reduction of external rotor permanent-magnet synchronous motor. *IEEE Transactions on Industrial Electronics*, vol. 62, no. 10, pp. 6204–6212.